2020

Monotonic loading behavior of calcareous sands with increasing particle crushing

Wenjing Cai
Iowa State University

Monotonic loading behavior of calcareous sands with increasing particle crushing

by

Wenjing Cai

A dissertation submitted to the graduate faculty

in partial fulfillment of the requirements for the degree of

DOCTOR OF PHILOSOPHY

Major: Civil Engineering

Program of Study Committee:
Cassandra J. Rutherford, Major Professor
Vernon R. Schaefer
Junxing Zheng
Michael A. Perez
Jacqueline E. Reber-Vettiger

The student author, whose presentation of the scholarship herein was approved by the program of study committee, is solely responsible for the content of this dissertation. The Graduate College will ensure this dissertation is globally accessible and will not permit alterations after a degree is conferred.

Iowa State University

Ames, Iowa

2020

TABLE OF CONTENTS

Page

LIST OF FIGURES

Page

LIST OF TABLES

Page

ACKNOWLEDGMENTS

I would like to thank my committee chair, Dr. Cassandra Rutherford, and my committee members, Dr. Vernon Schaefer, Dr. Junxing Zheng, Dr. Michael Perez, and Dr. Jacqueline Reber, for their guidance and support throughout the course of this research.

In addition, I would also like to thank my fiancé, friends, colleagues, the department faculty and staff for making my time at Iowa State University a wonderful experience. I want to also offer my appreciation to those who were willing to participate in my surveys and observations, without whom, this thesis would not have been possible.

ABSTRACT

Calcareous sediment, comprising higher than 50% calcium carbonate by weight, are mostly located between latitudes 30°S and 30°N in coastal areas, such as Florida, India, Puerto Rico, and Australia. Lots of researches have been focused on the loading behavior and the particle breakage subjected to loading. It has been reported that in offshore construction, the measured capacities in calcareous were approximately 20% lower than predicted capacities. Therefore, it is necessary to investigate the loading behavior of calcareous sand with the scenario of post-construction. Calcareous sands from Puerto Rico and Western Australia are selected as the tested materials for this study. The primary objective is to investigate the static loading behavior of calcareous sand with increasing particle crushing. To accomplish this, the physical properties are determined firstly. Calcareous sand is found to have high carbonate content, high specific gravity, and porous particle structures. Triaxial undrained tests are performed with various confining pressures to investigate the static stress-strain behavior of uncrushed calcareous sand. Then, calcareous samples, prepared with different particle crushing contents, are tested by triaxial undrained tests. Various particle crushing contents are obtained by compression loading (one-dimensional consolidation test) and shear loading (triaxial consolidated drained test and TruePath test). The effect of the loading mechanism on particle breakage is evaluated as well. Results obtained from the tests for Puerto Rico and Western Australia sand are analyzed and compared with each other.

CHAPTER 1. INTRODUCTION

Research Motivation

Calcareous sands are mostly located between latitude 30°S and 30°N, covering approximately 40% of the world's seafloor. Previous research on calcareous soils generally recognizes that these soils demand special consideration due to their unique characteristic. The engineering properties of calcareous sands are quite different from those of silica sands and clays. The existence of high intraparticle porosity of calcareous sands results in high compressibility due to grain crushing. Low hardness and brittle particles are essential in this regard as well. Hence, particle breakage has been considered as one of the most effective parameters to describe the physical behavior for calcareous sands subjected to load.

For fundamental offshore construction, drilled and driven piles are commonly used. Calcareous sands can experience dramatic particle damage during pile driving, resulting in excessive foundation settlement. It is also reported that in offshore construction, the measured capacities in calcareous were approximately 20% lower than predicted capacities. This underestimation often occurred in the sand with high potential for particle damage. Therefore, it is necessary to investigate the engineering behavior of calcareous sand with increasing crushing contents, which helps to understand the scenario of post construction in foundation design.

Study Scope

The primary objective of this research is to investigate the stress-strain response of uncemented calcareous sand with increasing severities of particle damage. Puerto Rico and Western Australia are selected as the tested site due to the abundance of coastline with calcareous soils coupled with the high density of coastal constructions and developments, such as port facilities, renewable industries, hotels, and oil and gas platforms. The secondary objective is

to analyze and compare the engineering behaviors between the calcareous sand from Puerto Rico and Australia. To accomplish these two objectives, the research is divided into following tasks:

- Characterize properties of two calcareous sand particles, such as minerology, and index properties. Compare and determine the common and unique characteristics for two calcareous sands.
- Investigate the static stress-strain behavior of uncrushed calcareous sand from Puerto Rico and Australia. Determine the factors contributing to the undrained shear strength.
- Investigate the crushing potential of two calcareous sands. Evaluate the methods used to generate the particle damage.
- Investigate the static stress-strain response of two calcareous sands with the increasing particle crushing content; analyze how the loading response differs to the other calcareous sand.

The research findings help to better understand the loading behavior of uncrushed and crushed calcareous sand, which also can serve as the database and reference for design of infrastructure in coastal and offshore calcareous.

Dissertation Organization

This dissertation consists of 7 chapters. Chapter 1 presents a study motivation and study scopes with a detailed demonstration of the objectives and tasks.

Chapter 2 presents a literature review of the previous work on the topic of calcareous sand. Basic knowledge of the formation of calcareous soil is provided, following with a basic geological background of Puerto Rico and Western Australia. At the end of this chapter, loading behavior and effective parameters influencing the shear strength are introduced.

Chapter 3 provides information related to the experimental program. Index properties, carbonate determination, triaxial apparatus, one-dimensional consolidation apparatus, and the model used for quantifying particle breakage are presented.

Chapter 4 is the basic investigation of the static stress-strain behavior for two calcareous sand. Plots of stress-strain, excess pore pressure, stress paths, and stiffness degradation are plotted and explained. Ottawa sand is selected as a control group to compare with the other two calcareous sands.

Chapter 5 presents the three different crushing methods used to crush the calcareous sands. Sieve analyses were conducted before and after each test to determine the quantity of particle crushing. An investigation of the crushing potential for both calcareous sands and an evaluation of three methods are demonstrated. The modified stress-dilatancy model is introduced to analyze the correlation between dilatancy and particle breakage for two calcareous sands.

Chapter 6 presents the investigation on the effect of increasing particle breakage on the static stress-strain response for two calcareous sands. A series of triaxial undrained tests are carried out on the reconstituted specimens with increasing particle breakage. Data analysis is performed as well.

Chapter 7 provides the conclusion from the previous chapters and recommendations for future research.

CHAPTER 2. LITERATURE REVIEW

Introduction

This chapter begins with an introduction of marine calcareous sediments, including the definition, geographical distribution, and the morphology of calcareous particles. Additionally, the geological background knowledge of the materials used in the present study is introduced. Engineering behavior of calcareous sediments was investigated in the past decades, and is summarized in this chapter, such as the basic engineering properties, the compression behavior, and the monotonic shearing behavior. Since the present research mainly focuses on the monotonic shearing behavior of the sand, the cyclic loading behavior will not be included in this chapter. Particle crushing is one of the important factors influencing the loading behavior of the sand; therefore, the effective parameters relate to particle breakage, such as strain level, carbonate content, input energy, and so on, are introduced as well.

Calcareous Sediments

There are six general classes of ocean sediments: sand-silt fluvial marine sediment, silt-clay fluvial marine sediment, inorganic pelagic clay, siliceous ooze, calcareous ooze, and calcareous sand and silt (Keller, 1967), in which two of the six classes are calcareous soils. This marine calcareous sediment, comprising a calcium carbonate fraction by weight of more than 50%, are located between latitudes 30°S and 30°N in coastal areas, which can be summarized into seven regions: 1) Central and North America, such as the Gulf of Mexico, the shelf in the Caribbean Sea, and the South Florida Shelf; 2) South America, where calcareous sediments are found in the shallow water in the Campos Basin in Brazil; 3) Europe, such as the southern North Sea, the southern Baltic Sea, and the English Channel; 4) the Middle East, where high carbonate content sediments are found in the Arabian Sea, especially in offshore Qatar and the UAE; 5)

Asia, such as the offshore of India, Philippines, and Nansha Islands; 6) Africa, such as the offshore of Mozambique; 7) Australia, where the calcareous sediments are found in the North West Shelf extending to the Browse Basin, and the South West Shelf extending the Perth Basin (Watson et al., 2019). Figure 2.1 shows the world map of the known and potential areas of calcareous sediments.

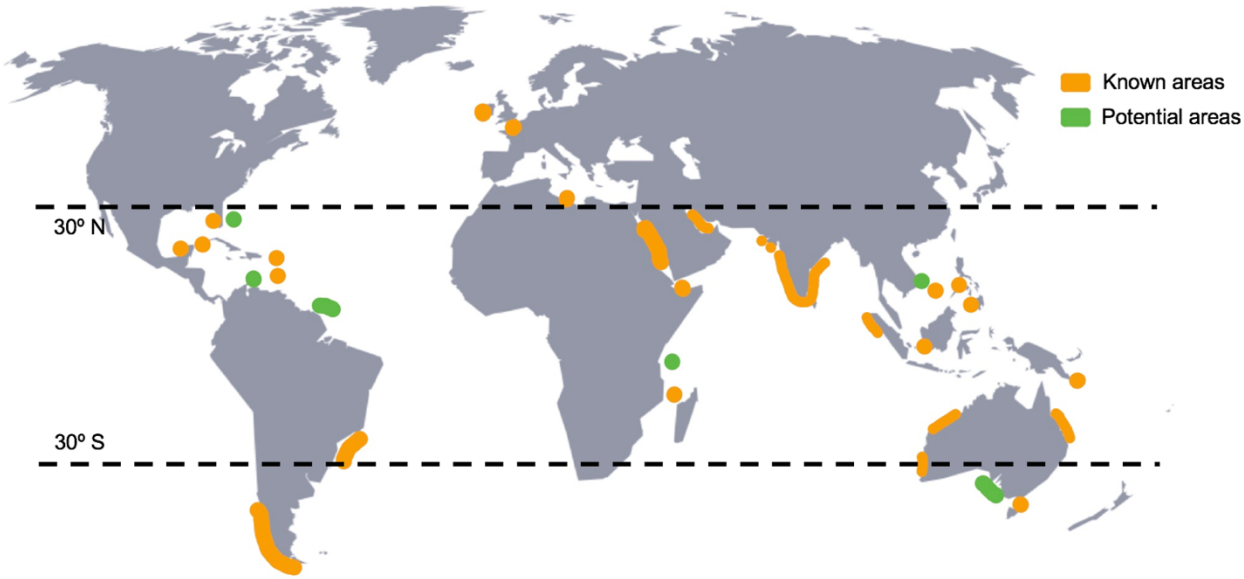

Figure 2.1. Offhsore Occurrence of Calcareous Sediments (Modified from Spagonoli & Doherty, 2016 & Watson et al., 2019)

Calcareous sediments mostly originate from biochemical processes attributed to coral reef formation, sedimentation of skeletal debris, and chemical precipitation of particles (Murff, 1987; Milliman et al., 1974). The nature of the sediments and the diagenetic alteration, also in terms of carbonate geology, depends on complex interrelated factors: temperature, climate, salinity and clarity of water, water depth, distance from land, pore water chemistry, and metocean condition. Importantly, these factors vary over geological time (Watson et al., 2019). Figure 2.2 provides a simplified schematic of a generic ground model focusing on the open continental shelves. Generally, the types of sediments are highly variable in shallow water (less

than 120 m), but there is not as much variability in deep water (Clark et al., 2009; Watson et al., 2019). Beemer et al. (2018) collected the calcareous sediments from beach and a water depth of 200 m. The calcareous sand from beach composes mainly of coralline algae, benthic foraminifers, abraded fragments of bivalves, and bryozoans with some quartz grains. On the other hand, the sand composition from the deep-water sample is mainly consisted of benthic and planktic foraminifers and intraclasts, such as fragments of corals and bryozoans. Additionally, water depth also controls the grain size of the carbonate sediments. Carbonate sediments in shallow water generally have larger grain sizes, while sediments from deep ocean water tend to have finer grain sizes. This can be attributed to the different energy in different water depths. Sediments in shallow water are exposed to high energy resulting from tides, waves, currents, wind, and sea-level changes. The sediments in this environment are easily transported and reworked. Sediment input sources are rivers, deposition of materials by tides, and the accumulation of fragments of the skeletons living in shallow water. On the contrary, the deep water has low energy and increases the input of pelagic sedimentation and small particles transported far away from the coast, resulting in the muddy sediments in this environment (James et al., 2004; Beemer et al., 2019). Different water depth results in different grain sizes and compositions in skeletal grain types, which potentially influence their engineering properties (i.e. relative density and void ratio, etc.) (Beemer et al., 2018).

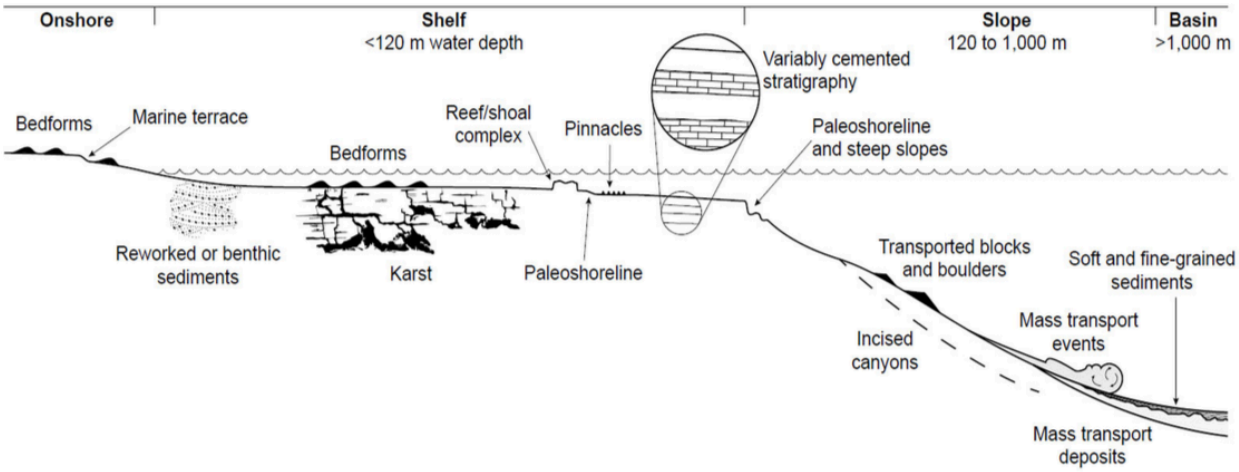

Figure 2.2. Generic Ground Model in Shelf Cross Section (Watson et al., 2019)

The mineralogy and diagenesis of carbonates usually differ for shallow marine environments and deep marine environments (Morse & Mackenzie, 1990). The carbonate-rich sediments in the shallow marine environments are generally dominated by aragonite and calcite rich in magnesium; whereas calcareous sediments in deep marine environment are composed of calcite poor in magnesium (Arango, 2006).

Marine calcareous soils can be divided into two categories based on their grain types: 1) skeletal grains, and 2) non-skeletal grains. Skeletal grains derived from biochemical origins are formed from the internal or external skeletal structure of marine animals and plants, such as corallines, whole shells or fragments of mollusks, and gastropods. These biogenic productions take place on the seafloor and in the water column, and they have high variability in morphology (as shown in Figure 2.3), for instance, balloon-like planktonic foraminifera, thin-walled debris, and solid ooids (Watson et al., 2019). The formation of non-skeletal grains occurs by a variety of chemical and physical processes, such as the biochemical precipitation and/or the inorganic physio-chemical precipitation of ooids, mud, peliods, and composite grains (Morelock & Ramirez, 2004; Arango, 2006).

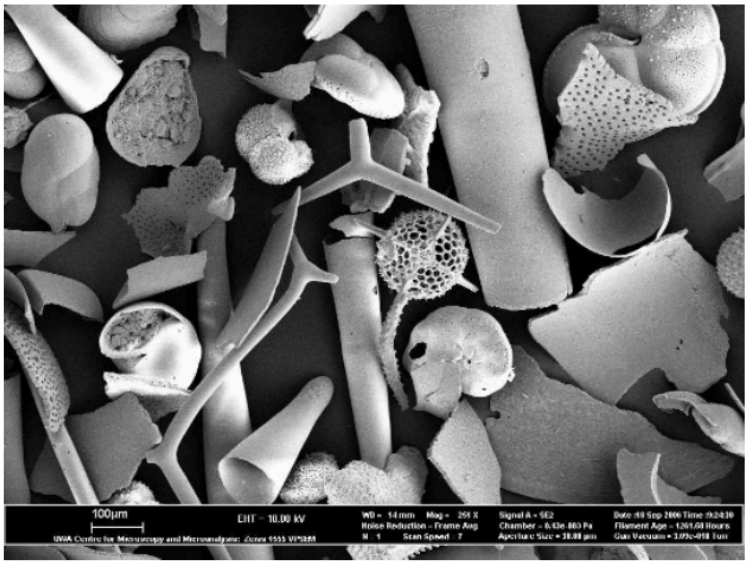

Figure 2.3. Example Microscopic Image of the Skeletal Carbonate Sediments (Watson et al., 2019)

Calcareous sand exhibits a higher specific gravity (G_s) and higher void ratio compared to silica sand (Murff, 1987; Morikoa, 1999; Arango, 2006; Wang et al., 2011). The high specific gravity of calcareous sand generally ranges between 2.75 and 2.85, which is due to its main mineralogy composition such as calcite (G_s = 2.75) and aragonite (G_s = 2.95). In contrast, silica sand presents a lower value of specific gravity due to its mineral composition of quartz with a specific gravity of 2.65 (Hurlbut, 1971). The void ratio is defined as the volume of voids divided by the volume occupied by the solids at a given density. Terzaghi et al. (1996) stated that the void ratio in sand is generally ranging from 0.43 to 0.85. The main particle component of calcareous sand is biogenic grains with intraparticle porosity, which leads to an additional volume of voids. Thus, void ratio of calcareous sand is found to be higher than silica sand.

The majority of the calcareous soils are graded in a medium to coarse range with high angularity. The shape of calcareous soil particles varies widely from flat shelly particles to nearly spherical precipitate particles. The properties of individual particles play an important role on the engineering behavior of the material (Murff, 1987). The grain crushability and material

compressibility of calcareous sand are normally defined by the shape, intraparticle porosity, and surface texture of the composing particles (Arango, 2006).

Coastal Geology of the Soil Origins

Calcareous sands from different origins show different characteristics. In the present study, the calcareous sands are from offshore Puerto Rico and Western Australia. The geological background of these two locations is introduced in the following sections.

Perth Basin in Western Australia

Western Australia (WA) is the largest state of Australia, occupying the entire western third of the country. The geology of Western Australia shows 4.4 billion years of Earth's history, dating back to the oldest dated zircon grains at Jack Hills to the recent sediments forming currently on the Swan Coastal Plain around Perth (Government of Western Australia, 2017). As shown in Figure 2.4, the Perth Basin is an onshore and offshore sedimentary basin extending about 1000 km along the southwestern margin of the Western Australia continent, which was formed about 200 million years ago when the Darling Fault line became active, resulting in the land subsidence to the west. Since then, the sea level has changed several times, contributing to the building up of sediments west of the Scarp and the changing coastline growing gradually westwards. This sedimentary basin, the Perth Basin, extends out to the sea beyond the current coastline and is covered by the more recent sediments around the existing coastline—the Swan Coastal Plain.

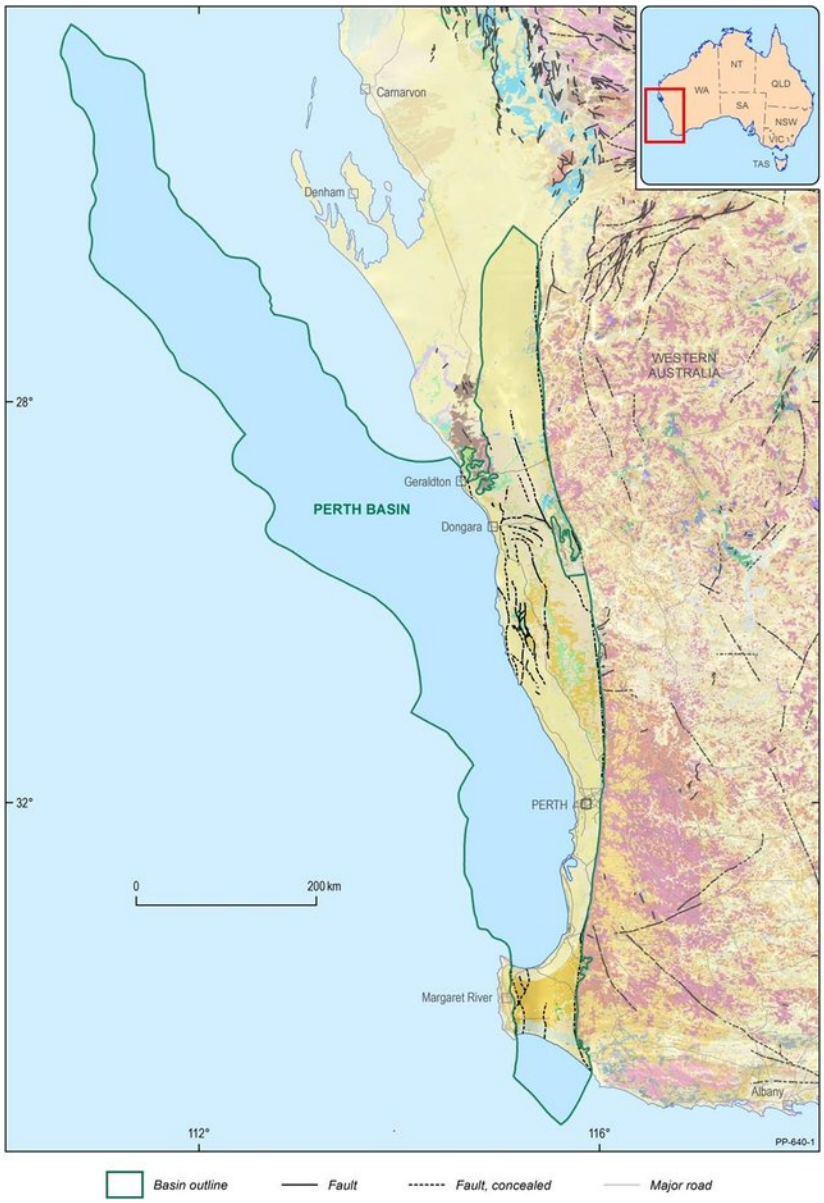

Figure 2.4. Location of the Perth Basin (Raymond et al., 2012; Hashimoto et al., 2018)

The Swan Coastal Plain includes several geomorphological units, distributed approximately parallel to the current coastline (as shown in Figure 2.5). According to Gozzard (2007), they can be summarized into four broad geomorphic units, three of which are deposited by wind (aeolian) in the west and rivers (alluvial) in the east. In general, the processes including erosion, transportation, and deposition of sediments by wind under much drier climactic condition are defined as aeolian process, and the resulting sediments are named as aeolian

sediments. The alluvial sediments are produced when a river or stream slows down and deposits sediments that are transported as bedload or in suspension.

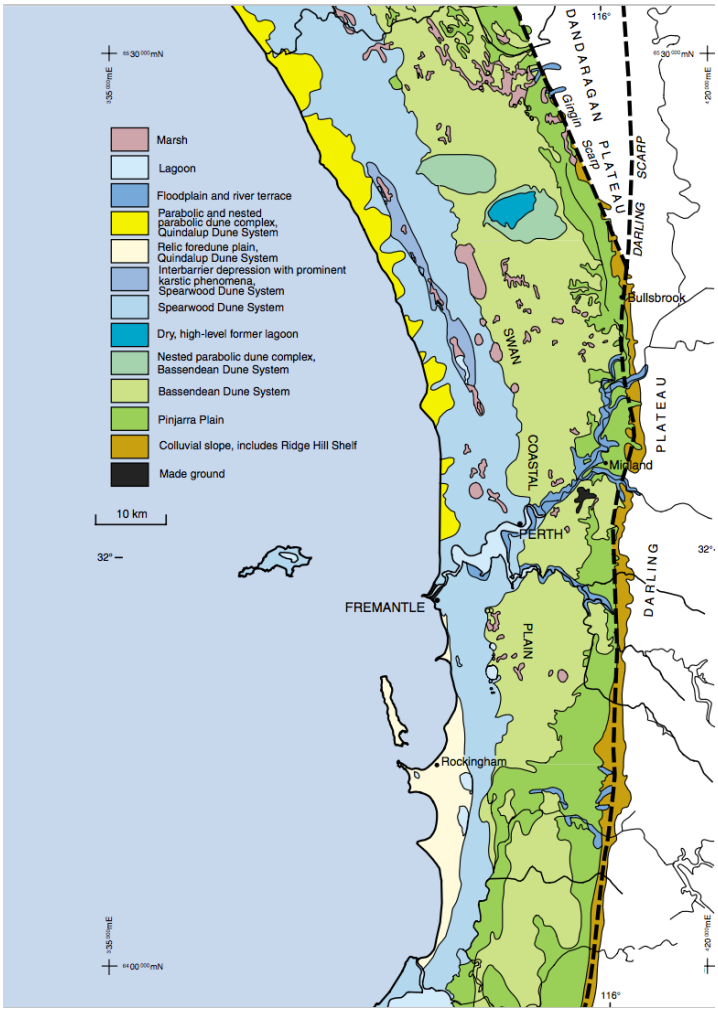

Figure 2.5. Generalized Geomorphology of the Perth Basin (Gozzard, 2007)

The three units of aeolian sediments in the Swan Coastal Plain are representing three separate geological ages shown as following: 1) Bassendean Dunal System. Series of shoreline deposits and coastal dunes within a 15 km-wide zone between the Pinjarra Plain and the Spearwood Dune System. This system was formed around 800,000 to 125,000 years ago in an interglacial period. The dunes have well-bleached white-grey sands, dominantly marine and lacustrine deposits which are reworked and eroded. The dunes are composed of low hills of

quartz sand with sandy swamps in swales between the dunes (Gozzard, 2007). 2) Spearwood Dunal System. This is a large-scale system, westward to the Bassendean Dune System, formed 40,000 years ago during the Pleistocene glacial and interglacial periods. The dunes exhibit the color of yellow brown and consist of the aeolian parts of the Tamala Limestone, which is the medium- to coarse-grained calcarenite with various amounts of quartz sand and plenty of broken fossil shell fragments (Gozzard, 2007). The calcium carbonate originally in the sediments tends to be leached out during water (rain) passes through the sediments and then reforms limestone beneath the soil. 3) Quindalup Dunal System. This system is the most westerly dune system, formed 10,000 years ago during the glacial-interglacial periods. This dune system is composed of unconsolidated calcareous sands with a cream color. Faibridge (1967) demonstrated that the aeolian calcarenite in this region could be associated with pluvial phases of the Quaternary, resulting in the calcareous sands cemented rapidly by percolating rainwater. Hails (1982) also defined the calcareous sands cemented or lithified by percolating rainwater are called aeolian calcarenite. The Australia sand used in the present study originates from the Quindalup Dunal System.

The fourth geomorphic unit, deposited by rivers, is called Pinjarra Plain located in the eastern part of the Swan Coastal Plain, which formed at the same time the aeolian units. The Plain is an alluvial tract of unconsolidated loams and clays with small amounts of limestone. There are alluvial fans near the scarp and floodplains along the rivers. The alluvial fans are higher along the paths of larger streams or rivers which emerge from the Darling Plateau; they merge imperceptibly with floodplain and estuarine sedimentary rocks in the west.

Coastal Geology of Puerto Rico

Puerto Rico, located between the Caribbean Sea and the North Atlantic Ocean, was formed early in the tectonic history of the Caribbean when the South American and North

American plates separated. It is approximately rectangular shape and originated as a chain of volcanic islands between the late Jurassic and early Cretaceous (Morelock & Taggart, 1988). The coastline of Puerto Rico is about 1,300 km long, comprising of 30% beach, 28% vegetated shorelines, 18% alluvial plains, and 15% rocky shorelines (Barreto, 2017). According to Kaye (1959), the coast of Puerto Rico can be divided into five types (as shown in Figure 2.6): 1) Type A: The Northeast coast from Punta La Bandera to Playa de Naguabo consists of rocky headlands and small offshore islands formed by the long spurs of the Sierra de Luquillo (a mountain range); 2) Type B: i) The Southeast coast from Playa de Naguabo to Puerto Patillas is characterized by large headlands and broad alluvial valleys which are fronted by long arcuate beaches with silica sand. The coastline in this area gives indications of fault control; for instance, the tectonic escarpments both inland and off the coast. ii) The Southwest coast from Punta Cuchara to Aguadilla consists of alternating rocky and alluvial stretches. The rectilinear nature of the northwest-trending shore of the Rincón peninsula is evidence of fault control; 3) Type C: The South coast from Puerto Patillas to Punta Cuchara is a piedmont alluvial plain and is formed by narrow beaches of dark-colored silica sand and andesitic gravel which alternates with mangrove swamps. The outlines of the coast are discontinuous and separated by asymmetrical bays; 4) Type D: The Northwest coast from Aguadilla to Arecibo comprises of limestone cliffs which form the shore or is separated by a narrow rocky or sandy bench. The current shoreline is erosional and related to the east-west trending faults located to the north of the island; 5) Type E: The North coast from Arecibo to Punta La Bandera is an alluvial plain separated by several large swamps and lagoons. Some sites of this area are fossil dunes of aeolianite formations and Pleistocene reef rocks.

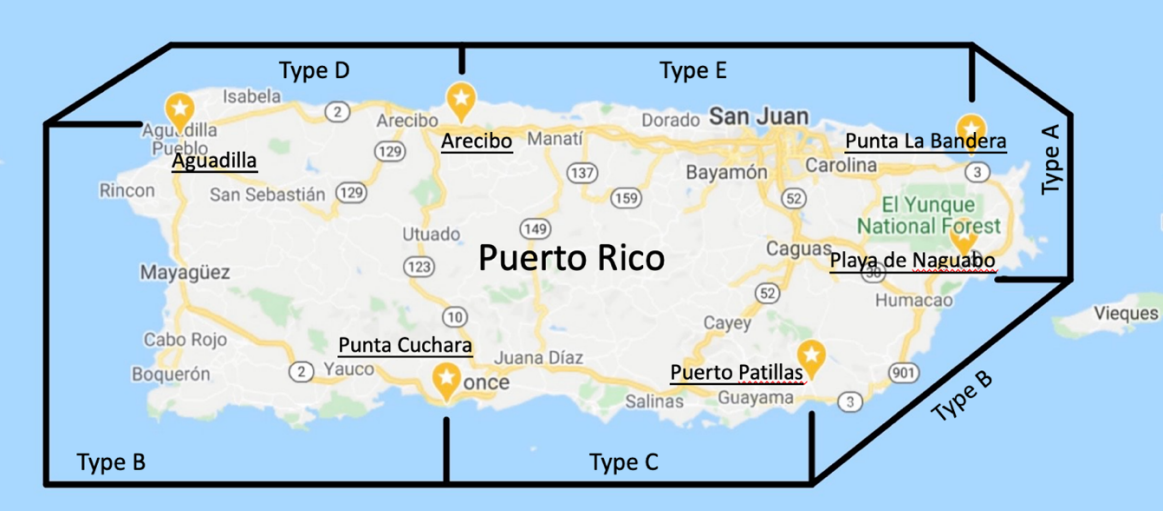

Figure 2.6. Puerto Rico Shoreline Types (Modified from Kaye 1959)

The coastline types are not assigned names because the present coastal classifications are restrictive in their morphologic implications and insistent on the distinction about the origin of the coast; therefore, the coastline types were described by Kaye (1959) in order, starting at the northeastern corner of the Puerto Rico island and proceeding in a clockwise direction. Morelock (1978) also divided the Puerto Rico coastline into three categories based on the coastal landforms: rocky cliff and headlands, mangrove coast, and sand or gravel beaches. The sand and gravel beaches of Puerto Rico are characterized by three major sources: terrigenous sand driven by rivers, dark minerals and dark igneous rock fragments due to river drainage, and calcium carbonate sediments supplied by the shoreward transport of the shells and debris of marine organisms. Figure 2.7 shows the beach composition for the beach systems of Puerto Rico in detail.

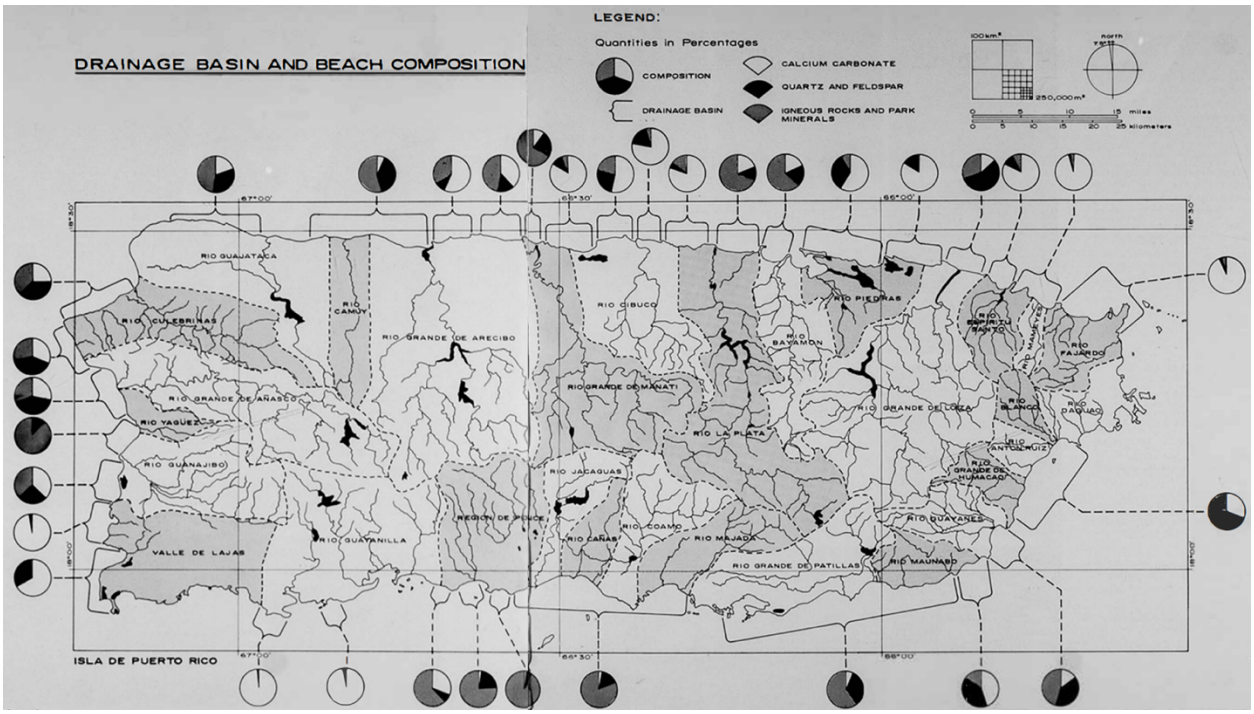

Figure 2.7. Beach Composition of Puerto Rico (Morelock, 1978)

As shown in Figure 2.7, the northeast coast and southwest coast consist of mainly calcareous sands which can be found in uncemented and cemented form. The Puerto Rico sand samples for the present study belong to Type B of the shoreline types and are located in the southwest coast. The beach systems in southwest corner are away from rivers outlets and deltas and are mainly composed of the shells and debris of marine organisms.

Behavior of Calcareous Sand

It is necessary to understand the mechanical behavior of calcareous soils for designing and construction of structures. Generally, the calcareous soils in the literature on this topic can be grouped as the following: uncemented calcareous soils, artificially cemented calcareous soils, and natural calcarenites (Sharma, 2004). The material involved in this research is uncemented calcareous sand; hence, the literature background introduced here are based on uncemented calcareous soils.

Compression Behavior

Similar to other granular materials, calcareous samples with various initial densities tended to close toward a unique Normal Compression Line (NCL) in e-lnp' plot with the increasing pressure (Pestana, 1994). Conversely, the required stress for calcareous sand to reach the NCL is much lower than that of non-calcareous soils. Coop and Lee (1993) showed that the loose calcareous sand from Dog's Bay achieved the NCL at pressure of 1 MPa; however, for loose silica sand from Ham River, the pressure had to reach up to 10 MPa to achieve its NCL (as shown in Figure 2.8). Calcareous sand had more volumetric reduction during compression compared to non-calcareous soils because of its intraparticle porosity and fragile angular grains (Coop & Airey, 2003; Sharma, 2004).

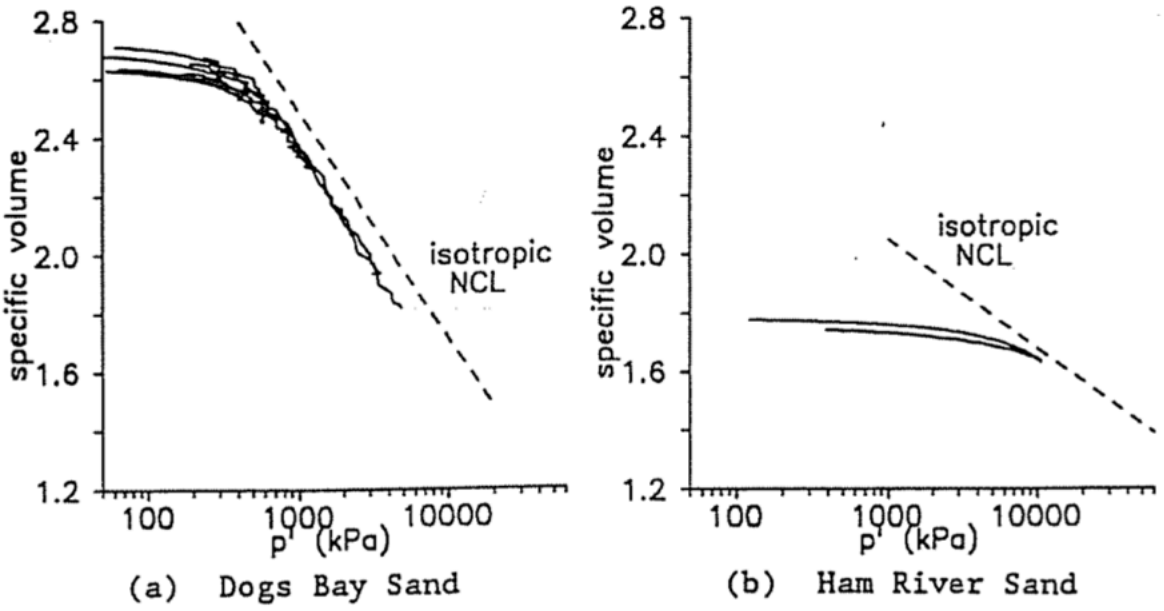

Figure 2.8. One-Dimensional Compression (Coop, 1990; Coop & Lee, 1993)

Monotonic Shearing Behavior

Calcareous sand exhibits a higher friction angle than silica sand during drained and undrained shearing tests with similar relative densities, which is typically higher than 35° and even exceeding 50° (Murff, 1987; Hull, et al. 1988; Arango, 2006; Safinus et al., 2013). Although silica sand presents a smaller friction angle, it exhibits a reliable tendency to dilate, helping with maintaining of stiffness and shear strength. Calcareous sand exhibiting a higher friction angle only shows dilative behavior under low confining pressures (Zhang et al., 2008) or even no dilation followed by significant particle crushing and resulting in less stiffness response (Hull et al., 1988).

A comparison on dilatancy of calcareous sand and silica sand was conducted by Golightyly and Hyde (1988). They performed triaxial drained tests on Dog's Bay sand (calcareous sand) and Lerghton Buzzar sand (silica sand) subjected to various confining pressures. The results showed that the increasing confining pressure suppressed the dilatancy for calcareous sand. Dog's Bay sand achieved its critical confining stress when the dilation angle was zero at the confining stress of 370 kPa; however, the Leighton Buzzard sand maintained a constant dilation angle of 10° even the confining stress was higher up to 1000 kPa.

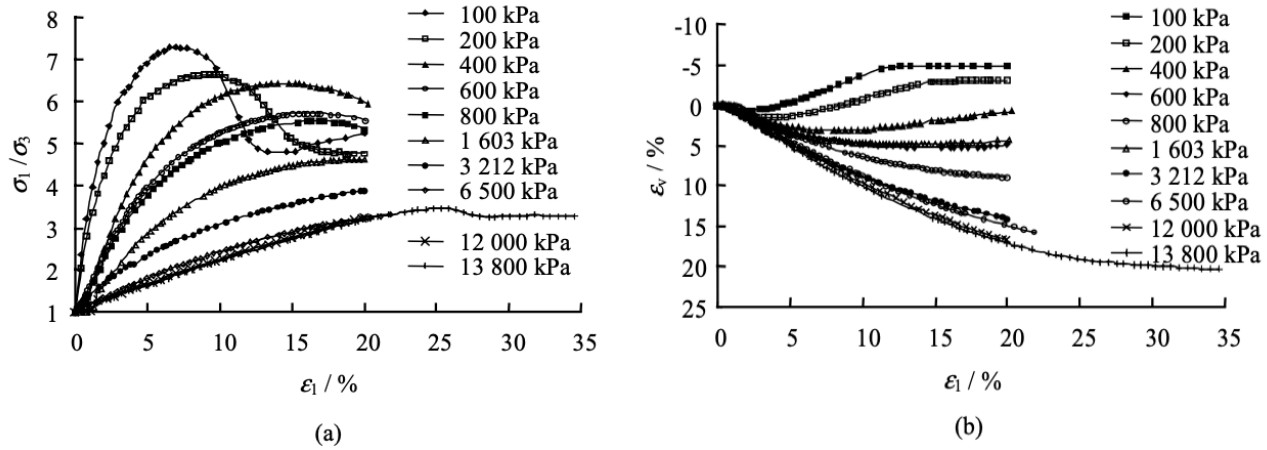

Figure 2.9. Typical Triaxial Behavior of Calcareous Sand (Zhang et al., 2008)

A similar tendency can be found from the research of Zhang et al. (2008). A series of triaxial drained tests were performed on calcareous sand from Nansha Island, China, to investigate the dilatancy and particle breakage. The results showed that dilation of calcareous sands occurred at low confining pressures, especially under 200 kPa. After 400 kPa, those sands exhibited contraction. The volumetric change (contraction is positive) and stress ratio at different confining pressures are shown in Figure 2.9. It was concluded that a higher confining pressure decreased the particle dilation, resulting in crushing and compaction. This early transition to contraction was caused by grain crushing, which occurred with relatively low stress. As a result, grain crushing hindered the development of potential maximum dilation, and led to a ductile stress-strain response with peak shear strength achieved at large axial strains (Arango, 2006; Safinus et al., 2013).

Particle Breakage of Calcareous Sand

Calcareous sand showed high compressibility during loading, which was up to 100 times higher than that of silica sand (Nauroy & LeTirant, 1979). This high compressibility is attributed to the particle breakage because of the low hardness and existence of intraparticle voids of the grains. Particle breakage highly influences the stress-strain response and other geotechnical behavior; therefore, it becomes a very important consideration for calcareous sand. Effective parameters affect particle breakage of calcareous sand are summarized in the following sections.

The Effect of Relative Density

Shahnazari and Rezvani (2013) performed isotropic compression tests and triaxial drained tests on two calcareous sands in loose and dense density, respectively. The results showed that the particle breakage decreased as the relative density increased in isotropic compression tests, while the opposite results were obtained in drained tests. As the relative density increased, the particle breakage increased as well.

Another investigation conducted by Dehnavi (2010) provided an information on the effect of density. The isotropic compression tests under high stress were performed on Hormuz calcareous sand, and a wider range of relative density was covered in this research. The correlation of relative density and particle breakage is shown in Figure 2.10. The particle breakage was indicated by the variation of surface area. Based on the result, the particle breakage increased as the relative density increased from loose to medium dense, but the crushing decreased when the relative density increased from medium dense to dense conditions. In other words, the maximum particle breakage occurred at medium density for isotropic compression test. The average contact stress was considered the only factor related to particle breakage. Therefore, the number of surrounding particles was increased in the dense sample, resulting in the average contact stress decreasing.

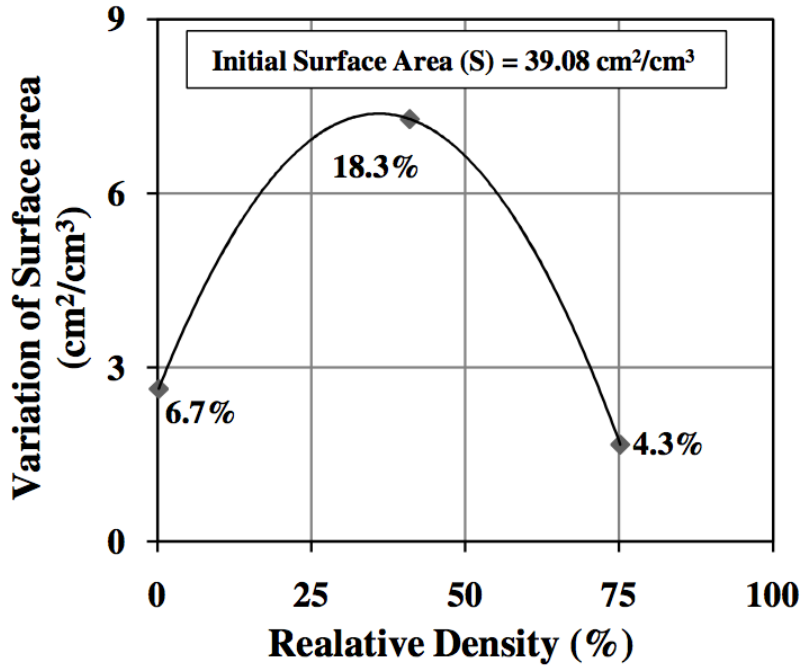

Figure 2.10 Variation of the Grain Surface Area in the Isotropic Compression Test as the Confining Pressure 1500 kPa (Dehnvai, 2010).

The Effect of the Drainage Condition

Results from Shahanazari and Rezvani (2013) are presented in Figure 2.11, showing that the drained condition led to more particle breakage than that of undrained condition. In the drained condition, there was no excess pore pressure generated; thus, the effective stress was equal to the total stress, and all of the exerted pressure was applied to the sand particles. However, the generated excess pore pressure in undrained condition caused the difference between effective and total stress. Part of the deviatoric load was sustained by soil particles, and the rest of the load was sustained by generated pore pressure. Hence, drained condition caused more particle breakage.

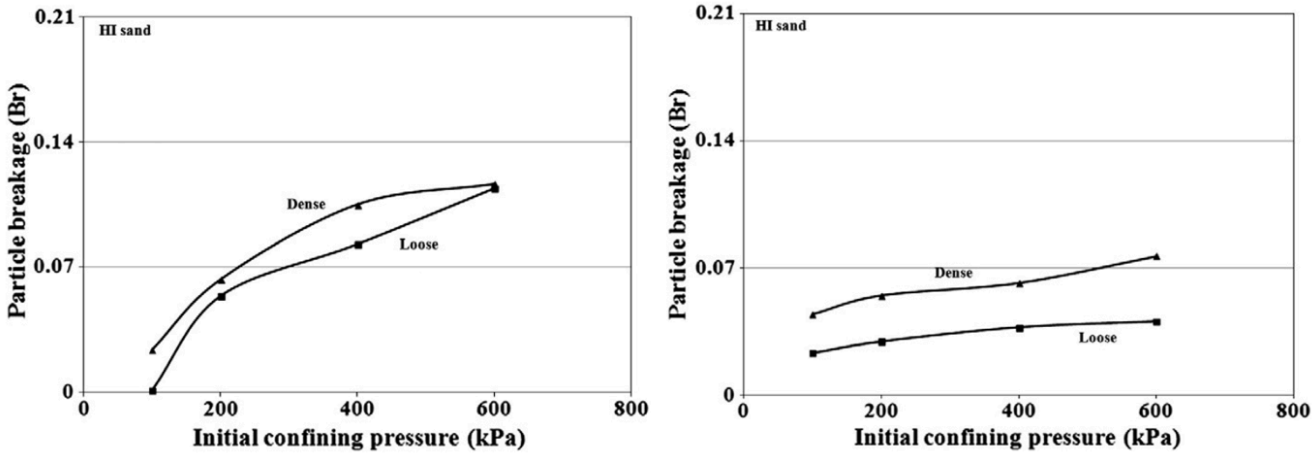

Figure 2.11. Particle Breakage of HI Calcareous Sand in Drained Triaxial Tests (Left) and Undrained Triaxial Tests (Right) (Shanazari & Rezvani, 2013).

The Effect of Stress Levels

Lade (1996) showed that larger amounts of particle breakage regenerated as stresses are increased. A similar tendency was also shown by Zhang et al. (2008). Figure 2.12 presents the correlation between particle breakage and confining stress caused by isotropic compression and triaxial shearing. Triaxial shearing generated more particle breakage than isotropic compression. For both loading mechanisms, particle breakage increased as the confining pressure increased. It

also noted that the slope of triaxial shearing curve decreased when the confining stress increased beyond 6,500 kPa, and the increment of particle breakage decreased even though the confining pressure increased. This indicated that there should be a limit for particle breakage, and the crushing would stop when a stable grading was reached, which was consistent with the conclusion suggested by Hardin (1985).

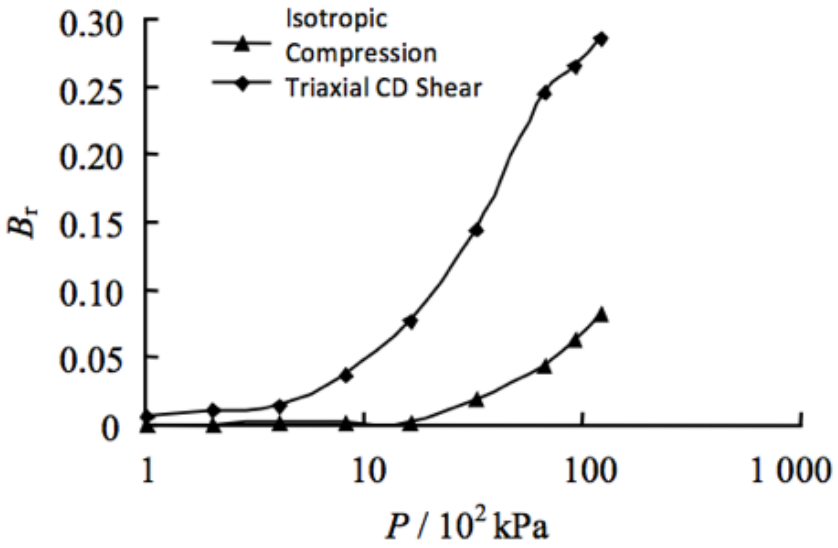

Figure 2.12. Relationship between Particle Breakage and Confining Pressure (Zhang et al., 2008).

The Effect of Carbonate Content

Calcareous sands from different origins contain various carbonate contents. Figure 2.13 presents particle crushing contents of different calcareous soils and non-calcareous soil with different carbonate content. Soil A to F were calcareous soils, and soil T was a quartz soil. Based on the results, soil F obtained a similarly low content of particle crushing as soil T, although soil F consisted of 90% carbonate content. Soil D contained the highest carbonate content but did not obtained the largest crushing amount. It became evident that the potential of particle breakage was independent on the carbonate content and was dependent of the nature of sand particles (Datta et al., 1982).

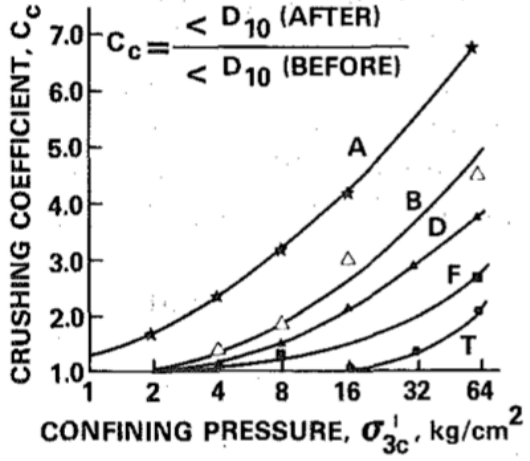

	SOIL DESCRIPTION		
SAND	PARTICLE CHARACTERISTICS	CARBONATE CONTENT	PARTICLE SIZE
A	SKELETAL W/ SHELL FRAGMENTS	92.2	COARSE
B	SKELETAL W/ SHELL FRAGMENTS	93.7	COARSE TO MEDIUM
D	SKELETAL W/ CORALLINE DEBRIS	95.0	MEDIUM TO FINE
F	NON SKELETAL, ROUNDED	90.1	MEDIUM TO FINE
T	ROUNDED, SOLID QUARTZ	0	COARSE TO MEDIUM

Figure 2.13. Crushing Characteristic of Various Sands (Murff (1987) Modified from Datta et al., 1982).

The Effect of Particle Size Distribution and Other Grain Properties

The particle size distribution had a significant effect on particle breakage (Shahnazari & Rezvani, 2013). It also can be observed in Figure 2.13, soil A with coarse particles had the largest amount of particle breakage, and soil D and F with medium to fine particles obtained less particle breakage compared to soil B with coarse to medium particles. A conclusion can be made that increasing particle size resulted in an increase of particle breakage. Larger particles have more defects or flaws; these larger particles also have a higher probability of the defect, leading to break. Conversely, smaller particles are generated from larger particles fracturing from these defects. When the crushing process continues, there are fewer defects in the existing subdivided particles, hence, similar particles have less potential to fracture as getting smaller (Lade et al., 1996).

Besides particle size distribution, particle breakage also increases when the following parameters increasing: 1) the amount of particles containing large intraparticle voids; 2) the angularity of particles; 3) the amount of thin-walled fragments; 4) uniformity of gradation; 5) mineral hardness (Datta et al., 1982).

Large amounts of intraparticle voids and more thin-walled fragments lead to a weaker particle structure in calcareous sand. When subjected to load, calcareous sand with weaker particle structure has a higher potential to be crushed.

Higher angularity of particles leads to higher particle breakage. Angular particles are broken more easily because stress is able to concentrate along the narrow dimension of particles which is easy to fracture the particles. Additionally, stress can also cause the fracture by concentrating at angular contact points (Lade et al., 1996).

High uniformity of particle gradation, classified the soil as well-graded, is not easy to be crushed compared with low uniformity soils (Lade et al., 1996). The reason is similar to the mechanism of increasing relative density mentioned previously. Soils with high uniformity have more particle surrounding each particle, resulting in the average contact stress decreasing.

Higher mineral hardness reduces the amount of particle breakage. For a given stress, harder particle materials tend to have a smaller amount of crushing. Figure 2.14 shows the hardness of different minerals in Mohs hardness and Sclerometer hardness. Calcite, the major component of calcareous soil, has a low absolute hardness of 9, while quartz sand has the absolute hardness of 100. Therefore, calcareous soil is much more easily crushed subjecting to load.

Hardness (mohs)	Mineral	Absolute Hardness (sclerometer)
1	Talc ($Mg_3Si_4O10(OH)_2$)	1
2	Gypsum ($CaSO_4 \cdot 2H_2O$)	2
3	Calcite ($CaCO_3$)	9
4	Fluorite (CaF_2)	21
5	Apatite ($Ca_5(PO_4)_3(OH\text{-},Cl\text{-},F\text{-})$)	48
6	Orthoclase Feldspar ($KAlSi_3O_8$)	72
7	Quartz (SiO_2)	100
8	Topaz ($Al_2SiO_4(OH\text{-},F\text{-})_2$)	200
9	Corundum (Al_2O_3)	400
10	Diamond (C)	1500

Figure 2.14. Mohs Hardness and Sclerometer Hardness of Different Minerals (Modified after Gianfranco et al., 2013)

The Effect of Axial Strain Levels

For a given relative density and given loading stress, larger axial strain level causes more particle breakage. Shanazari and Rezvani (2013) performed a series of triaxial drained tests on calcareous sand with three different axial strains of 5%, 15%, and 25%. All samples were controlled in the same relative density and a constant confining pressure of 600 kPa. It was reported by Tugoes Garcia (2008) that the loading rate on calcareous soil had a negligible influence on its stress-strain behavior. As the results shown in Figure 2.15, both calcareous sands involved in Shanazari's research exhibited an increasing tendency when axial strain increased. A similar conclusion was made by Zhang et al. (2008).

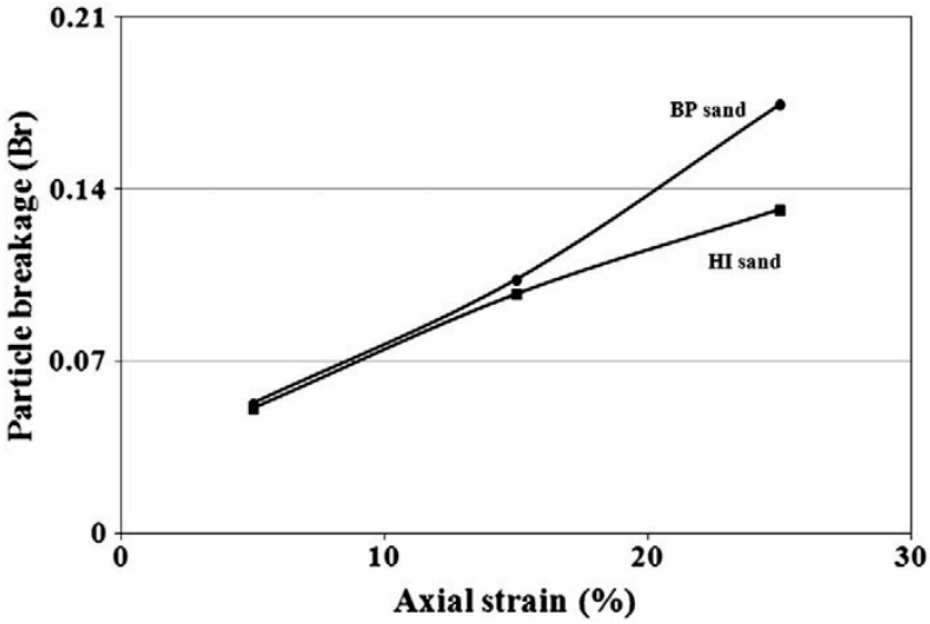

Figure 2.15. The Effect of Axial Strain on Particle Breakage of Calcareous Sands (Shanazari & Rezvani, 2013)

The Effect of Input Energy

The effect of membrane penetration should be considered in undrained and drained triaxial tests since it affects the pore water pressure of specimen (or volume change in drained test). When pore pressure changed by the influence of membrane penetration, the effective confining pressure was affected, leading to the disturbance on particle breakage (Baldi & Nova, 1984; Shanazari & Rezvani, 2013). To avoid this, the input energy was introduced and can be expressed as follows:

$$\delta W = q'\delta\varepsilon_s + p'\delta\varepsilon_v \quad (2.1)$$

in which W represents the energy (or work) done per unit volume of soil; q' represents the deviator stress (kPa); ε_s is the axial strain (%); p' is the mean effective principle stress (kPa); and ε_v represents the volumetric strain (%). Figure 2.16 shows the energy input results based on the work of Shanazari & Rezvani (2013). They observed that particle breakage increased as the input energy increased. For a constant input energy, it was found that the loose sand samples obtained

more particle breakage. Loos sand sample had fewer contact areas; hence, with the constant input energy, loose sand subjected a higher average contact stress between particles.

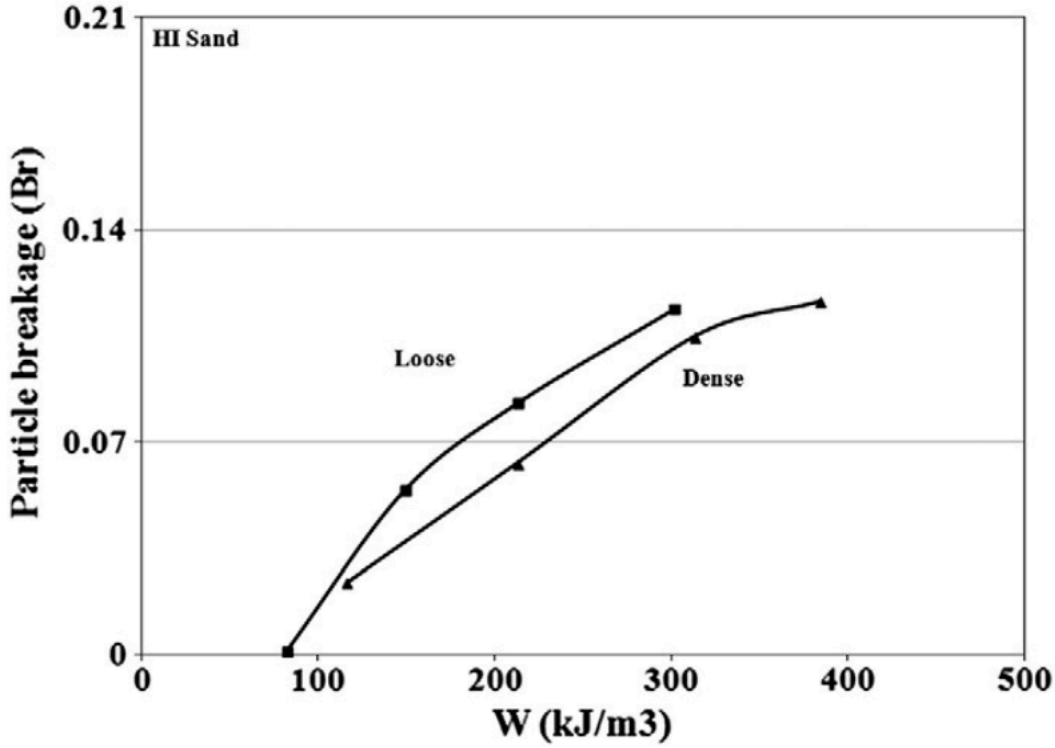

Figure 2.16. The Effect of the Input Energy on the Particle Breakage (Shanazari &Rezvani, 2013)

Steady State of Sand

The steady state of sand is defined as the state in which the sand will reach a stable grading that the particle contact stress will not be sufficient to generate further breakage (Coop et al., 2004). In the consideration of triaxial loading condition, the steady state can be explained as a balance between the volumetric compression attributed to particle breakage and volumetric dilation due to particle rearrangement (Chandler, 1985; Baharom & Stallebrass, 1998).

Generally, undrained tests were used to determine the steady state of soil on loose sand samples (Been et al., 1991). For undrained the condition, the void ratios at a steady state are measured, and are plotted on one graph along with the corresponding final effective stresses in a

logarithmic scale. A fitted line can be drawn, which is referred to as steady state line (SSL) (Ishihara, 1996). Figure 2.17 shows a concept sketch of the steady state line. The slope of the SSL is mainly affected by the shape of particles, and the vertical position of it is affected by particle size distribution (Poulos et al., 1985).

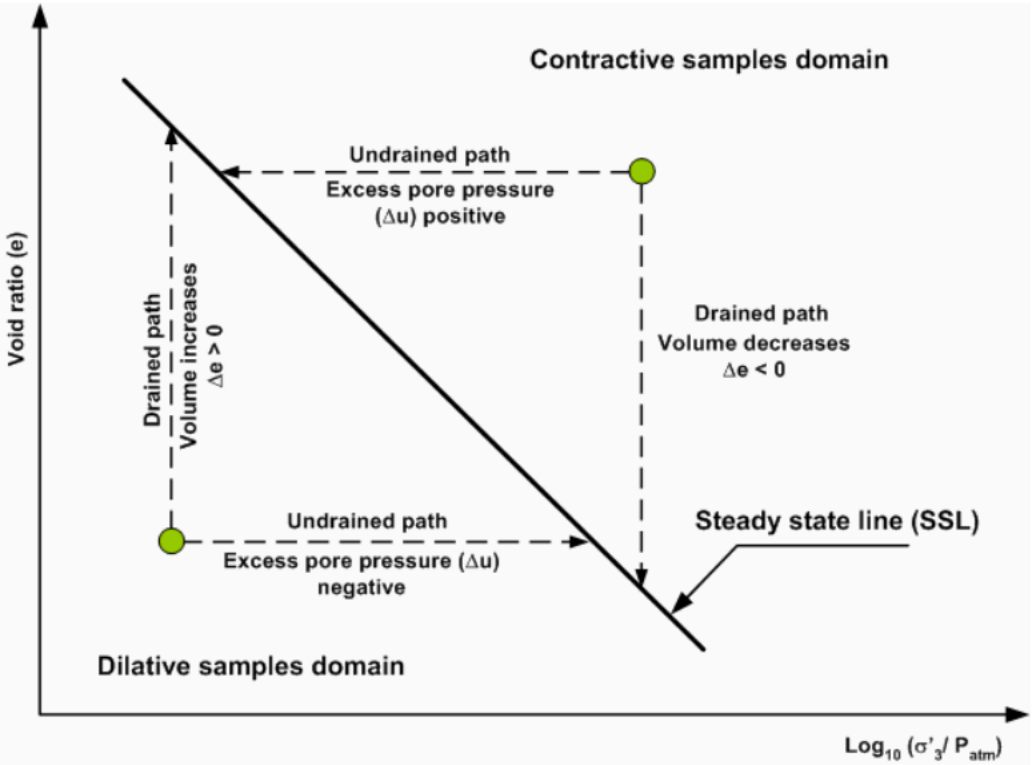

Figure 2.17. Concept Sketch of Steady State Line (Arango, 2006)

According to the SSL, sand samples with an initial state above the SSL are regarded as contractive sands, indicating that the sands will move toward the SSL by decreasing void ratio in drained condition or increasing pore pressures during undrained condition (contraction). Sand samples with an initial state below the SSL are considered dilative sands. It is inferred that the dilative sands tend to move towards the SSL by increasing void ratio in drained condition or decreasing pore pressure in undrained condition (dilation) (Arango, 2006). For a given sand, the

SSL is independent of the initial densities, sample preparation, and stress path (Been et al., 1991).

The state parameter (ψ) was introduced by Been and Jefferies (1985) to define the current state of the sand. This parameter is determined by the current specific volume (υ) and effective stress (p') of a sand relative to the SSL as the following equation:

$$\psi = \upsilon - \Gamma + \lambda \ln p' \qquad (2.2)$$

in which λ represents the slope of the SSL, and Γ represents the value of the specific volume on the SSL in $\upsilon - \ln p'$ space at p' = 1 kPa (Sharma, 2004). If the term of *void ratio* is used instead of *specific volume*, the state parameter can be simplified as: $\psi = e_o - e_{cs}$; where e_0 and e_{cs} are the initial void ratio and critical void ratio at steady state, respectively (Phan et al., 2016). The positive value of the state parameter indicates the sand tends to contract (above SSL), and the negative value indicates the sand tends to dilate (below SSL).

CHAPTER 3. EXPERIMENTAL PROGRAM AND METHODOLOGY

Introduction

This chapter introduces the detailed information of the tested materials from Puerto Rico (PR sand) and Ledge Point, Australia (LP sand), respectively, which including the sample sources and the scanning electron microscopy (SEM) images. To better understand the difference between calcareous sand and silica sand, Ottawa sand is selected as a control group. Additionally, a series of experimental studies on the PR sand, LP sand, and Ottawa sand are conducted to determine their particle size distributions, specific gravities, the maximum and minimum void ratios, and the carbon contents. The methodologies of static stress-strain response and quantifying relative particle breakage content are introduced in the end of this chapter, and the corresponding results will be discussed in Chapter 4 and Chapter 5.

Tested Materials

Calcareous sands vary based on sediment source and origin, mineralogy, water depth, and seawater chemistry, causing each type of calcareous sand to possess unique characteristics (Morse & Mackenzie, 1990). Many researche has been focused on calcareous sands from different locations, such as the Dog's Bay, Ireland (Coop, 1990; Golightly & Hyde, 1988; Hyodo et al., 1996), the Persian Gulf (Shahnazari et al., 2013), the west coast of Australia (Sharma & Ismail, 2006; Beemer et al., 2018), and the west coast of Puerto Rico (Catano & Pando, 2010; Morales-Velez, 2014). The investigated locations have high density of coastal constructions, such as, oil or gas platforms. Puerto Rico and Australia are abundant in not only energy resources but also tourism resources; therefore, it is important to study the calcareous sands from these two locations due to the abundance along the coastline coupled with the high density of coastal constructions and developments, such as port facilities, renewable industries, hotels,

platforms, and pipeline designs. Additionally, the comparison between calcareous sands from these two locations will provide a better understanding of the influence on the engineering properties with different sample characteristics. Both calcareous sands were collected from the seabed with a 10-meter water depth. Ottawa sand produced by US Silica was used as a control group, reflecting the difference between calcareous sands and silica sands.

Puerto Rico Sand (PR Sand)

Puerto Rico is an island located between the Caribbean Sea and the North Atlantic Ocean and is north of the equator. There are three major types of surficial sediments around Puerto Rico: terrigenous sediments with low carbonate content (< 25%); marine sediments with high calcium carbonate content (> 75%); and mixed sediments with calcium carbonate content between 25% and 75% (Scanlon et al., 1998). Surficial sediments in Cabo Rojo, in the southwest coast of Puerto Rico (Figure 3.1), fall in the category of marine sediments and were measured with more than 90% calcium carbonate ($CaCO_3$) (Morales-Velez, 2014); hence, samples from this location were selected as one of the tested materials for this study.

Figure 3.1. Location of Cabo Rojo, Puerto Rico

The scanning electron microscopy (SEM) imaging was performed by the Materials Analysis and Research Laboratory (MARL) at Iowa State University, and the SEM images of Puerto Rico sand are shown in Figure 3.2. The particles were scanned by 8x to 500x magnification lenses. The thin-walled mollusk and needle- or bar- shaped coral reefs control the grain structure of the Puerto Rico sand, and the septal particle structure are observed; therefore, the Puerto Rico sand can be characterized by significantly porous intra-structure.

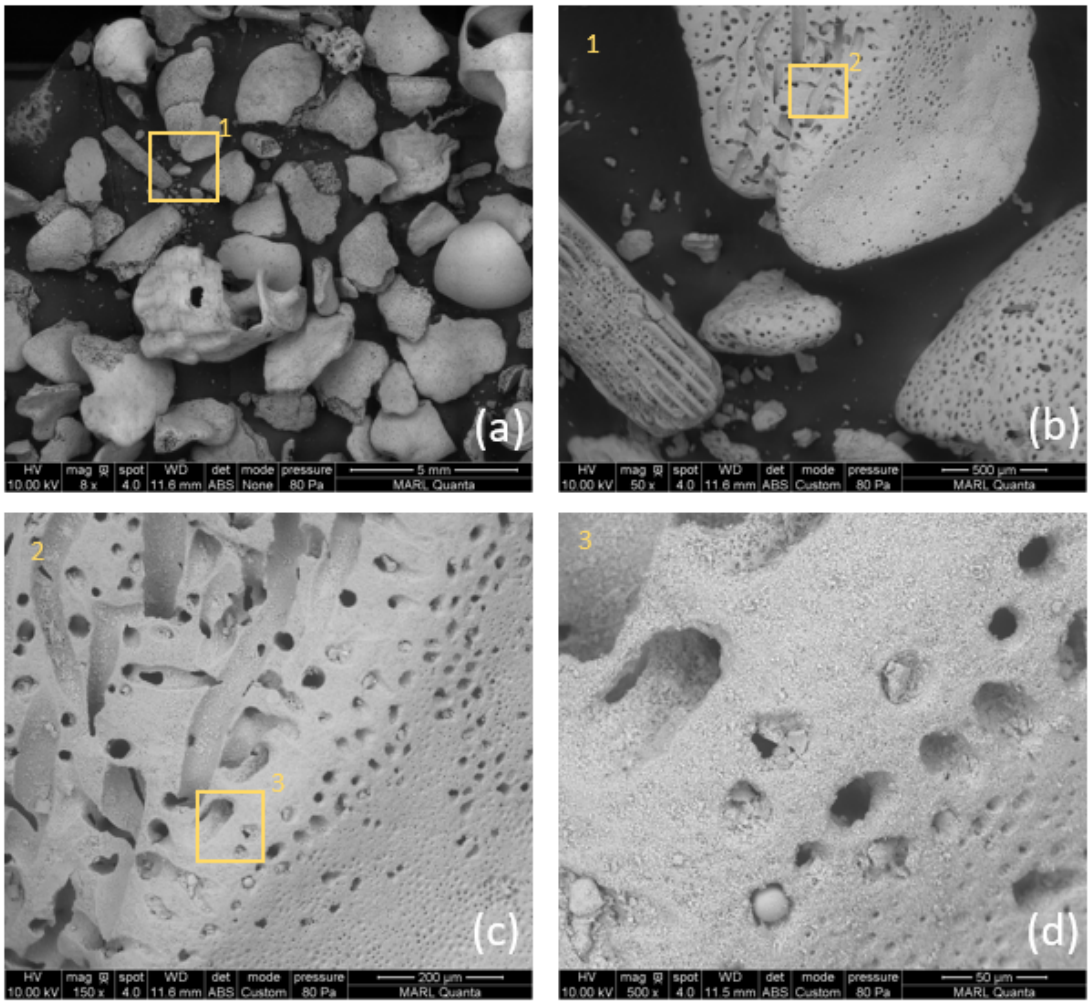

Figure 3.2 SEM Images of PR Sand

Ledge Point, Australia Sand (LP Sand)

Australia is surrounded by the Indian and Pacific oceans, and the Western Australia (WA) is the largest state of Australia, occupying the entire western third of the country. One of the other calcareous sands selected for the present study is from Ledge Point which is a small coastal township 105 km north of Perth, Western Australia (Figure 3.3). Sediments from Ledge Point are coastal Aeolian calcareous soil. As a part of the Quindalup dune system, calcareous sand dunes were formed along the shoreline of the Perth basin 10,000 years ago (Sharma, 2004).

Figure 3.3. Location of Ledge Point, Western Australia

The SEM images of Ledge Point sand are presented in Figure 3.4. Similar to PR sand, LP sand mostly consists of bioclastic grains with discernible marine organisms. With the same magnification lens scale, LP sand grains are smaller than those of the PR sand. The grain shape

of LP sand varies from angular to sub-angular, and even some grains show round shape. Porous structures were also observed, but with a less porous characteristic compared to the PR sand. As mentioned in the previously, the LP sand is aeolian sand, resulting in the finer grain size and lower inner-structure porosity.

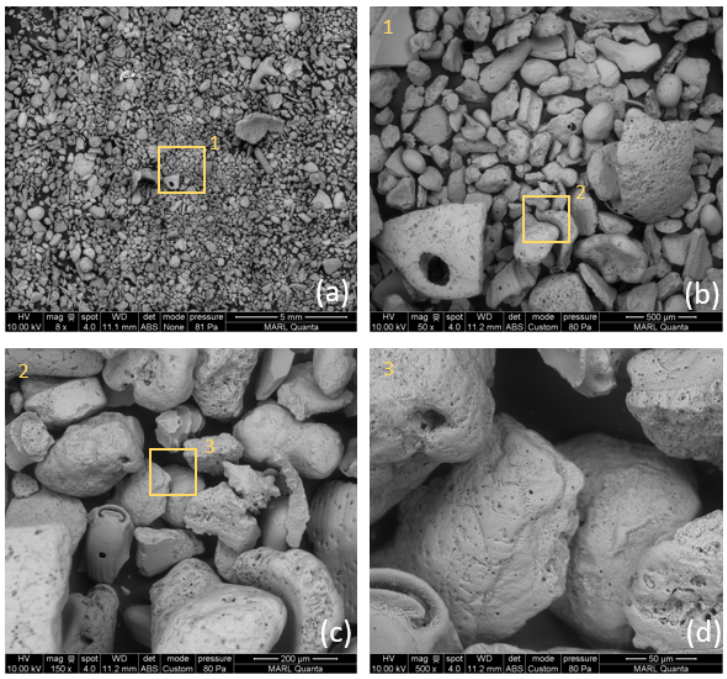

Figure 3.4. SEM Images of LP Sand

Ottawa Sand

Ottawa sand is mined near the Illinois and Fox Rivers, which closes to Ottawa, Illinois, and produced by US Silica. This type of sand is produced from a sedimentary rock and composed by rounded sand particles with more than 99% silicon dioxide (SiO_2) content that has a hardness of 7 in the Mohs scale. As shown in the SEM images in Figure 3.5, the grain shape of Ottawa sand are sub-rounded to rounded; most of the particle's surface shows an abraded texture with some specific points of etch polygonal marks in some of the grains (Bastidas, 2016).

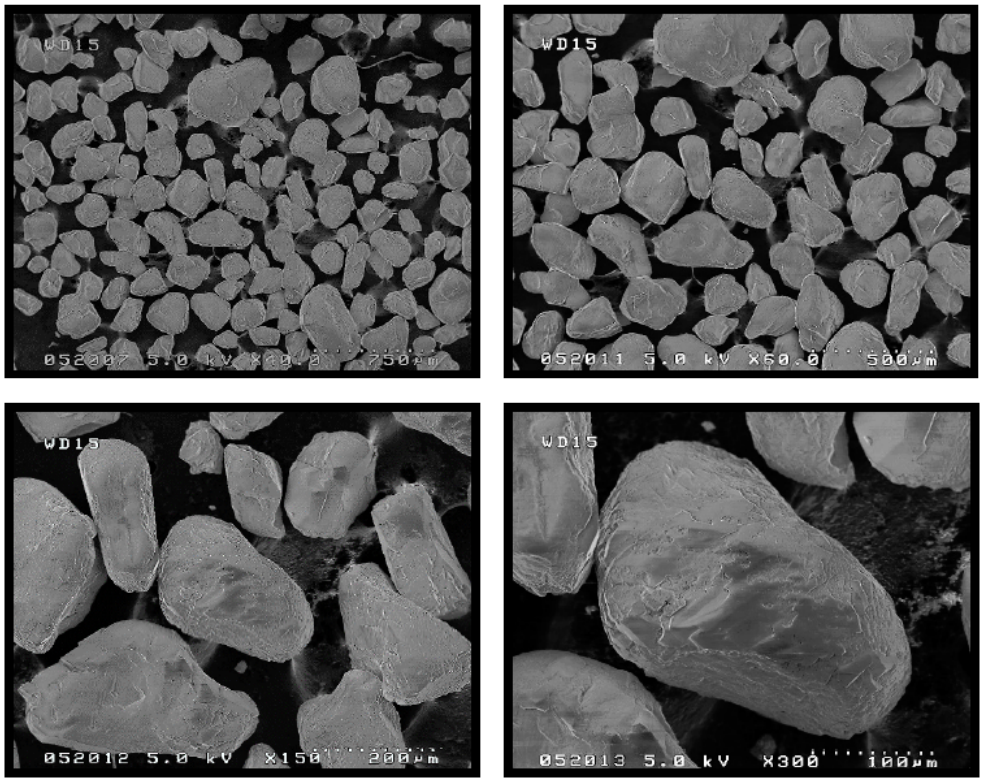

Figure 3.5. SEM Images of Ottawa F-65 Sand (Bastidas, 2016)

Compared to Ottawa sand, calcareous sand grains are in angular shapes and have obviously porous surface texture, which is because calcareous sands are composed of the debris of marine organism such as shells and corals, and the particles of chemical precipitation. Calcareous sands have high carbonate content (>90%), while the major chemical content of Ottawa sand is silicon dioxide (SiO_2 >99%). Additionally, the high carbonate content and porous grain structure lead to a relative low hardness of calcareous sand, making it easy to crush under the application of forces. These composition differences between calcareous sand and Ottawa sand result in the differences of their mechanical properties, which will be discussed in detail in the subsequent chapters.

Index Tests

Index properties, such as specific gravity, grain size distribution, minimum and maximum dry unit weight, were carried out to classify Puerto Rico sand and Ledge Point sand. To evaluate the particle breakage of calcareous sands after the application of the shear forces, sieve analysis, maximum and minimum dry densities, and maximum and minimum void ratio tests were performed on virgin and crushed calcareous sands. Due to the porous grains, low hardness, and irregular shape of the calcareous sand particle breakage is possible during sieving. To avoid this additional crushing due to sieving, a total shake time of 15 min was used as recommended (Hasanlourad et al., 2008; Zhang et al., 2005).

Grain Size Distribution

The grain size distribution curves of two calcareous sands and the Ottawa sand are plotted in Figure 3.6. The detailed parameters for these three sands are listed in Table 3.1. The grain sizes of Puerto Rico sand ranged between 4.75 mm (No. 4 sieve) and 0.075 mm (No. 200 sieve) with the uniformity coefficient (C_u) value of 3.25 and the coefficient of gradation (C_c) value of 1.14. For the Ledge Point sand, the grain size which was distributed from 2 mm (No. 10 sieve) to 0.075 mm shows a more uniform gradation with the C_u and C_c values of 2.40 and 1.20, respectively. Both calcareous sands had more than 50% of coarse fraction passing No. 4 sieve and had less than 5% passing No. 200. In terms of the Unified Soil Classification System (ASTM D2488-17), both Puerto Rico and Ledge Point calcareous soils were classified as poorly graded sands (SP).

In terms of the sieve analysis results from Figure 3.6, the Ottawa sand was classified as poorly graded sands (SP) ranging between 0.075 mm to 1.18 mm. The values of uniformity coefficient and coefficient of gradation are as follows: $C_u = 1.72$ and $C_c = 1.33$. Compared to the

other two calcareous sands, Ottawa sand obtained the most uniform grain size distribution and the greatest value of C_c. In terms of the grain size distribution curves, Ottawa sand can be defined as fine to medium sands; calcareous sand from Ledge Point was also fine to medium sand, and the Puerto Rico calcareous sand can be regarded as medium to coarse sand.

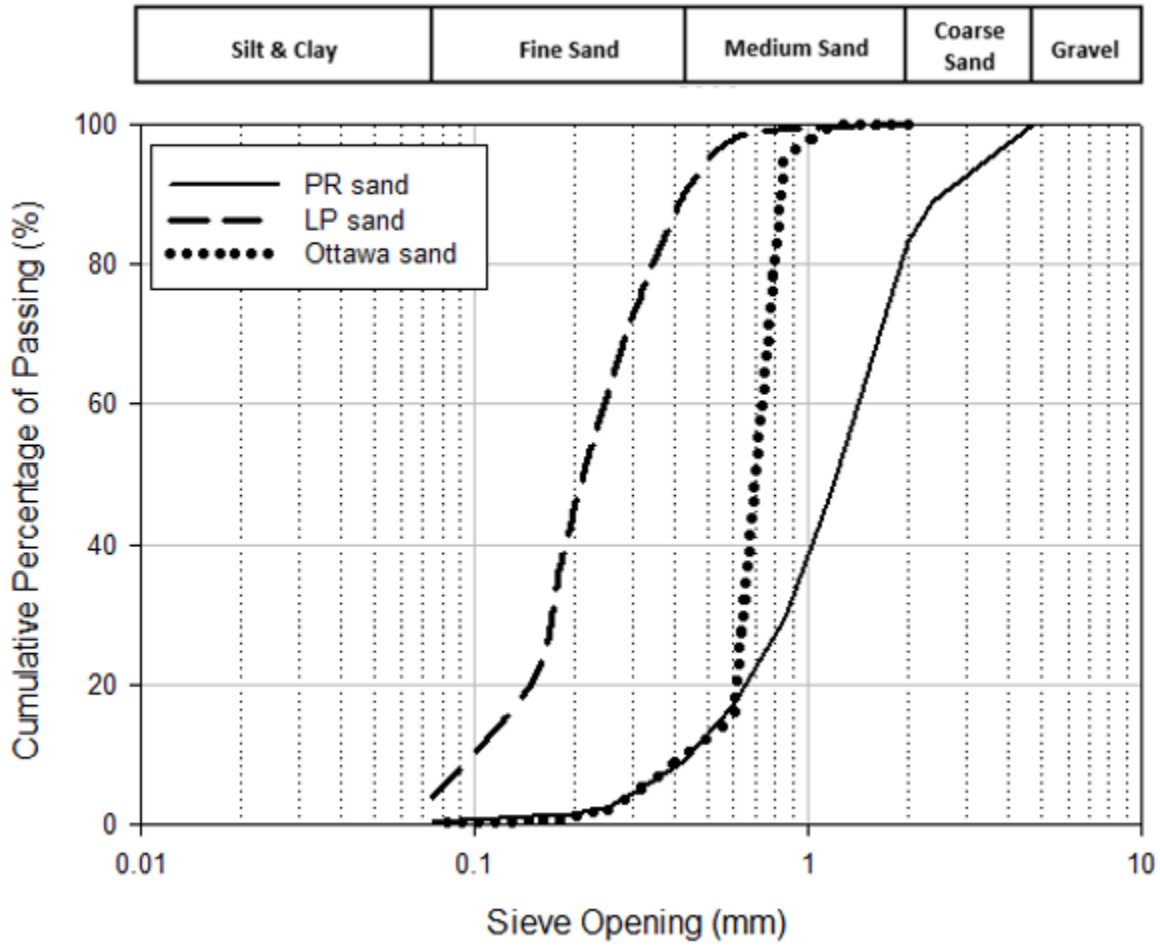

Figure 3.6. Particle Size Distributions of PR Sand, LP Sand, and Ottawa Sand

Table 3.1. Sieve Analysis Results of PR Sand and LP Sand

Parameter	PR Sand	LP Sand	Ottawa Sand	Method
D_{10} (mm)	0.45	0.10	0.43	ASTM C136/C136M - 14
D_{30} (mm)	0.86	0.17	0.65	
D_{50} (mm)	1.22	0.22	0.71	
D_{60} (mm)	1.45	0.24	0.74	
C_u	3.25	2.40	1.72	
C_c	1.14	1.20	1.33	

Specific Gravity

Pycnometer test according to ASTM D854-14 was conducted to obtain the specific gravity (G_s) of each type of calcareous sand. Table 3.2 shows the specific gravity of the Puerto Rico sand (PR sand), the Ledge Point sand (LP sand), and the Ottawa sand. It can be observed from this table that the calcareous sands have a higher specific gravity (>2.7) compared to the silica sands.

Table 3.2. Specific Gravities of Tested Materials

Sand Type	PR Sand	LP Sand	Ottawa Sand
Specific Gravity (G_s)	2.74	2.76	2.65
Method	ASTM D854-14		

Maximum and Minimum Void Ratio

Three methods were used to determine the minimum dry unit weight ($\Upsilon_{d\ min}$) and corresponding maximum void ratio (e_{max}) in this study: (1) ASTM D4254-00 method, (2)

Ruffatto's (2013) method, and (3) the Japanese method (2009). The ASTM D4254-00 method was carried out using the following procedures: (i) place the funnel spout on the bottom of the mold and hold the funnel vertical; (ii) fill the funnel with oven-dried sand by adjusting the height of the spout to maintain a free fall of the soil of about 13 mm without the spout contacting the already deposited sand; (iii) keep filling the mold until reaches approximately 13 mm to 25 mm above the top of the mold, and (iv) trim off the excess sand with a straightedge. The Japanese method has similar procedures as the ASTM method, except it used a cylinder shape for the mold. A square mold was used for ASTM method to compare with the Japanese method which used a cylinder mold. For Ruffato's method, approximately 400 g of oven-dried sand sample was placed in a 1000 ml glass cylinder; the cylinder was then turned up-side down by covering the top of the cylinder and repeating this action for 45 seconds (Bastidas, 2016). Three tests were conducted for each method to take average values.

Table 3.3. $\gamma_{d\ min}$ and e_{max} of PR Snad and LP Sand Determined by Different Methods

Method	PR Sand			LP Sand		
	$\gamma_{d\ min}$ (KN/m^3)	e_{max}	Standard Deviation	$\gamma_{d\ min}$ (KN/m^3)	e_{max}	Standard Deviation
ASTM D4254-00	6.85	2.92	0.12	12.89	1.10	0.02
Ruffatto's Method	7.86	2.42	0.01	12.87	1.10	0.02
Japanese Method	7.32	2.67	0.09	12.89	1.10	0.02

Table 3.3 showed the results of $\gamma_{d\ min}$ and e_{max} of PR sand and LP sand which are determined by the ASTM D4254-00, Ruffatto's method, and the Japanese method. The testing results of LP sand followed by all three methods were approximately the same, so the results from ASTM method were selected as the final results with $\gamma_{d\ min}$ = 12.89 KN/m^3 and e_{max} = 1.10, respectively. The results of Puerto Rico sand from Ruffatto's method and the Japanese method obtained similar values, but both results were lower than that of the ASTM method. The possible reason might be because that the medium to coarse Puerto Rico sand grains were stuck at the corners of square mold used for ASTM method, while the same problem did not happen when conducting the other two method with cylinder mold. Therefore, more air space was created, and less sand was taken into the square mold resulting in a lower minimum dry unit weight and a higher void ratio. Additionally, three testing results which were taken based on Ruffatto's method showed a smaller standard deviation than the results of the Japanese method. Therefore, the results of Ruffatto's method were taken as the final results. The minimum dry unit weight of Puerto Rico sand was determined to be 7.86 KN/m^3 and the corresponding maximum void ratio was 2.42. Compared with the results of PR sand and LP sand, there was not a big difference for the fine-grained soils (LP sand) with different methods and molds to determine $\gamma_{d\ min}$ and e_{max}. However, for the coarse-grained soils, such as PR sand, Ruffatto's method provided more accurate results, and the cylinder mold was better than the square mold.

The ASTM D4253-00 method, Ruffatto's method, and the Japanese method were also used to determine the maximum dry unit weight ($\gamma_{d\ max}$) and the minimum void ratio (e_{min}). For the ASTM D4253-00, the mold was filled with oven-dried sand in the same way as the ASTM D4254-00; then a surcharge base plate was placed on the surface of the sand, and the mold was attached with surcharge to the vibrating table. The recommended vibration time is 6 min to 8 min

at 60 Hz (0.33+/- 0.05 mm amplitude) or at 50 Hz (0.48 +/- 0.08 mm amplitude). Ruffatto's method was conducted by pouring around 400 g of oven-dried sand into the 1,000 ml plastic cylinder with the increments of 25 g. The plastic cylinder was tapped 8 times after placing each increment by using a rubber hammer with a 45 mm diameter. Likewise, for the Japanese method, the sand sample was divided into 10 lifts of the same mass in the mold with the collar. After each lift was filled, the mold was rotated and vibrated by hitting it 100 times with the 45-mm diameter rubber hammer. The collar of the mold was then removed when the mold was filled, and the excess sand was trimmed off. Three tests were conducted for each method to take average values.

Table 3.4. $\gamma_{d\,max}$ and e_{min} of PR Sand and LP Sand Determined by Different Methods

Method	PR Sand			LP Sand		
	$\gamma_{d\,max}$ (KN/m^3)	e_{min}	Standard Deviation	$\gamma_{d\,max}$ (KN/m^3)	e_{min}	Standard Deviation
ASTM D4254-00	8.44	2.18	0.0001	14.10	0.92	0.04
Ruffatto's Method	9.50	1.83	0.01	14.40	0.88	0.02
Japanese Method	9.80	1.74	0.01	14.50	0.87	0.02

According to the results from these three methods shown as in Table 3.4, Ruffatto's method and the Japanese method still obtained the similar values of results, while the ASTM method exhibited higher values for both PR sand and LP sand. Sand samples densified layer by

layer, as in Ruffato's method and the Japanese method, resulted in more accurate results, rather than densifying the sand sample with entire one layer by a surcharge plate which the ASTM method did. Additionally, densification by a surcharge may have a higher risk of leading to sand particle breakage. In addition, the Japanese method led to the highest value of $\Upsilon_{d\ max}$ and the lowest value of e_{min} of PR sand, which was because the Japanese method had more densified layers than Ruffatto's method. Therefore, the results from Japanese method were selected as the final results for both PR sand and LP sand. Table 3.5 summarizes the final testing results for PR sand, LP sand, and the control group of Ottawa sand.

In terms of the results, calcareous sand has higher maximum and minimum void ratios compared to silica sand due to the intraparticle void structure of calcareous sand. The PR sand with the coarser grains obtained higher maximum and minimum void ratios than those of the LP sand.

Table 3.5 Summary of the Maximum and Minimum Dry Unit Weight and Corresponding Void Ratios of PR Sand, LP Sand, and Ottawa Sand.

Properties	PR Sand	LP Sand	Ottawa Sand
$\Upsilon_{d\ min}$ (KN/m^3)	7.86	12.89	14.60
e_{max}	2.42	1.10	0.78
$\Upsilon_{d\ max}$ (KN/m^3)	9.80	14.50	16.99
e_{min}	1.74	0.87	0.53

Carbonate Content Determination

Calcium carbonate ($CaCO_3$) is one of the major chemical components of calcareous sand, however some sands may also contain a small amount of magnesium carbonate ($MgCO_3$). The titration test introduced by British Standard (BS-1377-3 1990) was selected to determine the carbonate content in an accurate way. The carbonate content of the PR sand was determined as 95%, and for the LP sand, the carbonate content was 93%. The test was conducted by soaking 5 g of tested calcareous using 100 ml of the hydrochloric acid (HCl) solution with a concentration of 1 mol/L for at least 1 hour; 25 mL supernatant liquid was then transferred by a pipette to a conical flask. Several drops of the indicator solution were added to the flask, and the mixed solution was titrated with the 1 mol/L sodium hydroxide (NaOH) solution until the color change was observed. The carbonate content of the calcareous sand was calculated based on the chemical reaction equation:

$$CO_3{}^{2-} + 2HCl = Cl_2{}^{-} + H_2O + CO_2 \uparrow \quad (3.1)$$

Comparison with Other Calcareous sand from the Literature

Besides the PR and LP sand in the present study, other calcareous sand with different origins from the literature was involved for comparison. The physical properties and the carbonate content were summarized in Table 3.6. The calcareous sand from the work of Shahnazari et al. (2013) were originated from the northern shores of the Persian Gulf. The HI soil was from Hormuz Island, and the BP soil was from Bushehr Port. The PR soil (Catano & Pando, 2010) was obtained from the Puerto Real beach in southwest Puerto Rico. Sharma (2004) investigated the properties of calcareous sand from Australia. One is from Goodwyn (GW), and the other one is from Ledge Point which is the same origin of the LP sand used in the present study.

Table 3.6. Physical Properties and Carbonate Content of Different Calcareous Sand

Soil	Grain Shape	Carbonate Content	D_{50} (mm)	C_u	C_c	e_{max}	e_{min}	G_s
PR	Angular	95%	1.22	3.22	1.13	2.42	1.74	2.76
LP	Sub-angular	93%	0.22	2.40	1.20	1.10	0.87	2.74
HI (Shahnazari et al., 2013)	Angular	53%	0.78	4.47	0.87	0.909	0.625	2.76
BP (Shahnazari et al., 2013)	Sub-angular	44%	0.43	3.2	0.84	0.726	1.051	2.71
PR (Catano & Pando, 2010)	Angular	92.8%	0.38	2.1	1.07	1.71	1.34	2.86
LP (Sharma, 2004)	Sub-angular	91%	-	1.835	-	1.21	0.90	2.76
GW (Sharma,2004)	Angular	94%	-	4.604	-	2.317	1.266	2.72

Based on the summarized results in Table 3.6, the specific gravities of all the involved calcareous soils were higher than 2.7. The majority of the carbonate contents of calcareous soils were greater than 90%, but the HI and BP soils from the Persian Gulf only had the carbonate contents of 53% and 44%, respectively. The physical properties of the LP sand in the present study were similar to the results of the calcareous sand from the same origin investigated by Sharma (2004). Overall, calcareous soil is different from site to site. Calcareous soils from different origins had different characteristics, resulting in different engineering behavior when subjected to load.

Particle Crushing

Calcareous sands have a higher potential of crushing. Particle crushing influences the shear strength and stress-strain response, especially under undrained shearing condition (Hardin, 1985; Hyodo et al., 1999). In this study, the calcareous sands are crushed by two methods: triaxial CD tests and one-dimensional (1-D) consolidation tests. The dry sand samples are used for the two methods to maximize the particle crushing content. The results are collected and discussed in Chapter 5 to investigate the influence of different loading mechanisms on particle breakage. The steps of sample preparation and testing procedures are introduced in the following sections.

Triaxial Consolidation Drained (CD) Test

It was improved by Shahanazari and Rezvani (2013) that the drained condition led to more particle breakage than that of undrained condition; therefore, the triaxial CD tests are selected to create particle breakage in the present study. There are two types of devices used to perform the triaxial CD tests: 1) manual setups and 2) fully automated configurations. To investigate the influence on particle breakage with and without water, the manual setups are used to perform the triaxial CD tests on dry calcareous sand samples, and the fully automated

configurations are used to perfume the tests on saturated samples. In addition, the fully automated configurations can also record the volumetric change as the strain increased.

The manual setups consist of a GeoJac^{TM} digital load actuator connecting to a computer, a load frame, a confining chamber with a top cap and a bottom base, and a pressure control panel (Figure 3.7). Sample preparation and testing procedures followed ASTM D7181-11 method with some modifications as described below. The testing specimen was a cylindrical shape with a diameter of 7.11 cm and a height of 14.22 cm. A thicker latex membrane with the thickness of 0.06 cm was used to prevent membrane breakage or damage due to the high angularity of calcareous sand. The membrane was attached on the pedestal sitting on the bottom base using O-rings. Then, a split mold was assembled and clamped tightly around the latex membrane, and the air between the membrane and the split mold was vacuumed to make sure the membrane is stretched firmly against the mold wall. A porous disc and a piece of filter paper were applied on the base pedestal, and the predetermined amount of oven-dried calcareous sand was poured into the mold using the dry pluviation method to obtain the desired relative density (D_r = 50%). Another porous disc and filter paper were placed on the top of the sand sample; the top cap was then applied and sealed by membrane with O-rings. Before removal of the split mold, a small amount of negative pressure was applied inside the sample by vacuum to make sure the uncemented sand sample could stand itself without the holding of mold. The top cap was attached, and the confining pressure in the cell was applied. De-aired water was filled into the chamber with a seating confining pressure to hold the tested sample during flushing. As mentioned previously, water was not involved inside the sample during the manually triaxial CD test, so the B check step for sample saturation determination was skipped. After the 15 min consolidation with the chamber pressure of 200 kPa, the sample was sheared by a rate of

15%/hour with the strain limit of 20%. The apparatus of the triaxial CD test is limited to run within the low-pressure range; therefore, the commonly used confining pressure levels of 100 kPa, 300 kPa, and 400 kPa, were carried out to obtain different particle crushing contents. Sieve analysis and maximum and minimum void ratios were determined after each triaxial CD test.

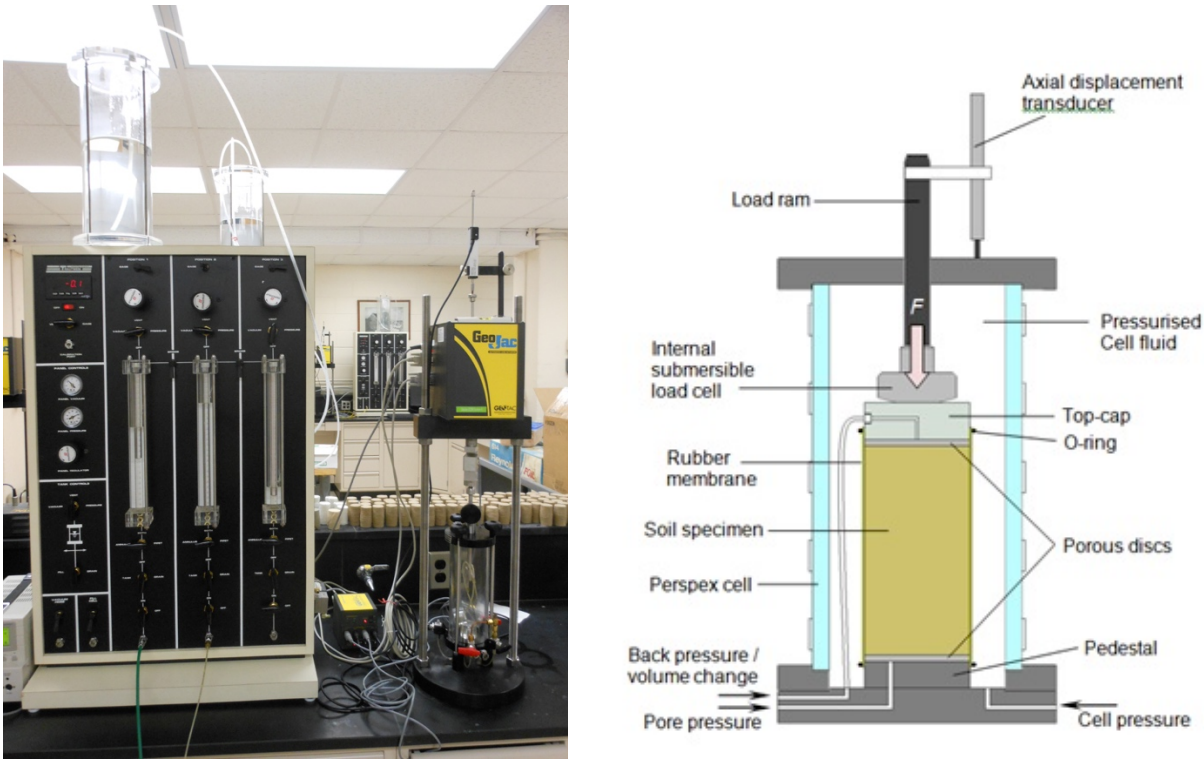

Figure 3.7. Manually Triaxial Apparatus and Sample Schematic Diagram (GDS Guideline)

The fully automated configurations consist of the TruePath Automated Stress path System which is GeoTAC's most advanced system incorporating state of art data acquisition and feedback control. As shown in Figure 3.8, a TruePath system consists of a Sigma-1 load frame, two DigiFlow pressure volume actuators (control the pressure inside and outside of the sample), and a high-resolution analog data acquisition system all connected to a computer through TestNet. The system also includes external and internal load cells, one deformation sensor, three pressure sensors, and a temperature sensor. The TruePath system can automatically record the volumetric change of a saturated sample by collecting the water increased or decreased in the

internal load cell during the test. The TruePath test sample with the relative density of 50% was prepared as the same procedures as the manually triaxial CD test. After the sample applied to the device, carbon dioxide (CO_2) gas with a low-pressure level (around 70 kPa) was used to flush through the sample from bottom to top to displace the air. The confining pressure was held to approximately 35 kPa higher than the flushing pressure to control swelling of the specimen (ASTM D4767-11). Then the sample was flushed and saturated with de-aired water to achieve 95% saturation. After saturated, the sample was consolidated for 15 min and was sheared with the strain limit of 20% and the confining pressures of 100 kPa, 300 kPa, and 400 kPa.

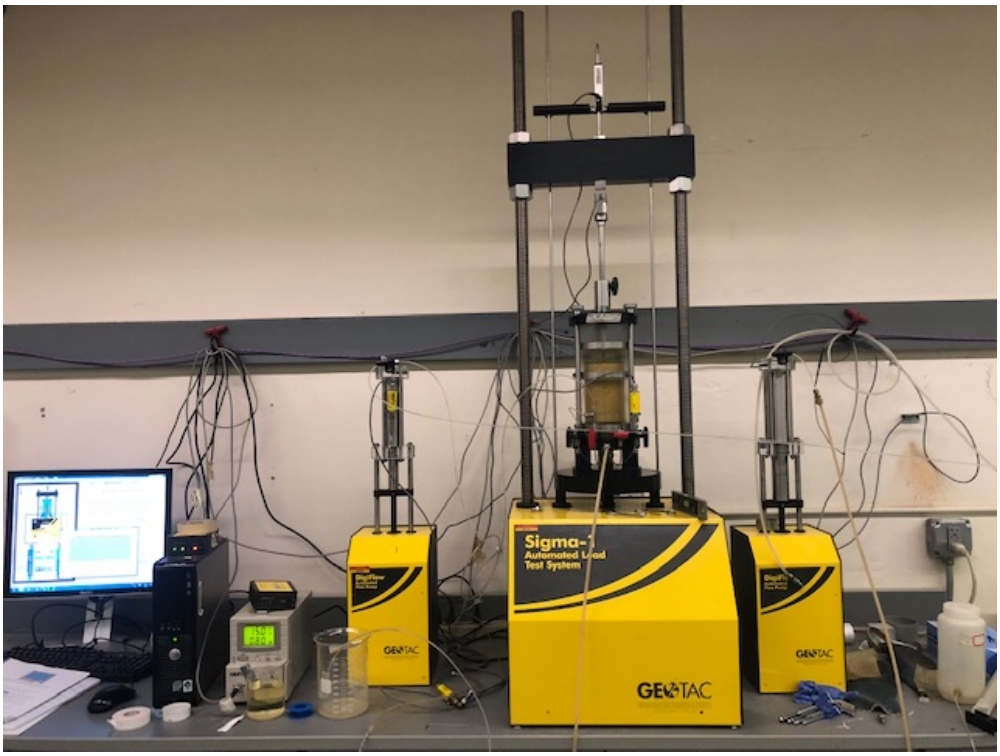

Figure 3.8. Fully Automated TruePath Configurations

One-Dimensional (1-D) Consolidation Test

The apparatus of 1-D consolidation test is similar to that of the triaxial test but consists of a shorter load frame and a different sample mold (Figure 3.9). For this test, the sample size was 6.35 cm in diameter and 2.54 cm in height with the target relative density (D_r) of 50%. A porous

disc and a piece of filter paper were placed on the recess located at the bottom of the plastic mold, followed by placing the steel confining ring. The predetermined amount of oven-dried calcareous sand was filled into the steel confining ring by the dry pluviation method. Then, another filter paper and porous disc was placed on the top of the sand sample; the top cap of mold was attached and fixed tightly. The consolidation phase was conducted dry. Due to the loading limit of the digital actuator, the stress levels selected for crushing were 2400 kPa and 4800 kPa. Sieve analysis and maximum and minimum void ratios were determined after each consolidation test.

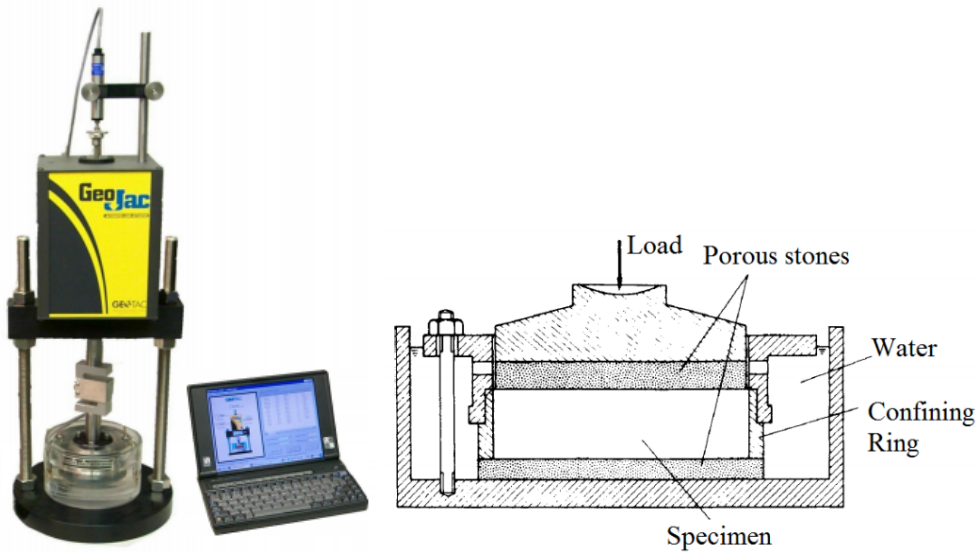

Figure 3.9. One-Dimensional Consolidation Apparatus and Sample Schematic Diagram

Quantifying Crushing Content

Different methods of quantifying the degree of particle crushing have been proposed by various studies. In 1967, Lee and Farhoomand defined a parameter as relative crushing, which is a ratio of D_{15i}/D_{15a}, where D_{15i} represents the diameter through which 15% of particles of the original material pass, and D_{15a} is the diameter through which 15% of the particles pass after being subjected to stress. Later in 1974, Lowrison suggested that the content of crushing can be quantified by evaluation of the increase in the surface area of the particles after crushing.

However, quantifying particle crushing based on passing a specific sieve size is not appropriate. Hardin (1985) illustrated that the breakage of particles terminated when the soil gradation curve achieved a stable condition. He also came up with a method to assess particle crushing. This method is still used in recent investigations. According to Hardin's method, the changes in the particle size distribution curve before and after crushing are determined and the final stable condition was reached when all particles were smaller than 0.075 mm. Then, the particle breakage of soil can be calculated from equation: $B_r = \frac{B_t}{B_p}$, where B_r represents the relative particle breakage, B_t is the area between the initial and final gradation curves, and B_p is the area between the original particle size distribution curve and vertical line for particle size of 0.075 mm (U.S. sieve No. 200). Figure 3.10 shows the graph concept of Hardin's method.

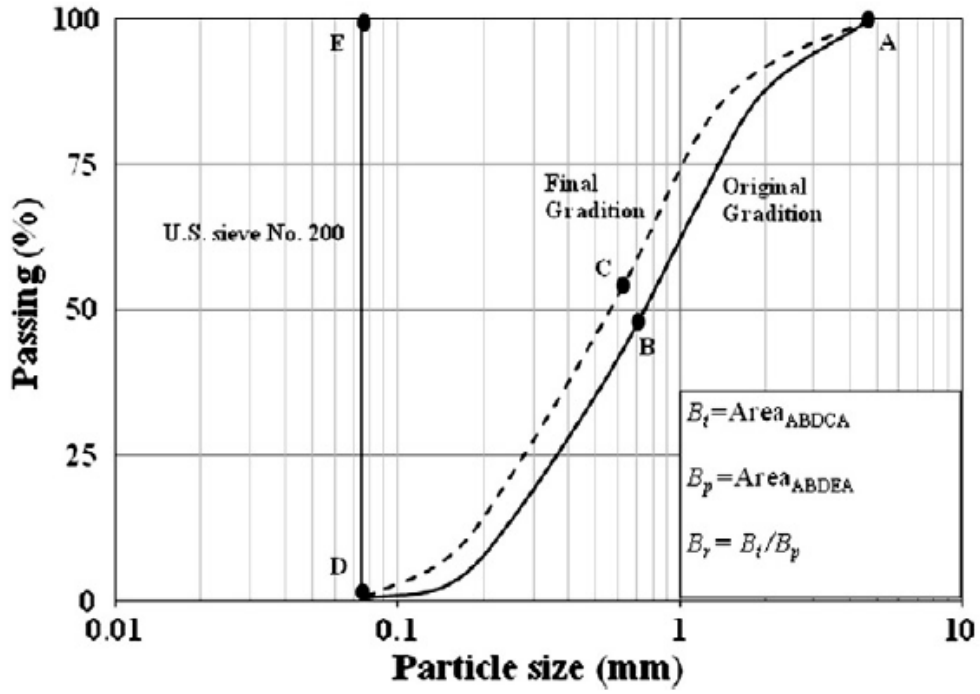

Figure 3.10. Definition of Particle Breakage Based on Hardin's Method (1985)

Monotonic Loading Response

Virgin sand samples and samples with different crushing contents were used to conduct the monotonic triaxial consolidation undrained (CU) tests to obtain the loading response, such as the stress-strain curves and the stress paths. The triaxial CU tests simulate the condition after the pile is ready and reflect the stress-strain response surrounding that pile. The apparatus and sample preparation for the triaxial CU tests was the same as the manually triaxial CD tests. The specimen was required to be above 95% saturation during the test; therefore, carbon dioxide (CO_2) gas with a low-pressure level (around 70 kPa) was used to flush through the sample from bottom to top to displace the air. The confining pressure was held to approximately 35 kPa higher than the flushing/back pressure to control swelling of the specimen (ASTM D4767-11). Then the sample was flushed and saturated with de-aired water. Once parameter B was greater than 0.95, the sample saturation was completed. A 15 min consolidation phase with the chamber pressure of 200 kPa was carried out, and then the shearing phase started at a rate of 1%/hour to reach final strain of 15%; all drainage valves were closed during this process.

For a better understanding of the loading behavior within the low-stress range, the triaxial CU tests at confining pressure of 200 kPa and 400 kPa were conducted on the two calcareous sands, respectively, to investigate the influence of various confining pressure on loading response and compare the difference between two sands. A confining pressure of 400 kPa was carried out on all crushed calcareous sands to evaluate the influence on their behavior with increasing crushing contents.

CHAPTER 4. STATIC LOADING BEHAVIOR ON CALCAREOUS SAND

This chapter summarizes the experimental results of the monotonic triaxial consolidated undrained tests on calcareous sands from Puerto Rico and Ledge Point. The monotonic consolidated undrained tests were conducted to provide a more comprehensive knowledge about the loading response of two calcareous sands from different regions, such as the stress-strain behavior, the effect of different confining pressures, the dilatancy and stiffness characteristics. In the end of the chapter, the comparison of the results of calcareous sand tests with results from the literature are discussed.

Monotonic Triaxial Test on Calcareous Sand

A series of monotonic triaxial consolidated undrained (CU) tests were conducted on Puerto Rico (PR) and Ledge Point (LP) sands. The calcareous sand specimens were prepared to a relative density (D_r) around 50%. Two levels of confining pressures (200 kPa and 400 kPa) were selected to investigate the calcareous sand behavior subjected to different confining stress levels.

Calcareous sands require a very high strain level to achieve steady state conditions compared to silica sand; however, during laboratory testing, steady state was only achieved in some tests (Catano et al., 2010; Zhang et al., 2009; Phan et al., 2016; Sharma, 2004). Steady state can be explained as a balance between the volumetric compression attributed to particle breakage and volumetric dilation due to particle rearrangement (Chandler, 1985; Baharom & Stallebrass, 1998). Been et al (1991) stated that the steady state of the same type of soils was found to be equal and independent of their sample preparation, initial density, and stress path. On the other hand, Shahnazari et al. (2012) illustrated that the calcareous soil sample experienced large deformations at large strains (>20%), resulting in unreliable results for engineering design. Therefore, in this study, the limited strain level for the triaxial CU tests was set as 15%.

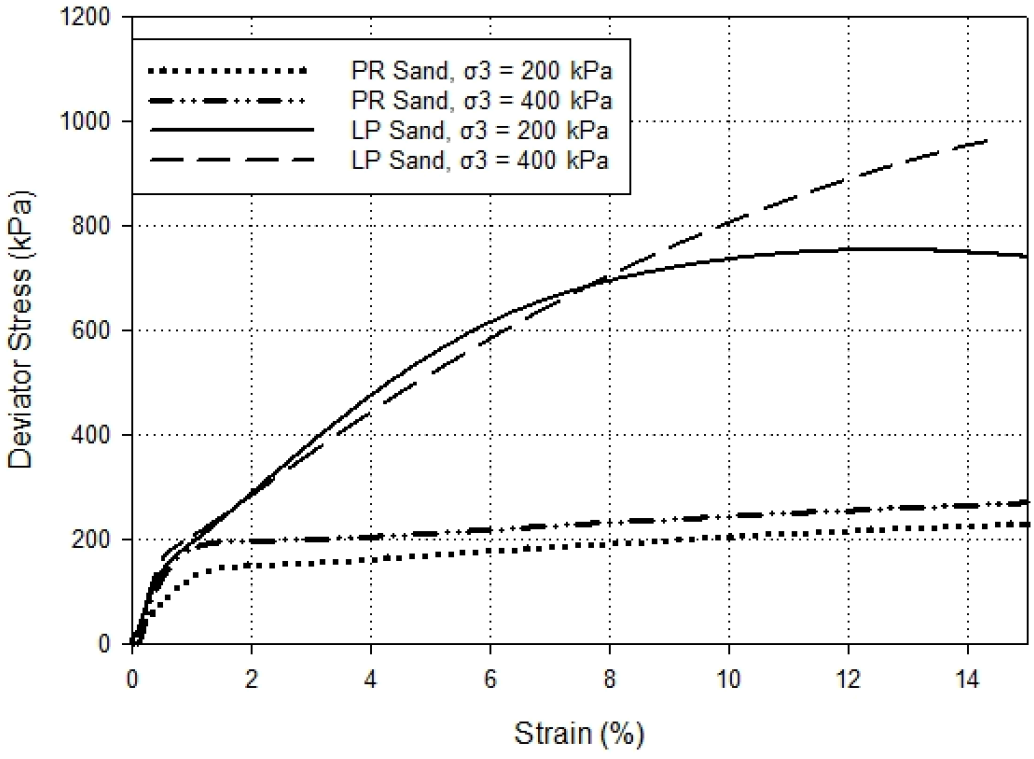

Figure 4.1. Stress-Strain Response of PR Sand and LP Sand

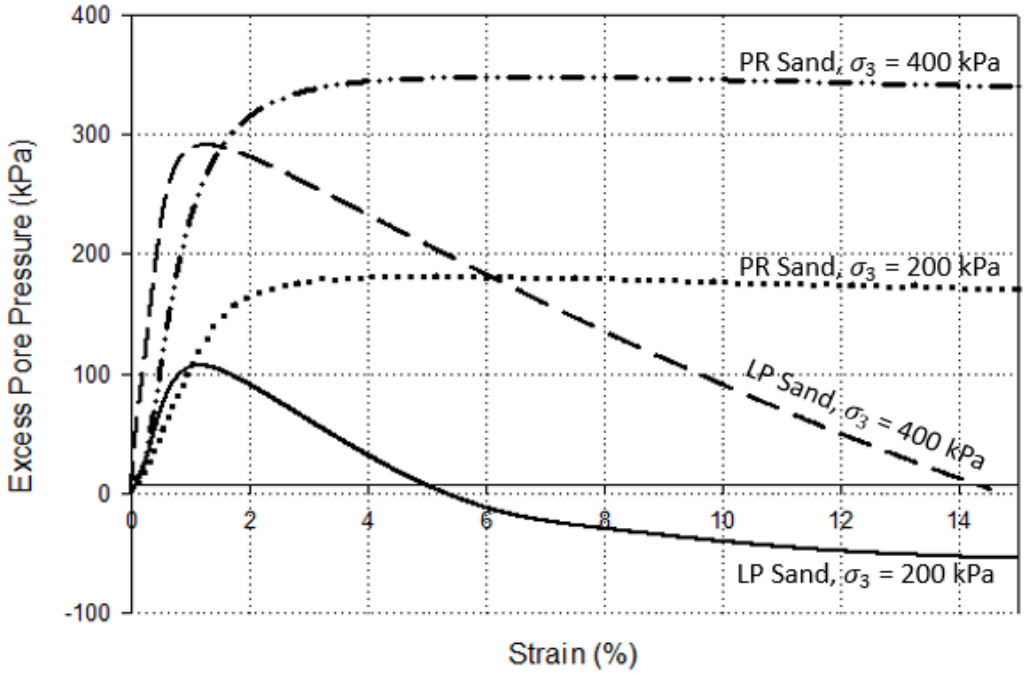

Figure 4.2. Excess Pore Pressure vs. Strain for PR Sand and LP Sand

In this study, the MIT stress path convention was used to determine the effective normal stress (p') and the deviator stress (q). The MIT effective normal stress, p', is the mean of the major and minor effective principal stress: $(\sigma'_1 + \sigma'_3)/2$, and the shear stress, q, was defined as: $(\sigma'_1 - \sigma'_3)/2$. The stress-strain curves and the excess pore water change, which obtained from the triaxial CU tests on both calcareous sands, are shown in Figure 4.1 and 4.2. In the stress-strain curve, the deviator stress is expressed as the equation: : $(\sigma_1 - \sigma_3)$. It can be observed that the LP sand gained a higher shear strength than the PR sand at both confining pressures (σ_3) of 200 kPa and 400 kPa. All four specimens exhibited a short approximately linear increase in deviator stress at the very beginning strain hardening process (within 0-0.5% of strain); then the deviator stresses increased as a non-linear trend with the strain increasing.

Table 4.1. Friction Angles of PR and LP Sand for Triaxial CU Tests

	Friction Angle (∅)	
	σ_3=200 kPa	σ_3=400 kPa
PR Sand	47.1°	45.6°
LP Sand	36.3°	33.3°

The stress-strain behavior of the PR specimens with two confining pressures were quite similar. They both reached the same high stress levels at the strain of 1%, and continued with a small stress increment until the end of tests with the friction angles (∅) of 47.1° ($\sigma_3 = 200\ kPa$) and 45.6° ($\sigma_3 = 400\ kPa$), respectively (Table 4.1). The LP specimen at a 200 kPa confining pressure achieved its maximum shear strength between 12% and 14% strain with the friction angle of 36.3°, and then showed a slight strain softening after the maximum strength achieved. Strain hardening was observed for the LP specimen at confining pressure of 400 kPa. The

friction angle for this specimen was 33.3°. For the PR sand, the shear strength increased with the increase of confining stress. The same phenomenon was observed in the LP sand. Hence, the higher confining pressure resulted in a higher shear strength for the same type of calcareous sand. With the same confining stress, the LP sand had a higher shear strength than the PR sand due to the LP sand obtaining a finer grain size distribution.

As illustrated in Figure 4.2, the excess pore pressure of the LP sand was initially increasing, and then started to decrease after reaching the maximum value around 1% strain level. Negative pore pressure values were obtained after 5% and 15% strain at confining pressures of 200 kPa and 400 kPa, respectively. The excess pore pressures of the PR sand were observed cumulating increasingly and were relatively stable after the maximum value achieved, but there was a slight decrease of pore pressure for both confining pressures according to the testing data. For confining pressure of 200 kPa, the PR sand exhibited a pore pressure decrease at the strain level of 5.5%. For confining pressure of 400 kPa, the pore pressure of the PR sand started to reduce at 8% axial strain. The reduction in excess pore pressure is caused by the soil dilation as the sand is sheared. Therefore, with the same confining pressure, the LP sand showed more of a dilative behavior in comparison with the PR sand. Additionally, the negative excess pore pressure resulted in a higher effective stress.

The effective stress paths were plotted in Figure 4.3. The stress paths for all four tested specimens showed an initial reduction in the mean effective principal stress (p'), and this was caused by the increase of excess pore pressure which indicating the contractive behavior. The excess pore pressure continued increasing until it reached the maximum pore pressure and then decreased. The decrease of the excess pore pressure led to an increase of the effective principal stress (p'), and the sample started to dilate. The point at which the specimen behavior converts

from contraction to dilation is the phase transformation (PT) point; the line drawn through the phase transformation points from the origin is defined as phase transformation (PT) line. In addition, the peak failure envelopes were obtained for both calcareous sands from the stress paths. The slope of the peak failure envelope for the PR sand was greater than that of the LP sand, resulting in higher internal friction angles for the PR sand.

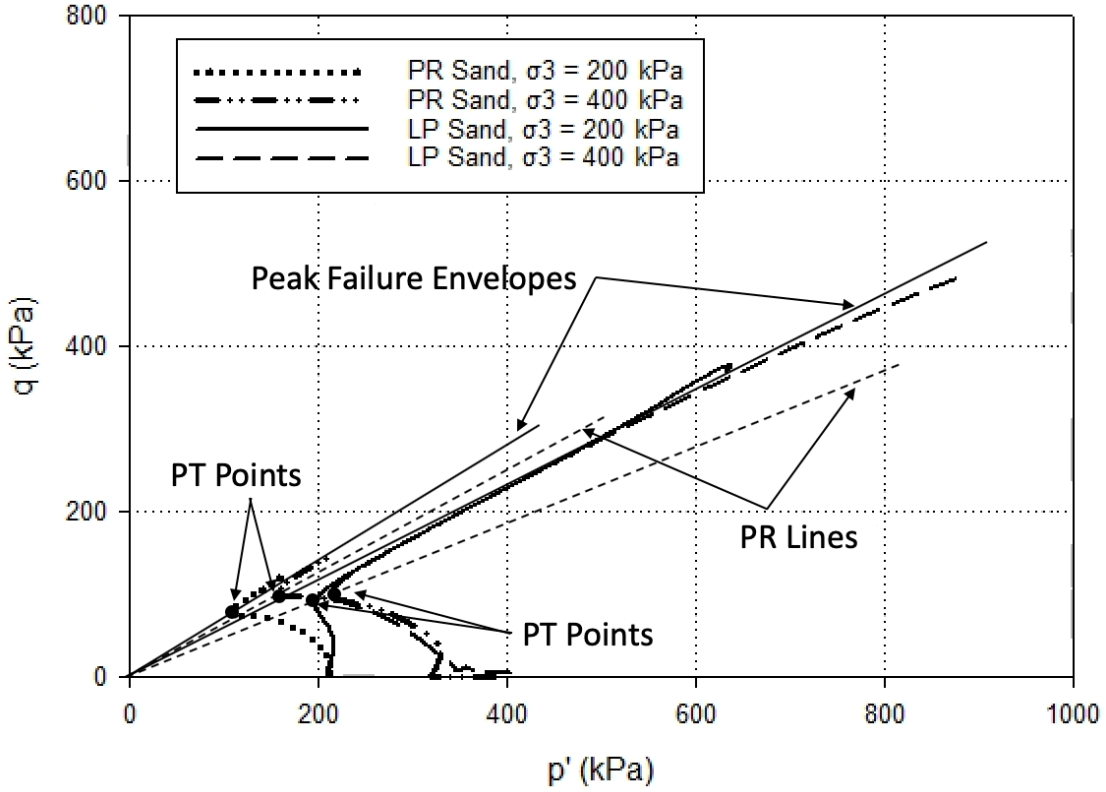

Figure 4.3. Stress Paths (p'-q plot) of PR Sand and LP Sand

For the medium dense (D_r = 50%) calcareous sands in this study, the sands initially contracted as it was sheared due to their high intraparticle void ratios. As the pore pressure increased, the contractive behavior continued until the sand grains started interlocking. With the additional stress applied, a bulk volume expansion or dilation was observed, and the pore pressure decreased at this stage.

Dilative behavior was observed clearly on both excess pore pressure curves and stress paths of the LP sand. The dilative behavior of the PR sand was not shown evidently on the pore pressure curves but was observed in the stress paths. With the same confining pressure, the PR sand was more contractive than the LP sand. Compared to the LP sand with finer grains and lower void ratio, the coarse-grained PR sand led to a higher void ratio and had a higher contractive potential during shearing.

Young's Modulus and Stiffness

The Young's modulus is a mechanical property measuring the stiffness of a soil and is required if an elasticity modeling approach is used. This modulus is not constant for a given soil, but it can be used to approximate the soil behavior with the given state of stress. The Young's modulus is determined by the following equation from axisymmetric conditions (Lade 2016):

$$\mathrm{E} = \frac{\Delta(\sigma_1 - \sigma_3)}{\Delta\varepsilon_1} \qquad (4.1)$$

Where, $\Delta(\sigma_1 - \sigma_3)$ is the change of deviator stress and $\Delta\varepsilon_1$ is the change of axial strain. Hence, the initial Young's modulus can be determined directly by the initial linear slope of the stress-strain curves. The initial Young's modulus (E_i) of the PR sand and LP sand are presented in Table 4.2. Based on the results, the LP sand obtained a higher initial Young's modulus than the results of the PR sand at confining pressures of 200 kPa and 400 kPa. For a certain type of the calcareous sand, the initial Young's Modulus ar the confining pressure of 400 kPa was greater than that at the confining pressure of 200 kPa. In other words, a higher confining pressure resulted in a greater initial Young's Modulus.

Table 4.2. Initial Young's Modulus of the PR Sand and LP Sand

Confining Pressure	Initial Young's Modulus (E_i), kPa	
	PR Sand	LP Sand
$\sigma_3 = 200\ kPa$	21,077	35,366
$\sigma_3 = 400\ kPa$	37,267	39,783

To better understand the response of the sands under shear loading, the stiffness (G), also defined as the shear modulus, is investigated in this study. In terms of Hooke's law for elastic behavior, the soil stiffness (G) can be expressed by the Young's modulus in Equation 4.2:

$$G = \frac{E}{2(1+\nu)} \quad (4.2)$$

in which, ν represents the Poisson's ratio, determined by Equation 4.3:

$$\nu = \frac{1}{2}\left(1 - \frac{\Delta\varepsilon_v}{\Delta\varepsilon_1}\right) \quad (4.3)$$

where, $\Delta\varepsilon_v$ is the volumetric strain increment, and $\Delta\varepsilon_1$ represents the axial strain increment. For undrained tests, the specimen volume is kept constant during shearing phase (i.e. volumetric strain increment is zero). Thus, the Poisson's ratio for the undrained tests was assumed as 0.5. An equation of stiffness can be derived by substituting the assumed Poisson's ratio as shown in Equation 4.4. This equation was also concluded by Sharma (2004).

$$G = \frac{E}{3} = \frac{\Delta(\sigma_1 - \sigma_3)}{3\Delta\varepsilon_1} \quad (4.4)$$

Based on the derived equation, the initial stiffness (G_i) can be obtained from the initial linear portion of the stress-strain curves from the monotonic triaxial CU tests. Since the stress-strain relationship of soil is non-linear, the stiffness is not constant for a given soil. This

changing parameter was represented by secant stiffness (G_{sec}) as the axial strain is increasing. The stress-strain response illustrated the degradation of soil stiffness as strain increased.

Table 4.3. Initial Stiffness of Puerto Rico Sand and Ledge Point Sand

Confining Pressure	Initial Stiffness (G_i), kPa	
	PR Sand	LP Sand
$\sigma_3 = 200\ kPa$	7,026	11,789
$\sigma_3 = 400\ kPa$	12,422	13,261

Table 4.3 shows the initial stiffness for Puerto Rico sand and Ledge Point sand, respectively. The results were consistent with the trend in initial Young's moduli, i.e. the higher the confining pressure the higher the initial stiffness corresponding to a higher shear strength. Normally, the high initial stiffness related to a high dry density and low void ratio. Triaxial CU tests were conducted on the calcareous sand samples with D_r = 50%. The initial void ratios were calculated using the relative density and maximum and minimum void ratios of the calcareous sand. The Puerto Rico sand had an initial void ratio of 2.08, and the initial void ratio for Ledge Point sand was 0.98. This lower initial void ratio results in a higher initial stiffness for Ledge Point sand.

The stiffness degradation is represented by the ratio of G_{sec}/G_i versus the axial strain in log-scale as shown in Figure 4.4 and Figure 4.5. The maximum stiffnesses of both calcareous sands were obtained at the beginning of shearing and were approximately equal to the initial stiffness. The stiffness degradation behavior for the PR sand and the LP were slightly different as shown in the figures below.

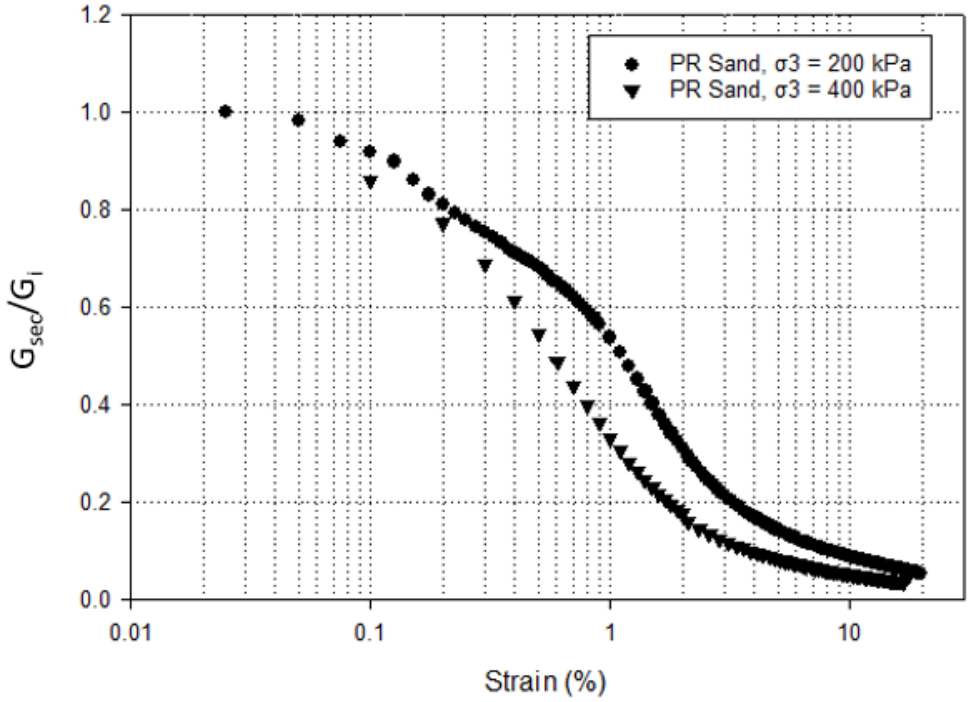

Figure 4.4 Stiffness Degradation for the PR Sand

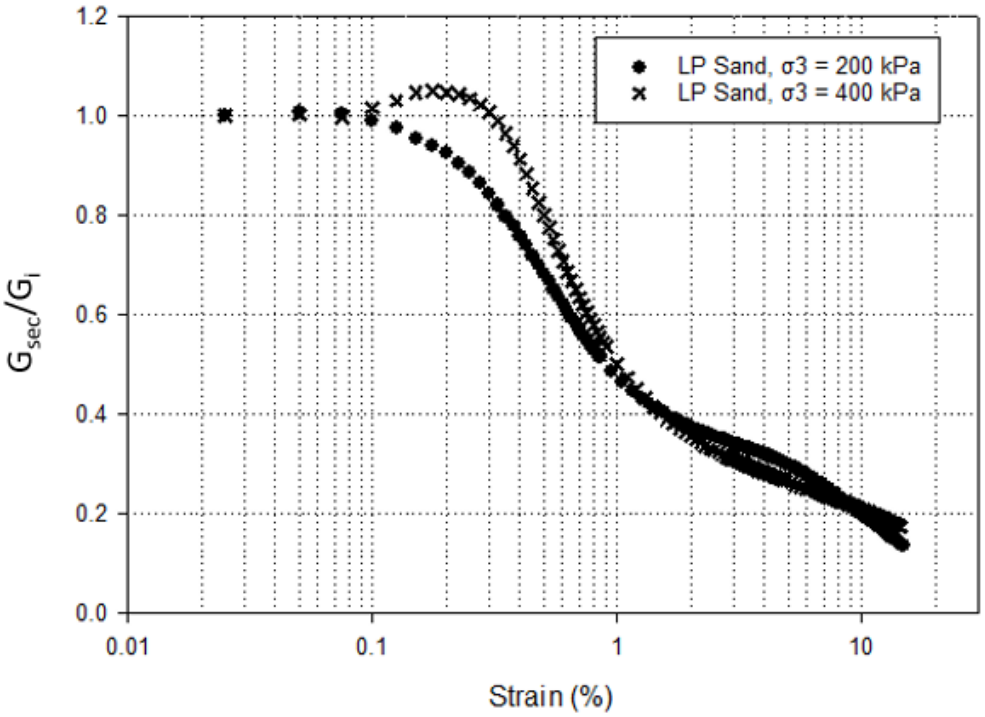

Figure 4.5 Stiffness Degradation for the LP Sand

For the PR sand, the stiffness decreased as the strain increased and kept decreasing until approximately to zero and remained in a constant range around zero till the end of testing or till the sample failure ($G_{sec} = 0$). For the PR sand at 200 kPa confining stress, the stiffness decreased gradually. The higher confining stress provided a higher initial stiffness, but this high confining stress resulted in a rapid stiffness degradation with increasing strain.

For the LP sand, the stiffness was constant until 0.03% strain and started to decrease after this stage. The strain corresponding to the end of this early stage was determined to be the "threshold" strain. Sharma (2004) defined a linear relationship before the "threshold" strain; beyond this strain, it is non-linear, resulting from a stiffness degradation. The stiffness of Ledge Point sand then kept decreasing to a low magnitude level close to zero until the end of testing. The "threshold" strain was not observed in Puerto Rico sand. It could be due to the slight particle crushing at the beginning of the test causing the plastic deformation.

Effective Stress Ratio

Although the deviator-strain diagram is conventionally used to present the stress-strain relationship of soil, it is sometimes difficult to compare the stress-strain behavior pattern especially when the result curves have large scale difference. The effective stress ratio, $\frac{\sigma_1'}{\sigma_3'}$, plotted against the strain increments for undrained tests, provides similar magnitudes. In this way, all testing data can be displayed in one diagram for better evaluation. Figure 4.6 (a) shows the relationship between effective stress ratio and axial strain on Puerto Rico and Ledge Point sand at confining stresses of 200 kPa and 400 kPa. Compared to the normal stress-strain plot shown in Figure 4.6 (b), four curves in stress ratio diagram all achieved peak values, but the positions of these peak values were not same with those obtained from the normal stress-strain diagram. Normally, the maximum effective stress ratio does not occur at the same when the

maximum deviator stress occurs for the undrained test, because they have different definitions and play different roles when analyzing geotechnical structures (Bolton, 1986; Lade, 2016). The maximum deviator stress is defined as the undrained strength. The maximum effective stress ratio is defined as the effective strength envelope, in other words, this value is used to define when the soil has failed.

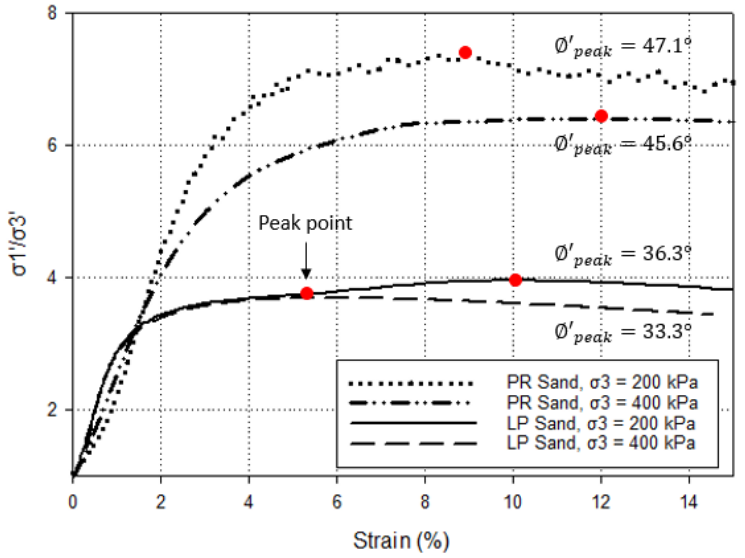

(a)

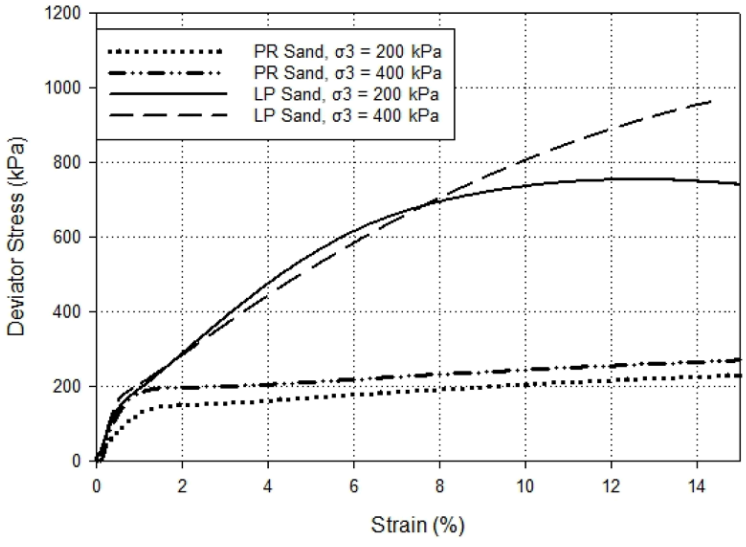

(b)

Figure 4.6. (a) Effective Stress Ratio Plot; (b) Normal Stress-Strain Plot from Triaxial Undrained Tests

The high stress ratio represents the high dilatancy potential resulting in a weak soil (i.e. low shear strength). The PR sand has a larger friction angle than the LP sand but has a lower strength due to particle breakage.

Comparison with Silica Sand

Ottawa sand was used to perform the triaxial consolidated undrained (CU) test with a confining pressure of 400 kPa. The Ottawa sand specimen was prepared with 50% relative density (D_r) using the same sample preparation procedures outlined in Chapter 3. The response of the Ottawa sand was used as a comparison for the two calcareous sands.

The stress-strain curves, the excess pore water curves, and the stress paths of PR, LP, and Ottawa sands were shown in Figure 4.7, Figure 4.8, and Figure 4.9. The deviator stress of medium dense Ottawa sand increased rapidly as the sample sheared. The maximum value of the deviator stress was achieved around 6% strain. After the maximum strength, a gradual strain softening occurred until the end of the test. For the LP sand, the strength increased gradually reaching a maximum deviator stress at 15% strain, which is approximately the same as the final strength of Ottawa sand at 15% strain. Based on the increasing trend, it can be inferred that the strength of the LP sand would exceed the strength of Ottawa sand if the strain is greater than 15%. According to the stress-strain curves, the PR sand had the lowest shear strength. The maximum deviator stress of the PR sand achieved within 15% strain was 300 kPa, while the maximum deviator stresses of the LP sand and Ottawa sand were 967 kPa and 1080 kPa, respectively.

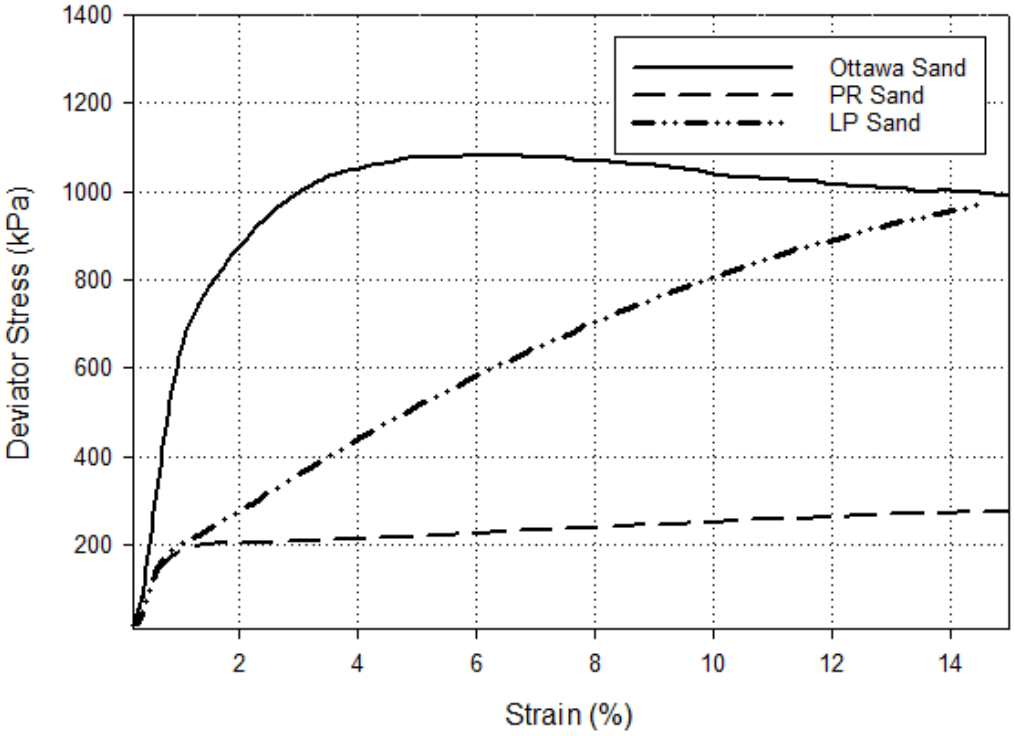

Figure 4.7. Stress-Strain Curves for PR Sand, LP Sand, and Ottawa Sand

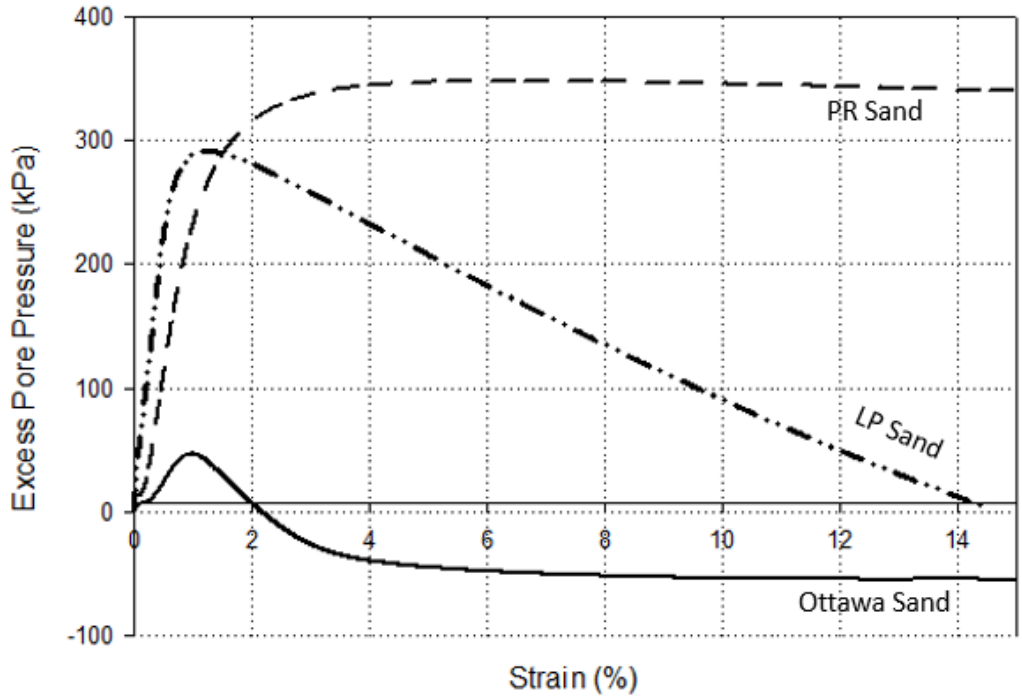

Figure 4.8. Excess Pore Water Pressure of PR Sand, LP Sand, and Ottawa Sand

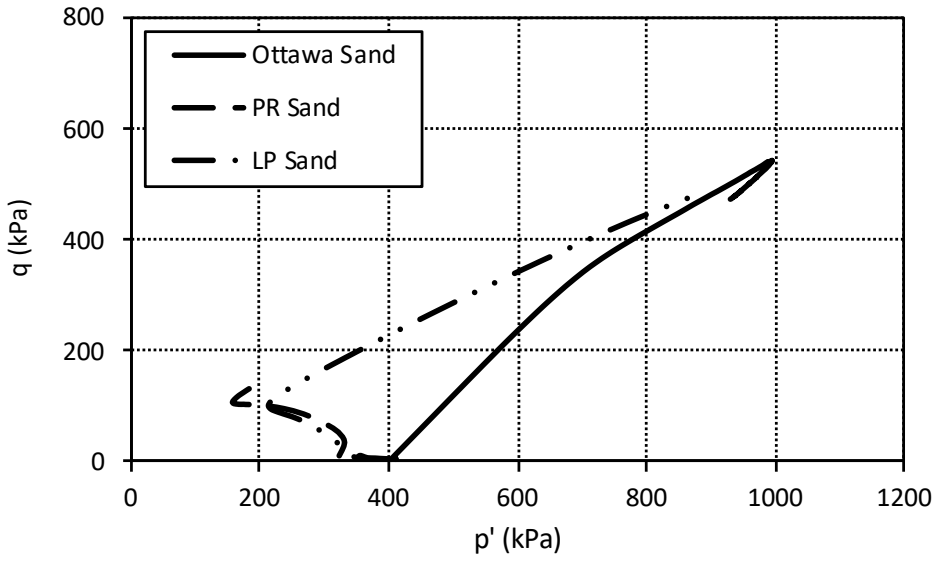

Figure 4.9. Stress Paths of PR Sand, LP Sand, and Ottawa Sand

According to Figure 4.8 and Figure 4.9, the Ottawa sand exhibited an evidently dilative behavior than the other two calcareous sands. The pore pressure of Ottawa sand increased within the first 1% strain and then started to decrease. When the strain was beyond 2%, negative pore pressures were observed. The negative excess pore pressure contributed to a greater value of effective stress ($\sigma' = \sigma - \Delta u$). As a function of effective stress, shear strength increases proportionally as the effective stress increases. Therefore, the maximum shear strength of Ottawa sand was built up rapidly. The contractive behavior of the PR sand and LP sand was attributed to their weak particles, especially for the PR sand with high intraparticle void ratio which resulted in weaker particles and lower shear strength.

The friction angles for three sands are summarized in Table 4.4. Ottawa sand obtained the lowest friction angle due its spherical particle shape. The LP sand had a similar friction angle to the Ottawa sand, because the particles of the LP sand were fine-grained size and rounded to sub-rounded shape. Although the friction angle of the LP sand was closed to that of the Ottawa sand,

the maximum deviator stress of the LP sand was lower than the result of the Ottawa sand slightly. For the PR sand with the highest friction angle, the lowest maximum shear strength was obtained.

Table 4.4. Friction Angles for Puerto Rico Sand, Ledge Point Sand, and Ottawa Sand

Sand Type	PR Sand	LP Sand	Ottawa Sand
Friction Angle (˚)	45.6	33.3	33

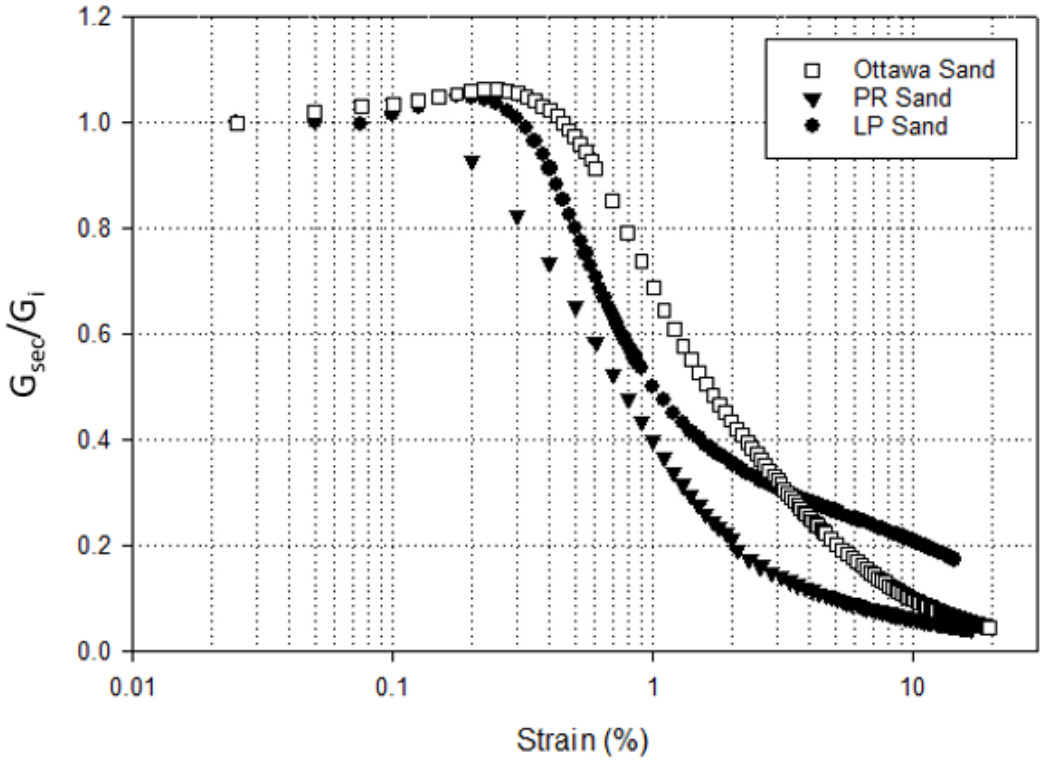

Figure 4.10. Stiffness Degradation of PR Sand, LP Sand, and Ottawa Sand

In terms of the definition and Equation 4.1 mentioned previously, the initial Young's modulus of Ottawa sand was determined based on the initial slope from the stress-strain curve with the value of 92,864 kPa; the corresponding initial stiffness (G_i) was calculated based on Equation 4.4 with the result of 30,955 kPa. The results were summarized in Table 4.5 for

comparison with the other two calcareous sands. Compared to the PR sand and LP sand, Ottawa sand had the highest initial Young's modulus and the highest initial stiffness.

Table 4.5. Initial Young's Modulus and Initial Stiffness of Ottawa Sand, Puerto Rico Sand, and Ledge Point Sand

Sand Type	PR Sand	LP Sand	Ottawa Sand
Initial Young's Modulus (E_i), kPa	37,267	39,783	92,864
Initial Stiffness (G_i), kPa	12,422	13,261	30,955

As discussed before, the stress-strain relationship of soil is non-linear, thus the stiffness is not constant for a given soil. The secant stiffness (G_{sec}) was used to represent this changing parameter as the soil sheared. The stiffness degradation was represented by the ratio of G_{sec}/G_i versus the axial strain in log-scale as shown in Figure 4.10. It is noted that the "threshold" strain was observed for Ottawa sand. After the "threshold" strain, the stress-strain response turned to be non-linear and the stiffness started to reduce. The shape of the stiffness degradation curve of Ottawa sand was more successive, and the stiffness was degraded moderately. The stiffnesses of both PR sand and LP sand were reduced rapidly; however, the stiffness of the LP sand turned to decrease moderately at a smaller strain than that of the PR sand. At the end of the test (15% strain), the Ottawa sand and the PR sand had a similar residual stiffness value close to zero, while a larger strain would be needed for the LP sand to make its stiffness reduce to zero.

Summary

This chapter presented the results of triaxial CU tests on calcareous sands from Puerto Rico and Ledge Point, respectively. Two confining stress levels of 200 kPa and 400 kPa were used to investigate the influence of different confining pressures on the static loading response of calcareous sands. In addition, the triaxial CU tests at a confining pressure of 400 kPa were

performed on the PR sand, the LP sand, and the Ottawa sand. In this case, Ottawa sand was selected as a control group to illustrate how the calcareous sand differs from the silica sand.

The undrained shear strength was influenced by confining pressure. The increasing confining pressure led to an increase in the shear strength and a decrease in the peak friction angle. The LP sand obtained a higher shear strength compared to the PR sand at the same confining pressure. According to the test results, the LP sand exhibited smaller maximum friction angles than those of PR sand due to the finer particle size and the sub-angular particle shape of the LP sand.

The LP sand had a higher initial Young's modulus and initial stiffness compared to the PR sand. The increasing confining pressure led to an increase in the initial Young's modulus and initial stiffness for calcareous sand.

Compared with calcareous sand, silica sand obtained the highest maximum shear strength and the lowest corresponding friction angle at the confining pressure of 400 kPa. Calcareous sand exhibited a ductile behavior when subjected to shearing; thus, the shear strength obtained in this case was the maximum shear strength in the axial strain limit of 20%, rather than the peak shear strength, which required higher axial strain to achieve. Besides, silica sand also had the highest initial Young's modulus and initial stiffness. When subjected to shearing, the stiffness of silica sand degraded slower than that of calcareous sand.

CHAPTER 5. PARTICLE CRUSHING OF CALCAREOUS SANDS

This chapter aims to investigate the crushability of Puerto Rico sand and Ledge Point sand. Three methods are used for crushing the Puerto Rico sand and Ledge Point sand: 1) One dimensional (1-D) consolidation tests on dry sand samples, 2) manually triaxial consolidated drained (CD) tests on dry sand samples, and 3) TruePath triaxial CD tests on saturated sand samples. A comparison of the crushing results of three methods is discussed, such as the effect of different loading mechanisms and the effect of water involved. This chapter ends with presenting the correlation between particle breakage and shear strength based on the results obtained from the TruePath triaxial CD tests.

Evaluating the Breakage Potential of Puerto Rico Snad and Ledge Point Sand

It was reported that the calcareous sands experienced particle damage when subjected to load (Coop, 2003; Zhang et al., 2008; Shahanazari & Rezvani, 2012), due to its high carbonate content and porous particle structures. Particle breakage has been considered as one of the most effective parameters to describe its physical behavior. Three methods were used to evaluate the particle breakage potential of Puerto Rico (PR) sand and Ledge Point (LP) sand: 1) one dimensional (1-D) consolidation tests with dry sand samples, 2) triaxial consolidated drained (CD) tests with dry sand samples, and 3) TruePath triaxial consolidated drained (CD) tests with saturated sand samples. These methods were also performed to investigate the crushing effect wiht different loading mechanisms and different loading conditions: 1) compression loading and shear loading and 2) with and without water. The relative density (D_r) of 50% was used for all three methods. Due to the limitation of the testing devices, conditions of low strain and low stress were used. The strain level of 20% was used to help create more particle breakage instead of the strain level of 15%, which was generally used for shearing tests. Particle breakage results

in a gradation change of soil; hence, particle size distribution was determined before and after each test to establish the particle damage.

The 1-D consolidation tests were performed by pouring the pre-determined amount of dry calcareous sands into the rigid ring with a dimension of 6.35 cm in diameter and 2.54 cm in height. Tamping was necessary to achieve the desired relative density and level the top surface of the specimen with the top of the ring. Two compression stresses of 2,400 kPa and 4,800 kPa were selected for consolidation tests on PR sand and LP sand, respectively. The fixed ring consolidometer used for this test allowed only the top face of the soil sample to move downward relative to the ring.

Triaxial consolidated drained (CD) tests were also performed on dry sand specimens with different confining pressures: 100 kPa, 300 kPa, and 400 kPa. A pre-determined amount of sample was prepared in a dimension of 7.11 cm in diameter and 14.22 cm in height; procedures of sample preparation were the same as the steps of the triaxial CU test described in Chapter 3. The sample was flushed by air after assembled and followed by 15 min isotropic consolidation. The specimen was then sheared to achieve the strain limit of 20% by a shearing rate of 20%/hour.

TruePath triaxial consolidated drained (CD) tests were carried out on the saturated sand samples at confining pressures of 100 kPa, 300 kPa, and 400 kPa. The sample size is the same as the triaxial CD test described above, and the detailed sample preparation and testing procedures have been described in Chapter 3. It is necessary to make sure the sample is fully saturated (>95%). After the 15 min isotropic consolidation, the sample was sheared until 20% strain with a shearing rate of 20% hour.

Crushability of Puerto Rico Sand

Particle size distributions of uncrushed PR sand and the crushed sand obtained from 1-D consolidation (ODC), triaxial CD (TxCD), and TruePath CD (TPCD) tests were presented in Figure 5.1, Figure 5.2, and Figure 5.3. Relative particle breakage (B_r) for each test was determined based on Hardin's method (1985) demonstrated in Chapter 3, and the results were summarized in Table 5.1. The relative particle breakage caused by 1-D consolidation tests with increasing compression stresses were 0.36 and 0.43; the relative breakage contents from triaxial CD tests with increasing confining pressures were 0.46, 0.52, and 0.55, and the results from TruePath CD tests were 0.14, 0.32, and 0.34. The increasing B_r value led to the leftward moving of the particle distribution curve, which represents the grains gradation became finer than the initial gradation. The particle damage of the PR sand occurred throughout its entire particle size range between 4.75 mm and 0.075 mm for all three tests.

Table 5.1. Relative Particle Breakage (B_r) of PR Sand for 1-D Consolidation Test and Triaxial CD Test

Test	ODC		TxCD			TPCD		
Stress (kPa)	2,400	4,800	100	300	400	100	300	400
B_r	0.36	0.43	0.46	0.52	0.55	0.14	0.32	0.34

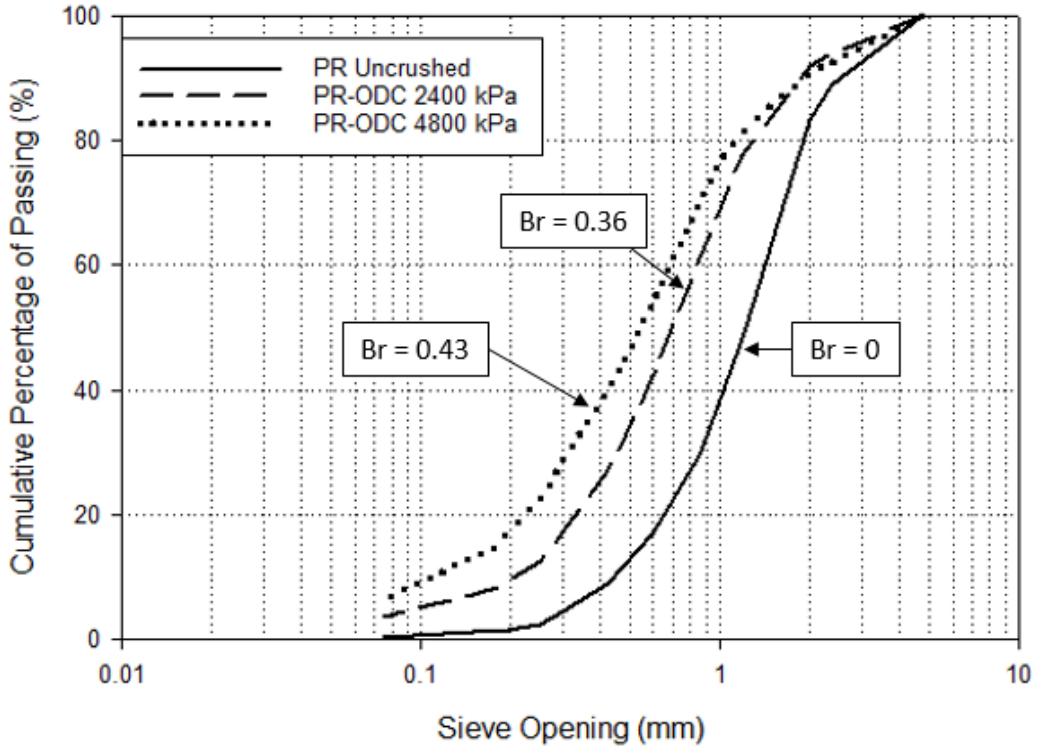

Figure 5.1 Particle Size Distribution of PR Sand (1-D Consolidation Test)

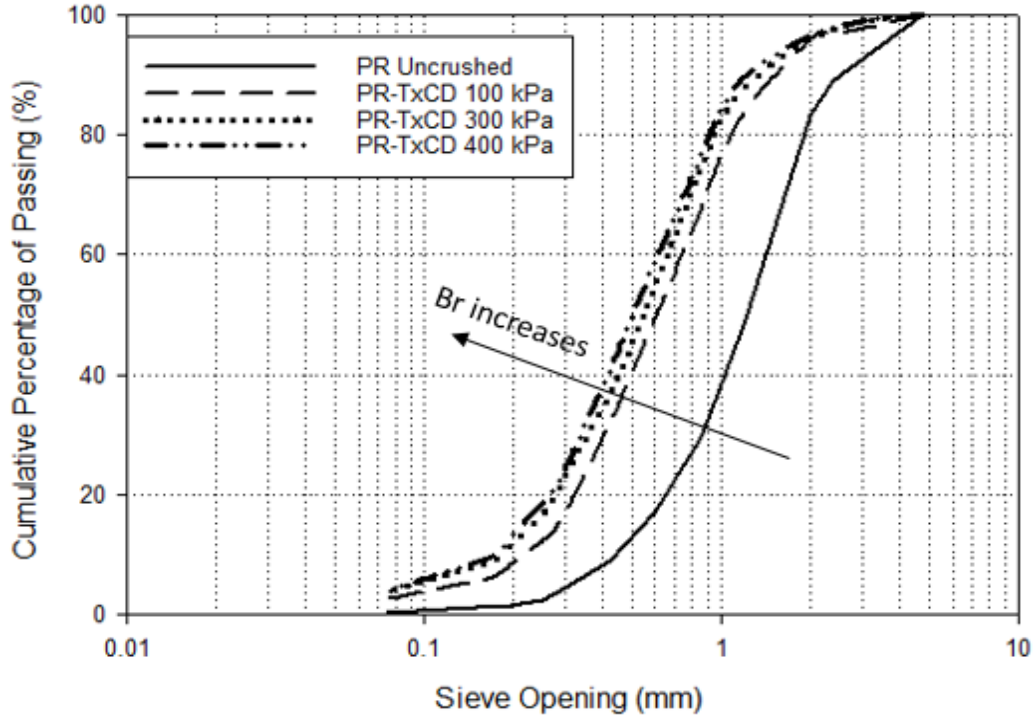

Figure 5.2 Particle Size Distribution of PR Sand (Triaxial CD Test)

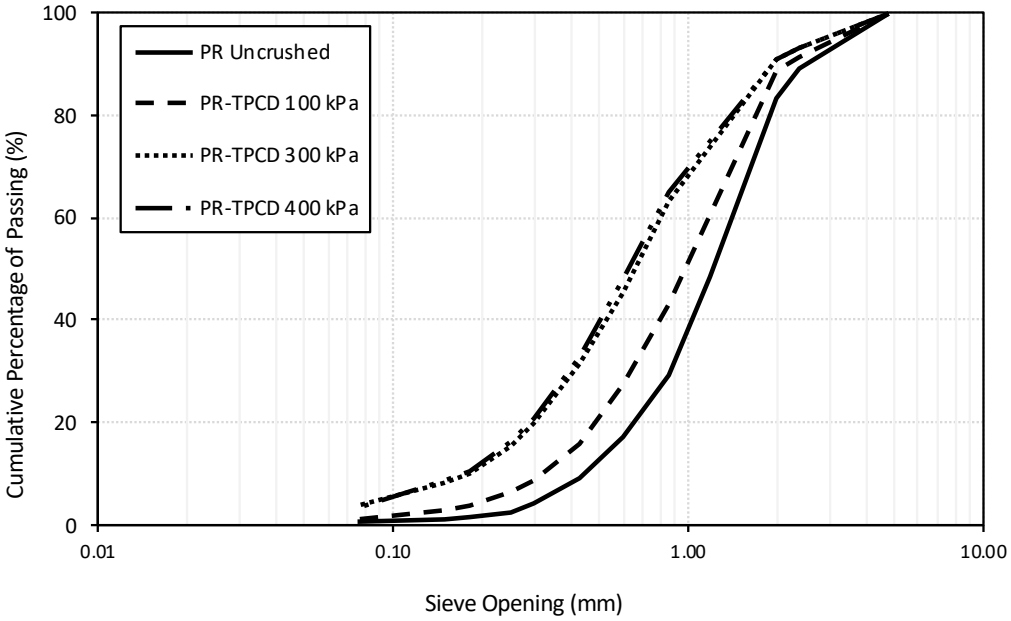

Figure 5.3. Particle Size Distribution of PR Sand (TruePath CD Test)

It was observed that the crushing gradation curves, caused by consolidation, were different from the pattern of those caused by triaxial shearing but were similar to the pattern of those caused by TruePath shearing. The separated particle size fractions were utilized for better understanding. The particle size ranging between 4.75 mm and 0.075 mm can be divided into three fractions: coarse fraction ranging between 5 mm to 1 mm, middle fraction ranging between 1 mm to 0.25 mm, and fine fraction for the particle size smaller than 0.25 mm. The percentage of particle size fractions of uncrushed and crushed samples and the corresponding net increment based on three testing methods were plotted in Figure 5.4, Figure 5.5, and Figure 5.6.

As shown in Figure 5.4, the uncrushed PR sand consisted of a high coarse fraction content of 67.83%, 29.67% of the middle fraction, and a minimal amount of fine fraction of 2.5%. Subjected to a compression load of 2,400 kPa, there was a significant reduction of the coarse fraction, decreasing by approximately 30%, which contributed to a significant increase in middle fraction and a 10% increase in the fine fraction. When the compression stress increased

up to 4,800 kPa, the coarse fraction reduced by 39%, and the crushed specimen obtained a 19% increase of middle fraction and a higher increase of fine fraction (20%) compared to the uncrushed sand.

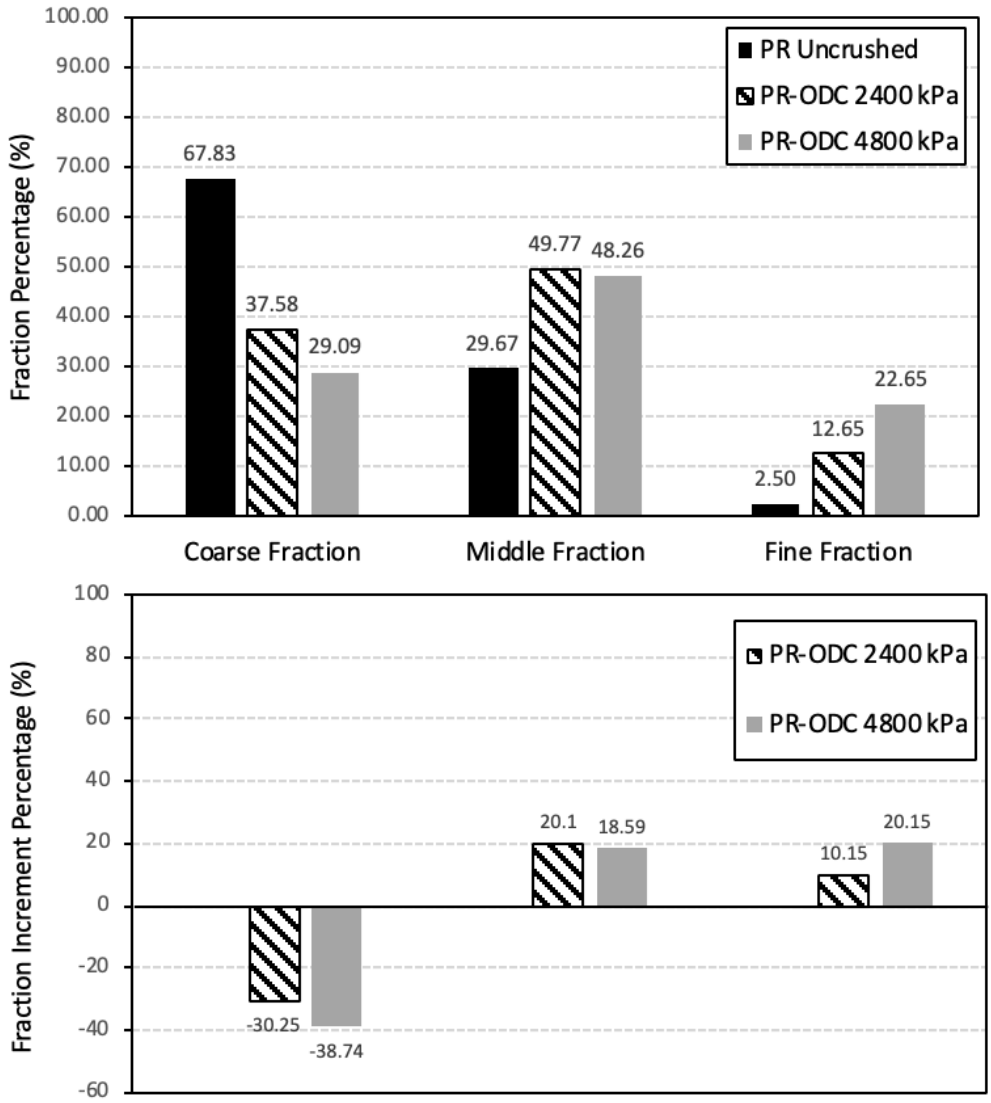

Figure 5.4. Particle Size Fraction Change of Puerto PR (1-D Consolidation Test)

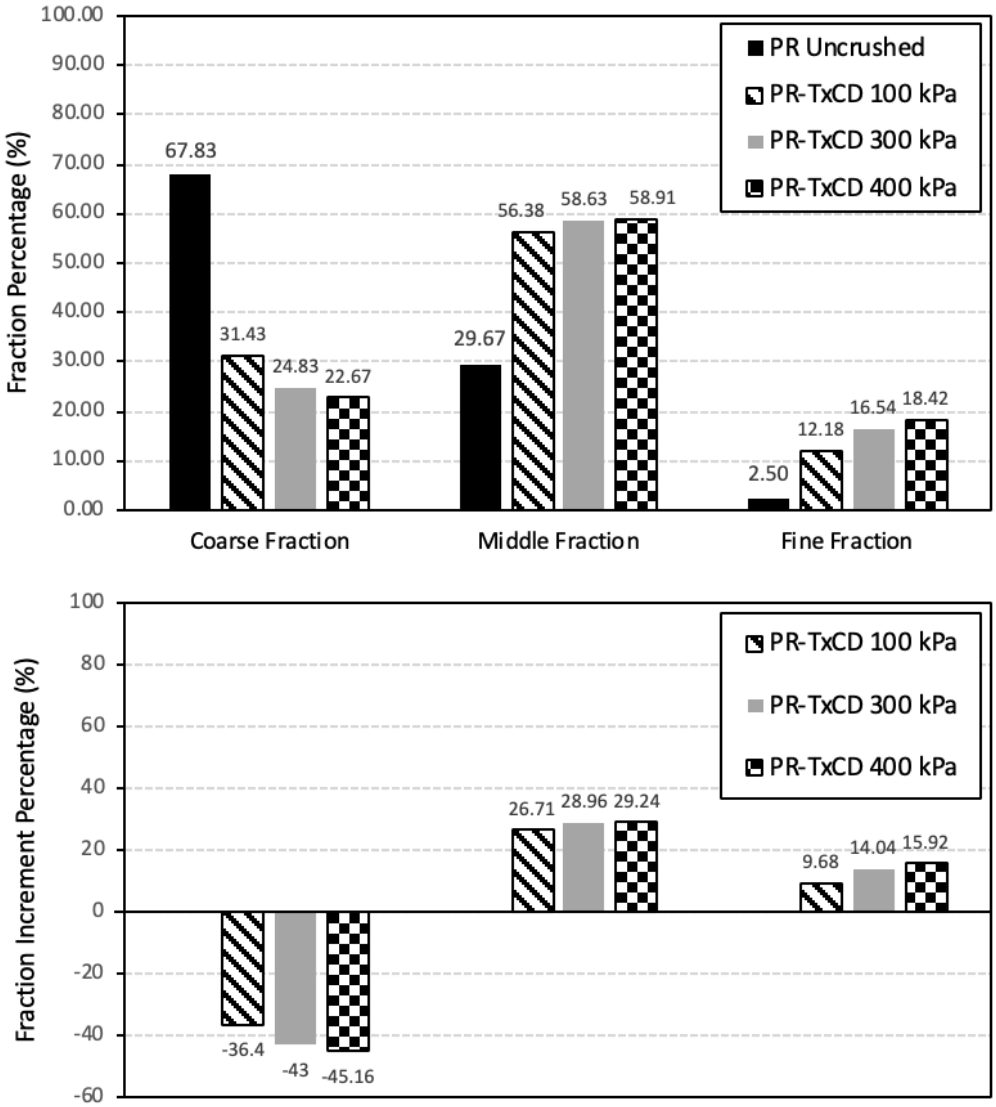

Figure 5.5. Particle Size Fraction Change of PR Sand (Triaxial CD Test)

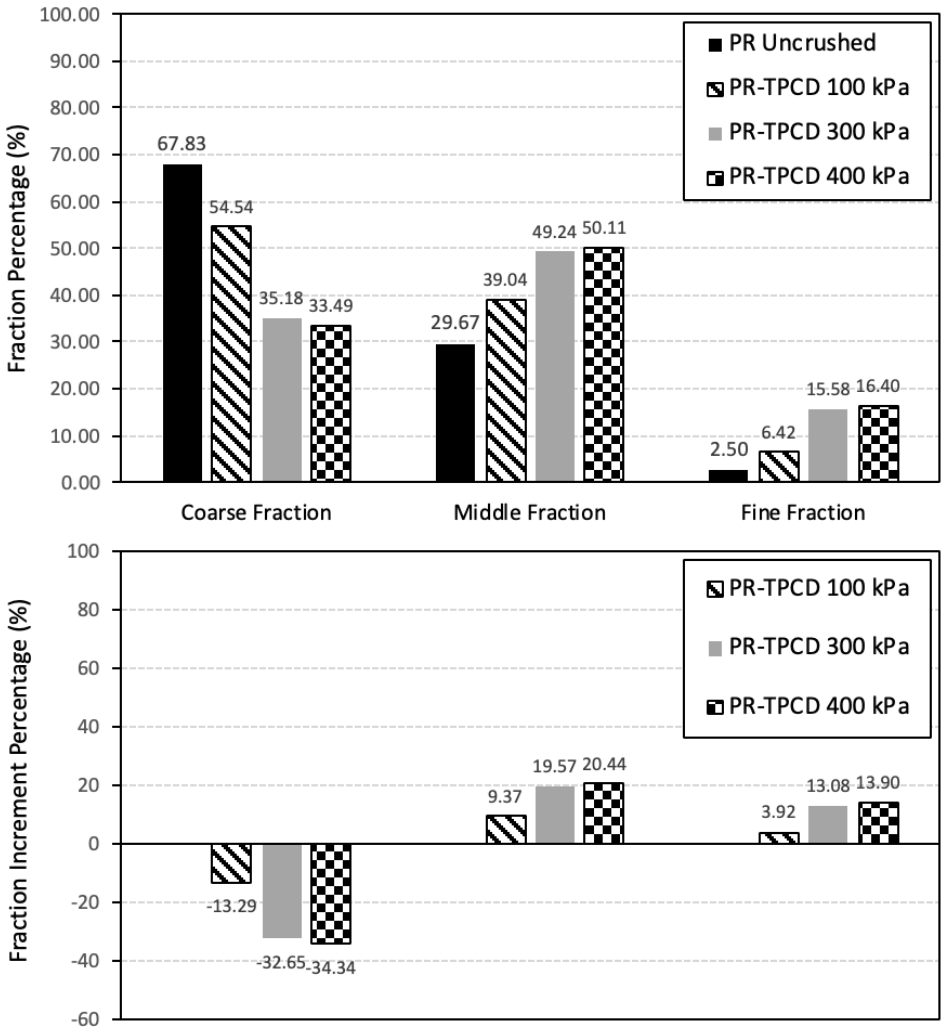

Figure 5.6. Particle Size Fraction Change of PR Sand (TruePath CD Test)

Figure 5.5 shows the results obtained from triaxial CD tests. When the uncrushed sand was sheared at the confining pressure of 100 kPa, a reduction of 36% was obtained for coarse fraction and 27% increase in middle fraction, followed by a 10% increment in the fine fraction. As the confining pressure increased, the coarse fraction kept decreasing, indicating more coarse particles were damaged into the smaller sizes due to the high confining stress.

Figure 5.6 shows the results obtained from TruePath CD tests. Subject to the confining pressure of 100 kPa, the coarse fraction decreased by 13%, the middle increased 9%, and the fine

fraction increased by 4%. As the confining pressure increased, the coarse fraction decreased, resulting in an increase of middle and fine fractions. The net reduction of the coarse fraction caused by the TruePath CD tests was smaller than the results obtained from the Triaxial tests with the same confining pressure.

Higher loading stresses tended to cause more particle breakage from the coarse fraction. The majority of the crushed coarse particles degraded into the middle fraction as loads applied. According to the results of 1-D consolidation tests, the increment of the middle fraction subjected to 4,800 kPa was lower than the increment subjected to 2,400 kPa, which contributed to a further increase in the fine fraction. However, for the other two shearing methods, the increments of the middle and fine fractions both increased as the confining pressure increased. Therefore, the compression loading caused the particle breakage from both coarse and middle fractions resulting in more increase of the fine fraction. In contrast, the shear loading caused the particle breakage from coarse fraction, contributing to the increase of both middle and fine fractions.

As illustrated in Figure 5.7, relative particle breakage (B_r) increased as the loading stress was increasing for all three crushing methods; however, the correlation between relative particle breakage and the loading stress was non-linear. The increments of the particle breakage decreased gradually when the loading stress increased. Additionally, the shear loading resulted in a higher B_r value within a lower stress range, but higher compression stress was required to achieve a similar B_r value. In other words, shear loading was more active on particle crushing and caused more particle breakage than compression loading. On the other hand, compared to the results from the TruePath CD tests, higher B_r values were obtained from the triaxial CD tests

with the same confining stress. Thus, the shear tests performed on dry sand samples led to more particle breakage than the tests on saturated sand samples.

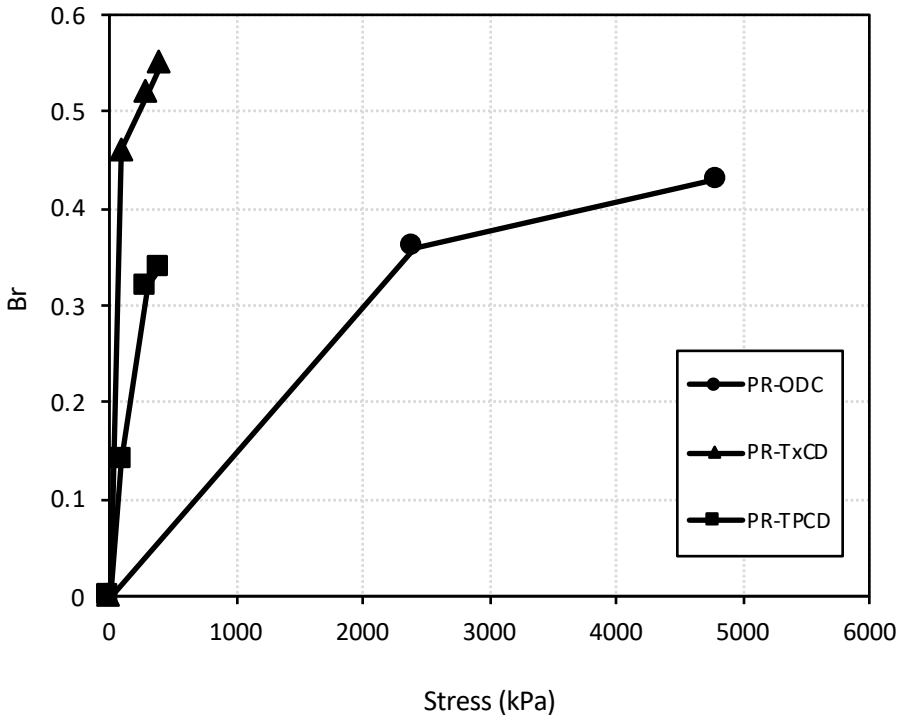

Figure 5.7. Relative Particle Breakage of PR Sand for 1-D Consolidation Tests, Triaxial CD Tests, and TruePath CD Tests

Crushability of Ledge Point Sand

Particle size distributions of uncrushed LP sand and the crushed sand obtained from 1-D consolidation (ODC), triaxial CD (TxCD) tests, and TruePath CD tests were presented in Figure 5.8, Figure 5.9, and Figure 5.10. Relative particle breakage (B_r) for each test was determined based on Hardin's method (1985), and the results were summarized in Table 5.2. The relative particle breakage caused by 1-D consolidation tests with increasing compression stresses were 0.05 and 0.07. The relative breakage contents from triaxial CD tests with increasing confining pressures were 0.02, 0.08, and 0.14; the B_r values obtained from the TruePath CD tests were 0.08, 0.12, and 0.13. For the results of 1-D consolidation tests, the relative particle breakage (B_r)

maintained very close values with increasing compression stresses, which is represented by the overlapping gradation curves in Figure 5.8. The significant gradation change, caused by compression loading, occurred at two particle size ranges: 0.2 mm to 0.6 mm and 0.075 mm to 0.17 mm. As the crushed gradation curves plotted in Figure 5.9 and Figure 5.10, the significant gradation change, caused by shear loading, was observed between the particle size of 0.6 mm and 0.075 mm.

Table 5.2. Relative Particle Breakage (B_r) of LP Sand for 1-D Consolidation Test and Triaxial CD Test

Test	ODC		TxCD			TPCD		
Stress (kPa)	2,400	4,800	100	300	400	100	300	400
B_r	0.05	0.07	0.02	0.08	0.14	0.08	0.128	0.13

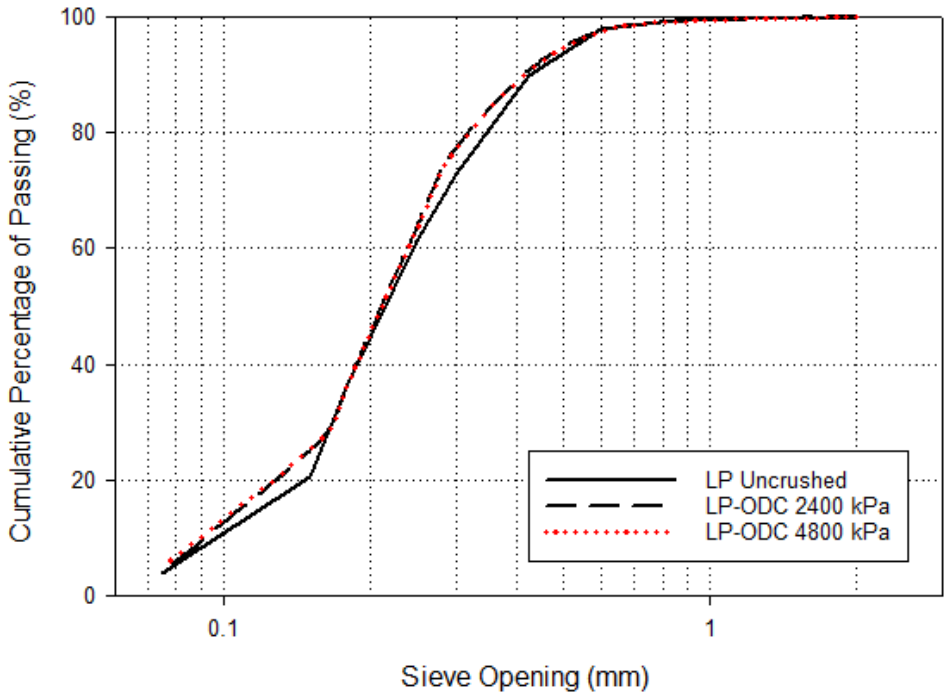

Figure 5.8 Particle Size Distribution of LP Sand (1-D Consolidation Test)

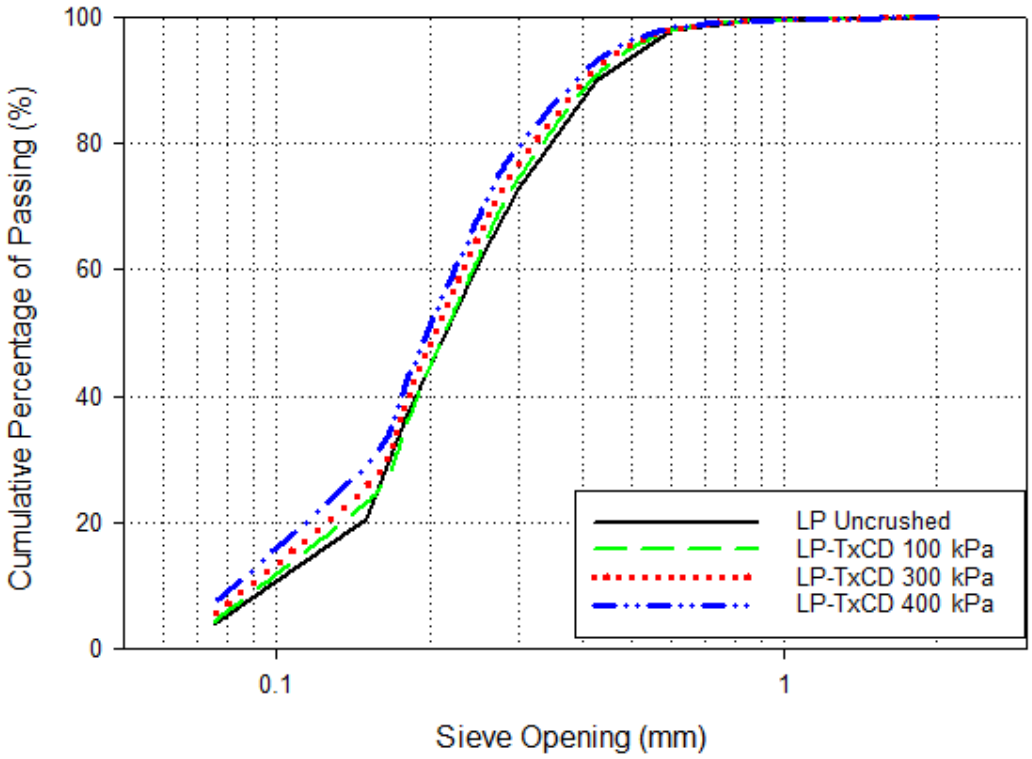

Figure 5.9 Particle Size Distribution of LP Sand (Triaxial CD Test)

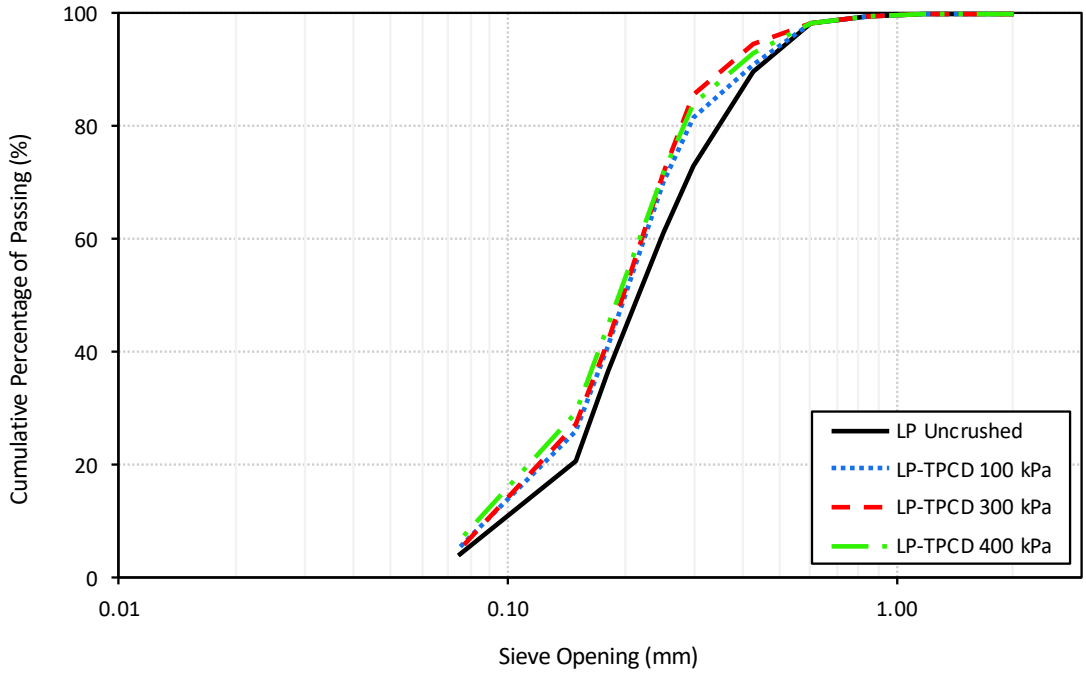

Figure 5.10. Particle Size Distribution of LP Sand (TruePath CD Test)

According to the gradation plots, the compression and shear loading caused the particle breakage in different particle size ranges; thus, the separated particle size fractions were utilized for a better understanding. The particle size of the LP sand ranging between 2 mm and 0.075 mm was divided into three fractions: coarse fraction ranging between 2 mm to 1 mm, middle fraction ranging between 1 mm to 0.25 mm, and fine fraction for the particle size smaller than 0.25 mm. The percentage of particle size fractions of uncrushed and crushed samples and the corresponding net increment based on three testing methods were plotted in Figure 5.11, Figure 5.12, and Figure 5.13.

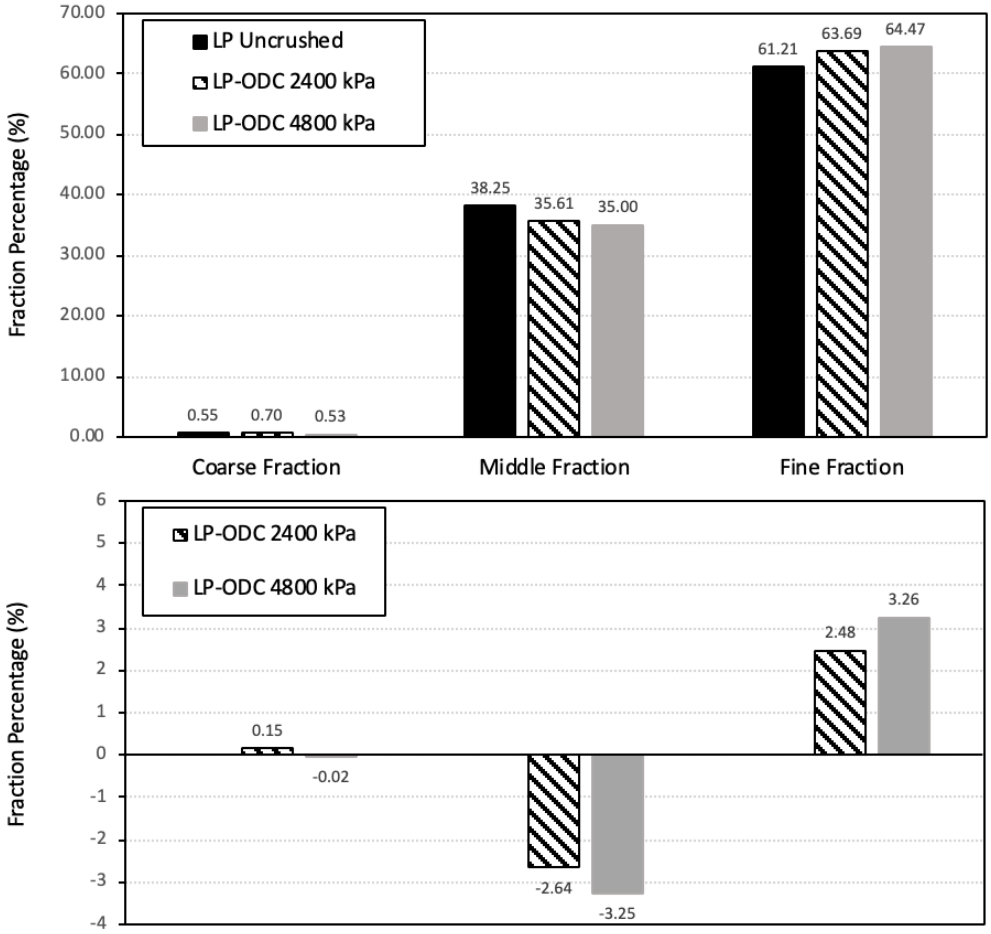

Figure 5.11. Particle Size Fraction Change of LP Sand (1-D Consolidation Test)

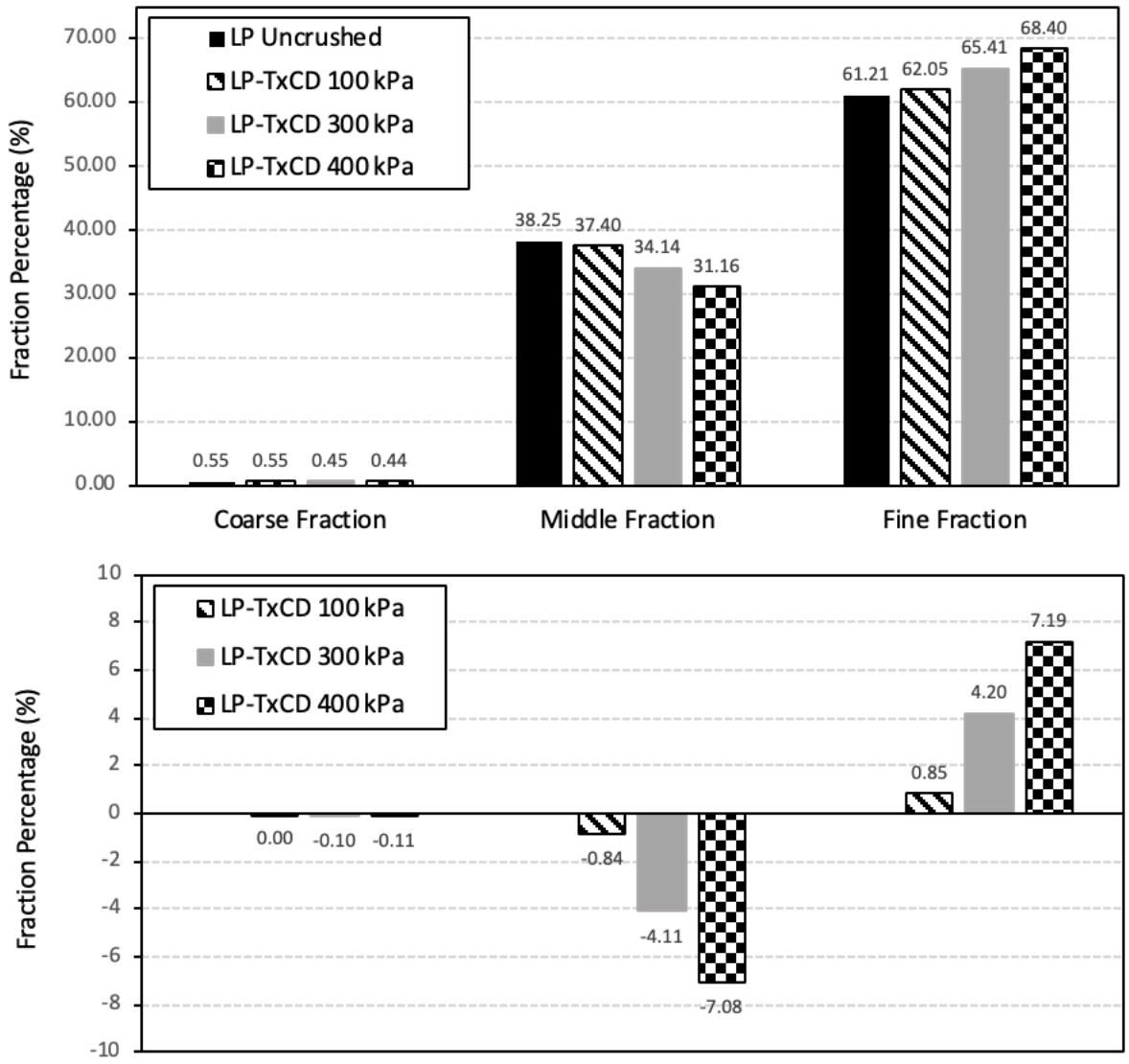

Figure 5.12. Particle Size Fraction Change of LP Sand (Triaxial CD Test)

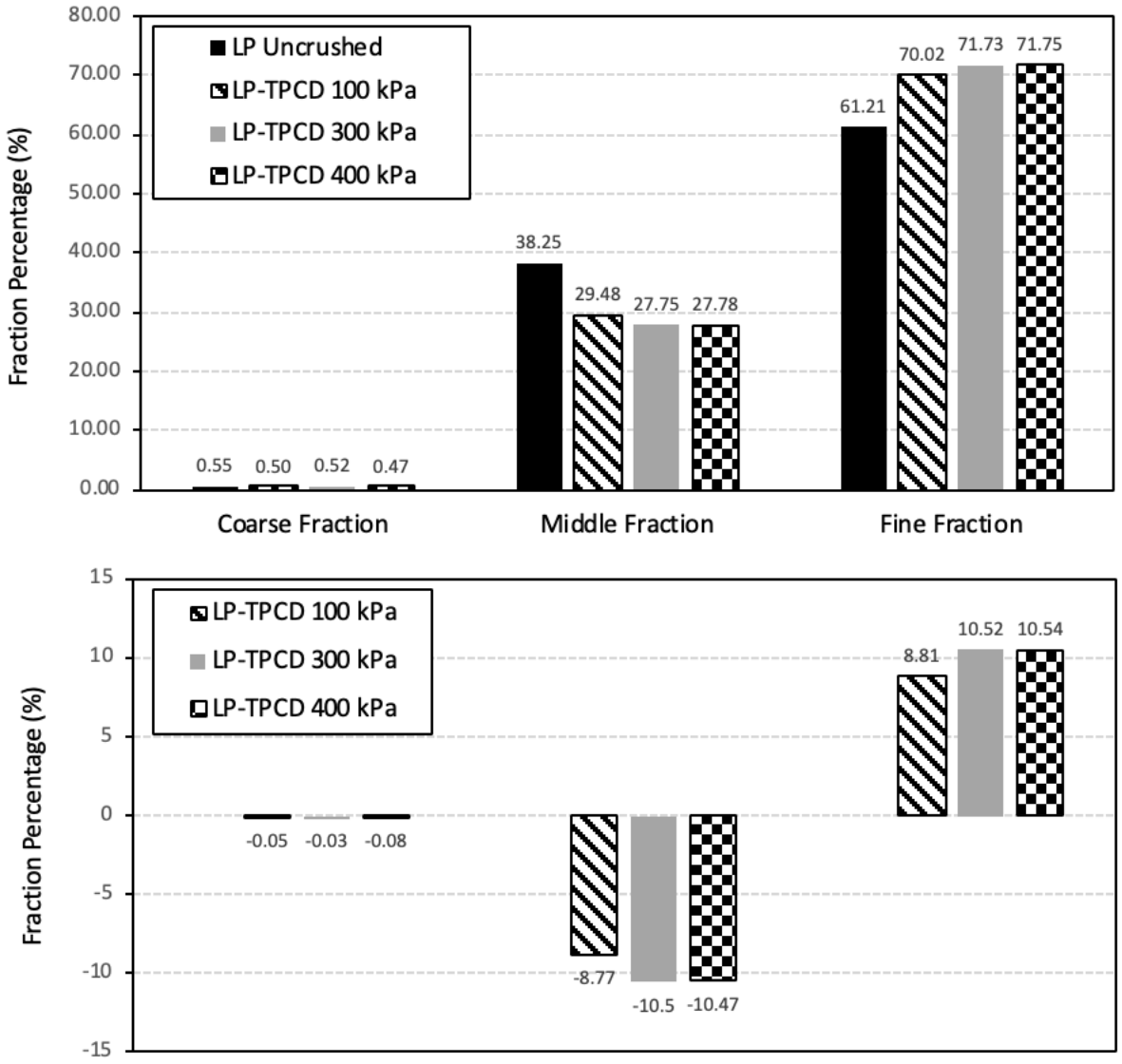

Figure 5.13. Particle Size Fraction Change of LP Sand (TruePath CD Test)

The uncrushed LP sand consisted of a tiny coarse fraction of 0.55%, the middle fraction of 38.25%, and the fine fraction of 61.21%. Since the coarse fraction of LP sand was almost zero, the change in this fraction was ignored. As shown in Figure 5.11, at a compression loading of 2,400 kPa, there was a small decrement in the middle fraction, contributing to a 2.48% increase of fine fraction. When subjected to the compression stress of 4,800 kPa, the fine fraction increased by 3.26% compared to the uncrushed LP sand.

Figure 5.12 shows the results obtained from triaxial CD tests. The middle fraction was decreasing as the confining stress was increasing. Due to the tiny amount of the coarse fraction, particles in the middle fraction were broken into smaller sizes, resulting in the increase of the fine fraction. Although there was a small amount of increase in the fine fraction when subjected to 100 kPa confining stress, the increment of fine fraction increased rapidly when the confining stress increased up to 300 kPa and 400 kPa.

Figure 5.13 shows the particle size fractions and the corresponding net increments of the uncrushed and crushed LP sand obtained after the TruePath CD tests. The particles in the middle fraction were broken into finer sizes. The net increments of the fine fraction caused by the TruePath CD tests increased moderately and were smaller than the results from triaxial CD tests.

For the LP sand, higher loading stresses tended to cause more particle breakage from the middle fraction. According to the results of 1-D consolidation tests, the increased amount of fine fraction was quite small compared to the results of the other two methods. The increments of the fine fraction caused by compression loading mainly focused on the particle size ranging between 0.2 mm to 0.6 mm and 0.075 mm to 0.17 mm; however, the increment of the fine fraction caused by shear loading focused on a broader size range (0.6 mm to 0.075 mm).

Figure 5.14 indicates the correlation of the relative particle breakage (B_r) along with the increasing loading stress. As the loading stress increased, the relative particle breakage increased non-linearly. The compression loading caused less particle breakage with large loading stresses, while more crushing contents were obtained by shear loading with relatively lower loading stresses. Therefore, similar to the conclusion of PR sand, shear loading is more active to cause more particle breakage. On the other hand, the results of B_r based on saturated sand samples

were slightly lower than the B_r values obtained from dry sand samples. Thus, the presence of the water has a negative influence on particle breakage.

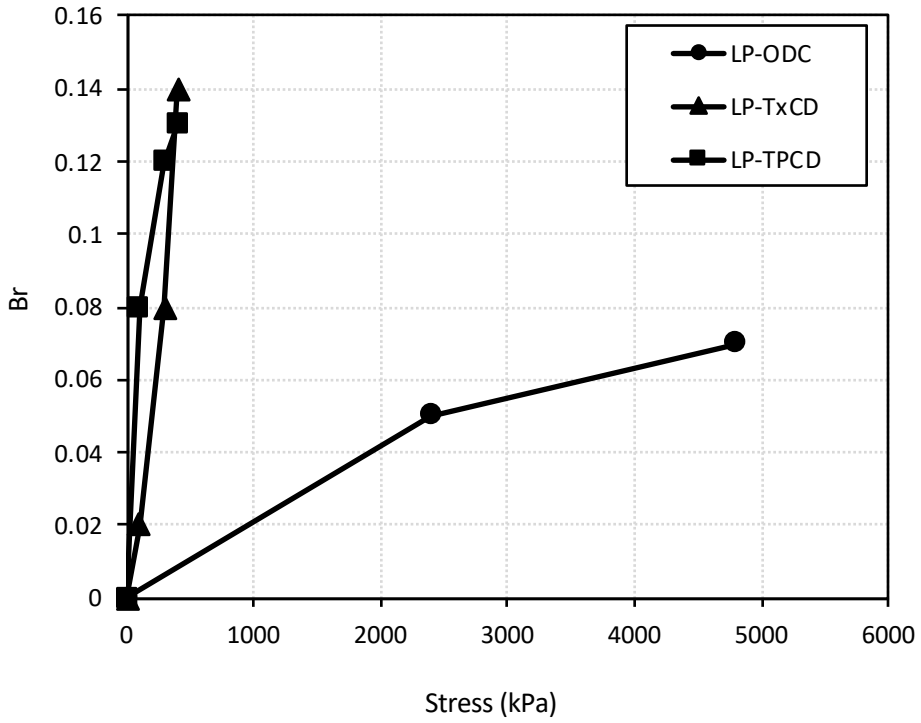

Figure 5.14. Relative Particle Breakage of LP Sand for 1-D Consolidation Tests, Triaxial CD Tests, and TruePath CD Tests

According to the results of PR sand and LP sand, particle breakage depended not only on the magnitude of loading stress but also on the particle size distribution and the loading mechanism. The PR sand had more particle breakage than the LP sand with the same relative density and the same loading stress because the PR sand had the coarser grains than the LP sand. Thus, the PR sand exhibited a higher crushability. On the other hand, the shear loading was a more active loading mechanism causing more particle breakage. A higher B_r value was achieved by shear loading with low confining stress, while approximately 10-times higher stress of compression loading was required to obtain the same B_r value. Additionally, dry sand samples tended to have more particle breakage than saturated samples at the same pressure.

Particle Breakage and Shear Strength

The stress-dilatancy model was suggested by Rowe (1962), illustrating the correlation between the effective stress ratio and the friction angle (Equation 5.1). Ueng and Chen (2000) modified the stress-dilatancy model in triaxial tests taking account of the particle breakage for crushable soils. The modified model was shown in Equation 5.2:

$$\frac{\sigma_1'}{\sigma_3'} = (1 - \frac{d\varepsilon_v}{d\varepsilon_1})tan^2\left(45^\circ + \frac{\emptyset_u}{2}\right) \quad (5.1)$$

$$\frac{\sigma_1'}{\sigma_3'} = (1 - \frac{d\varepsilon_v}{d\varepsilon_1})tan^2\left(45^\circ + \frac{\emptyset_f}{2}\right) + \frac{dE_B}{\sigma_3' d\varepsilon_1}(1 + sin\emptyset_f) \quad (5.2)$$

in which, σ_1' is the maximum effective principal stress; σ_3' is the minimum effective principal stress; $d\varepsilon_v$ is the volumetric strain increment (contraction is positive); $d\varepsilon_1$ represents the axial strain increment; $\emptyset_u$ and $\emptyset_f$ are the friction angle of soil; and dE_B is the energy consumed for particle crushing. The first term of this equation represents the dilatancy during shearing, and the second term of the equation corresponds to particle crushing. Zhang et al. (2009) suggested to represent dE_B by the term of kdS_v, where dS_v is the specific surface area increment, k is a coefficient depending on soil particle strength. Thus, Equation 5.2can be derived as following:

$$\frac{\sigma_1'}{\sigma_3'} = (1 - \frac{d\varepsilon_v}{d\varepsilon_1})tan^2\left(45^\circ + \frac{\emptyset_u}{2}\right) + \frac{kdS_v}{\sigma_3' d\varepsilon_1}(1 + sin\emptyset_u) \quad (5.3)$$

To evaluate the modified stress-dilatancy model, the specific surface area increment needs to be determined. Miura and Yamanouchi (1971) proposed a method to calculate the surface area of soil by using the gradation curve of soil. The results from triaxial CD tests for Puerto Rico sand and Ledge Point sand were taken for this investigation. For particles larger than 0.075 mm, the surface area can be determined as:

$$S_{w1} = \sum F * \frac{[4\pi(\frac{d_m}{2})^2]}{[(\frac{4}{3})\pi(\frac{d_m}{2})^3 G_s \gamma_w]} \quad (5.4)$$

where, d_m represents the mean diameter of adjacent sieves calculated by $\sqrt{d_1 d_2}$; d_1 and d_2 are the sizes of two consecutive sieve (e.g. 0.3 mm and 0.25 mm); F is the percentage retained on sieve by weight; G_s is the specific gravity of the soil; γ_w is the unit weight of water.

For particles smaller than 0.075 mm, the surface area can be calculated by Blaine method as shown in Equation 5.5:

$$S_{w2} = \sum F * \frac{S_0 * G_c * t * (1-e_0) * \sqrt{e^3}}{G_s * t_0 * (1-e) * \sqrt{e^3}} \quad (5.5)$$

where, G_c is the specific gravity of fine grains; S_0 is the specific surface; t_0 is the sedimentation time; e_0 is the void ratio of fine-grain powder; e and t are the values related to G_s. Then, the total specific surface area can be obtained by Equation 5.6, and the total surface area is determined by using the total specific surface area multiply by the soil dry unit weight (Equation 5.7).

$$S_w = S_{w1} + S_{w2} \quad (5.6)$$

$$S = S_w * \gamma_d \quad (5.7)$$

For irregular-shape particles, the calculated surface area would be lower than the actual surface area. The negative effect can be neglected when considering the surface area increment (Zhang et al. 2009).

The data obtained by the TruePath CD tests from Chapter 4 were used in this section because the TruePath system can automatically record the volumetric change of a saturated sample by collecting the water increased or decreased in the internal load cell during the tests. The effective stress ratio and the volumetric change along with the axial strain for PR sand and LP sand were plotted in Figure 5.15, Figure 5.16, Figure 5.17, and Figure 5.18. The positive volumetric change represents the sample dilation during the test, and the negative value represents the sample contraction.

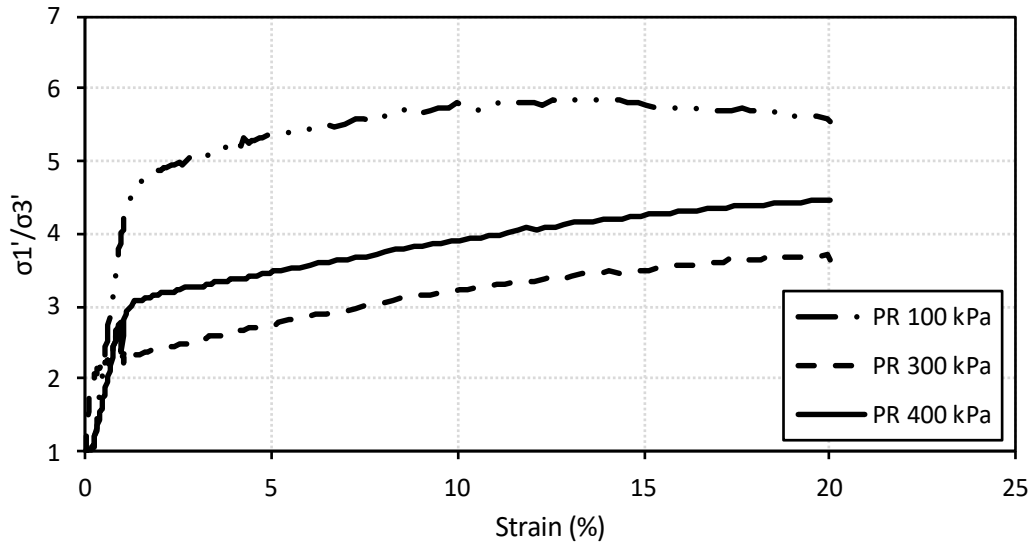

Figure 5.15. Effective Stress Ratio of PR Sand

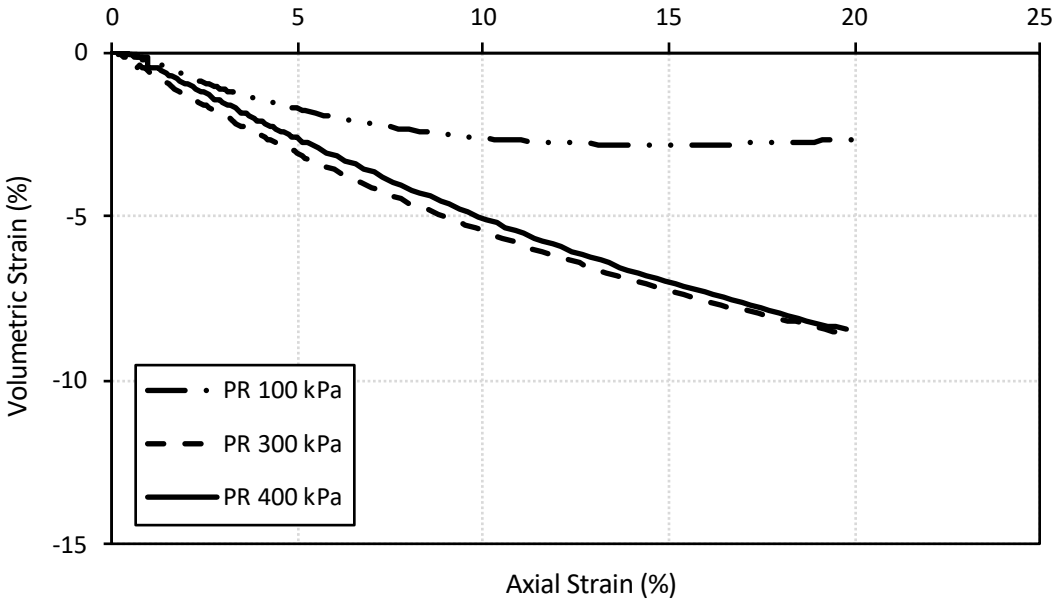

Figure 5.16. Volumetric Change of PR Sand

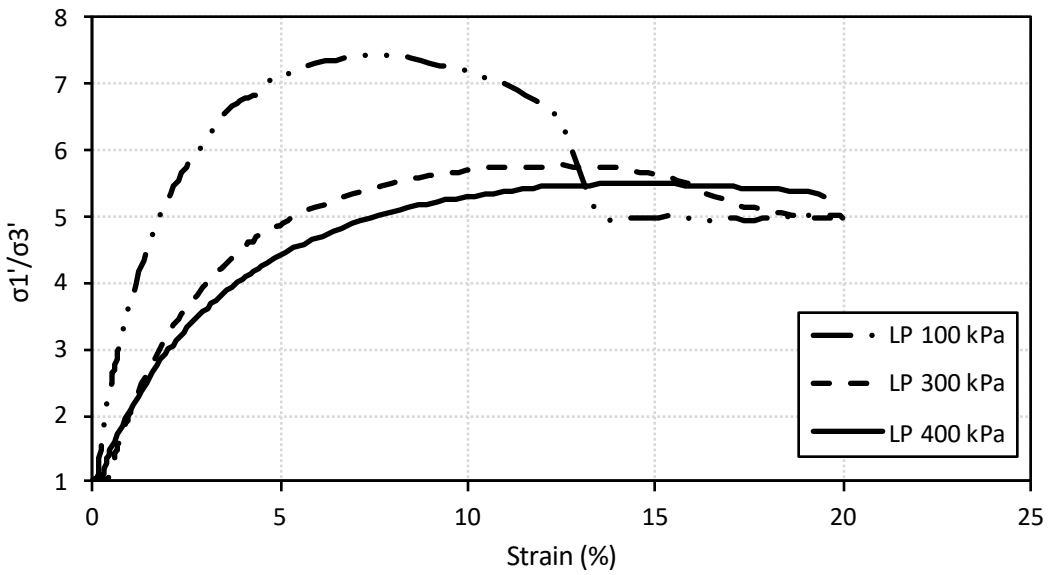

Figure 5.17. Effective Stress Ratio of LP Sand

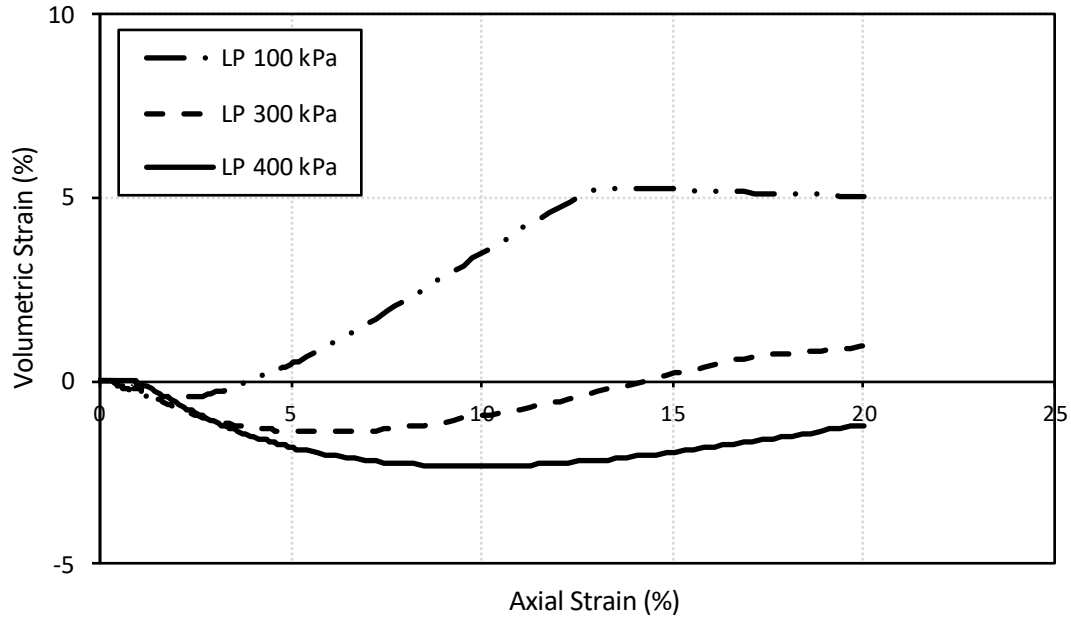

Figure 5.18. Volumetric Change of LP Sand

All the PR sand samples contracted when subjected to shear at the confining pressures of 100 kPa, 300 kPa, and 400 kPa with the negative volumetric strain in the maximum strain limit

of 20%. The LP sand sample at confining pressure of 100 kPa exhibited an evident dilation. At the confining pressure of 300 kPa, the volumetric strain decreased by a tiny amount of 1.4%, and then the sample turned to dilate after 14% strain with a positive increment of 0.9% at 20% strain limit. For the LP sample at 400 kPa, the negative values of volumetric strain within the axial strain limit indicated the sample contraction.

The total specific surface area increments of the PR sand and LP sand were calculated based on equations mentioned in the previous paragraphs and were plotted along with the axial strain for each confining pressure (Figure 5.1 and Figure 5.20). As the plots shown, the surface area increment was increasing along with the axial strain and confining pressure for both calcareous sands. The slope of the curve is the value for $\frac{dS_v}{d\varepsilon_1}$ in Equation 5.3.

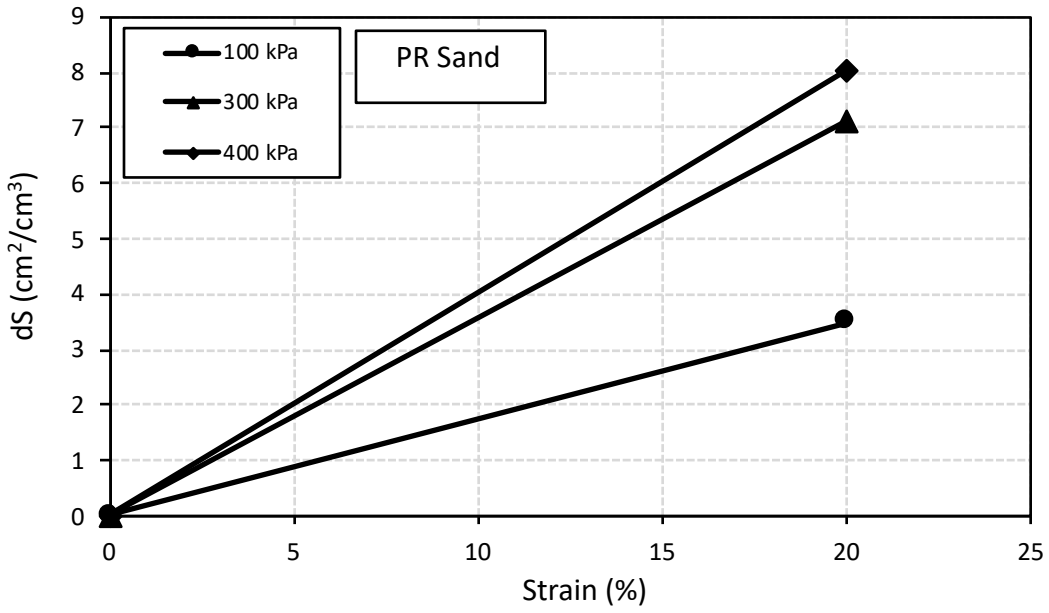

Figure 5.19. Correlation between Surface Area Increment and Axial Strain of PR Sand

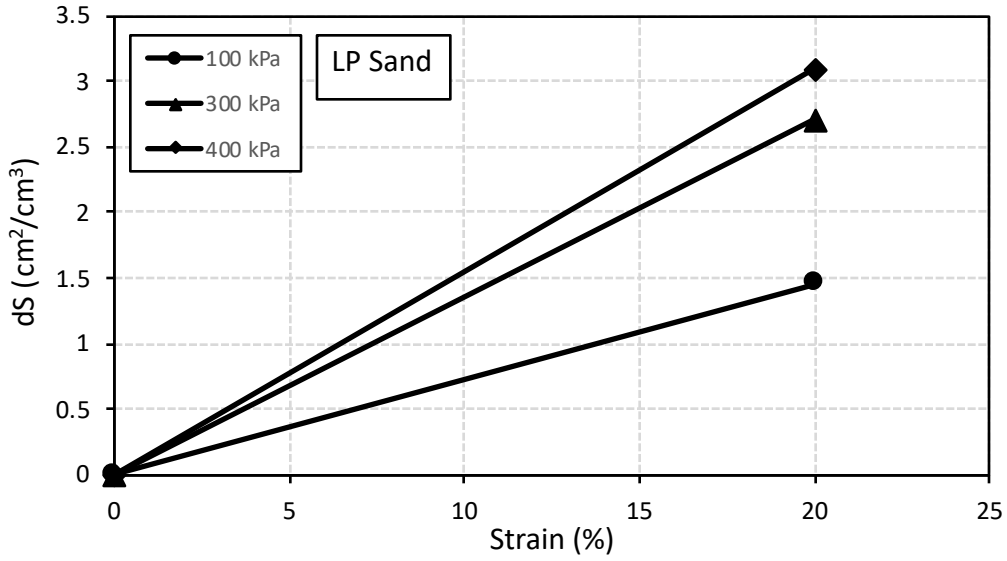

Figure 5.20. Correlation between Surface Area Increment and Axial Strain of LP Sand

The parameter $\emptyset_u$ in Rowe's model in Equation 5.1 is the friction angle excluded the component of dilatancy but included the component of particle breakage. In the modified Rowe's model in Equation 5.2, $\emptyset_f$ is the friction angle without the component of dilatancy and particle breakage, which is the primary friction angle between the sand particles. In the present study, only approximately value of $\emptyset_f$ can be calculated.

The friction angle, $\emptyset_u$, with the component of particle breakage is related to the ratio of total specific area increment to the strain increment (i.e. $\frac{dS_v}{d\varepsilon_1}$) (Zhang et al., 2009). The value of $\emptyset_u$ was calculated by Equation 5.1, and the correlations between $\emptyset_u$ and $\frac{dS_v}{d\varepsilon_1}$ for PR sand and LP sand were shown in Figure 5.21 and Figure 5.22. At the point of $\frac{dS_v}{d\varepsilon_1} = 0$, the corresponding value of $\emptyset_u$ is the friction angle excluded the component of particle breakage (i.e. $\emptyset_u = \emptyset_f$ when $\frac{dS_v}{d\varepsilon_1} = 0$). A linear trend line was used to find the intercept in this case, and the values of $\emptyset_f$ for PR sand and LP sand were 49.5° and 41.5°, respectively.

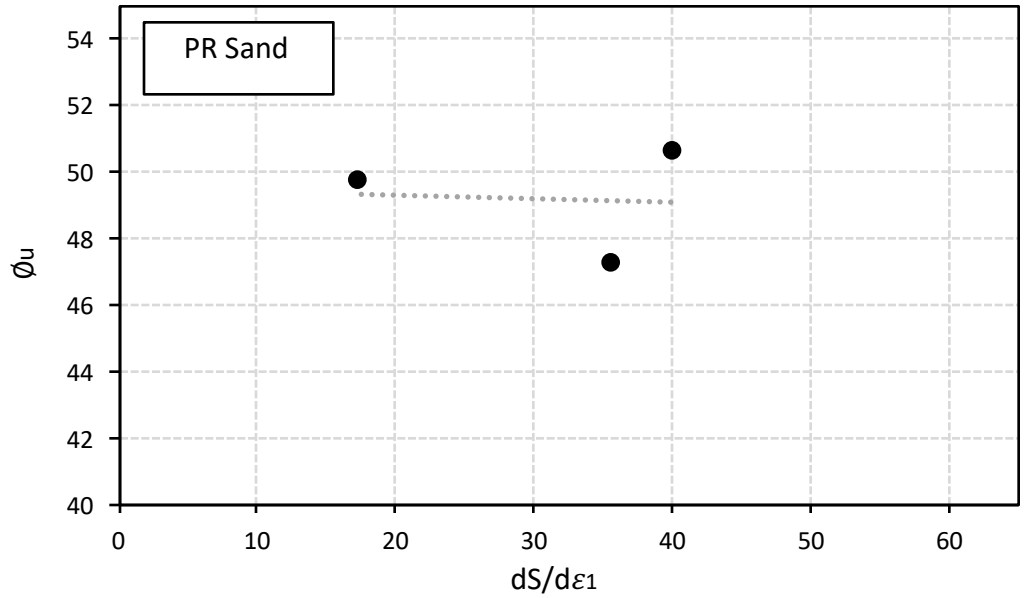

Figure 5.21. Correlation between $\emptyset_u$ and $\frac{dS_v}{d\varepsilon_1}$ for PR Sand

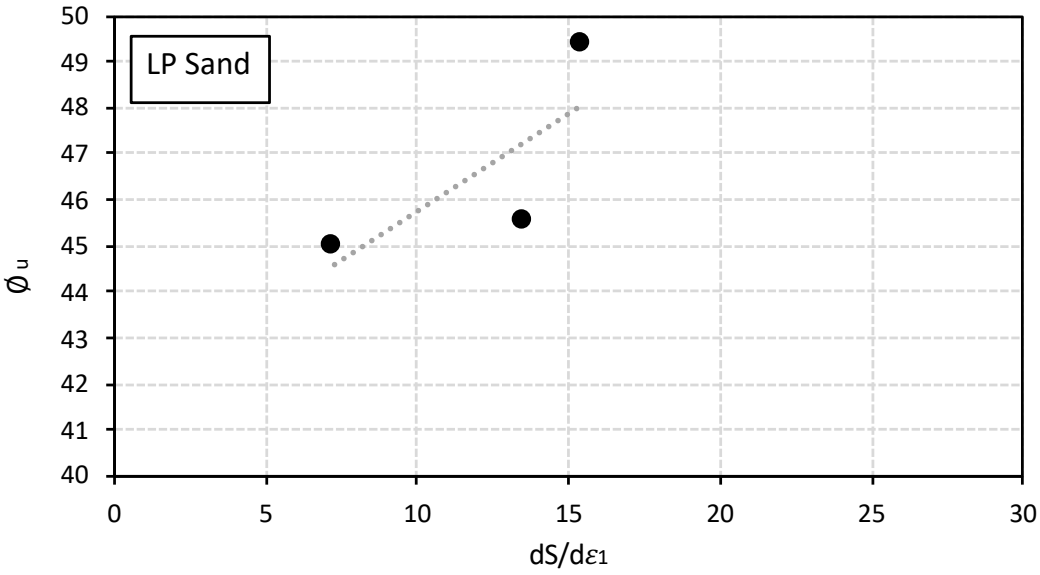

Figure 5.22. Correlation between $\emptyset_u$ and $\frac{dS_v}{d\varepsilon_1}$ for LP Sand

A parameter, $\emptyset_b$, is a difference between $\emptyset_u$ and $\emptyset_f$, representing the crushing intensity of particles. In addition, the friction angle corresponding to the maximum shear strength was

calculated and was marked as the symbol of $\emptyset$, which included the both components of dilation and particle breakage. Thus, a difference ($\emptyset_v$) between $\emptyset$ and $\emptyset_u$ represented the dilative intensity of samples. The positive value of the dilative intensity indicated sample dilation, and the negative value indicated the contraction. The calculated results for PR sand and LP sand were summarized in Table 5.3 and Table 5.4, respectively.

Table 5.3. Summary of the Dilation and Particle Breakage Intensities for PR Sand

Confining Pressure (kPa) (PR Sand)	$\frac{\sigma_1'}{\sigma_3'}$	$\emptyset$ (°)	$\emptyset_u$ (°)	$\emptyset_f$ (°)	$\emptyset_b$ (°)	$\emptyset_v$ (°)
100	5.85	44.8	49.7	49.5	0.2	-4.9
300	3.7	35.0	47.2		-2.3	-12.2
400	4.67	39.4	50.6		1.1	-11.2

Table 5.4. Summary of the Dilation and Particle Breakage Intensities for LP Sand

Confining Pressure (kPa) (LP Sand)	$\frac{\sigma_1'}{\sigma_3'}$	$\emptyset$ (°)	$\emptyset_u$ (°)	$\emptyset_f$ (°)	$\emptyset_b$ (°)	$\emptyset_v$ (°)
100	7.43	49.7	45.0	41.5	3.5	4.7
300	5.77	44.7	45.5		4.0	-0.8
400	5.5	43.8	49.5		8.0	-5.7

Based on the results listed in Table 5.3 and Table 5.4, both dilative and crushing intensities were influenced by the confining pressure. As the confining pressure increased, the dilative intensity decreased, while the crushing intensity increased. For example, the dilative and crushing intensities of the LP sand were 4.7° and 3.5° at 100 kPa, and then the dilative intensity decreased to -5.7° with the corresponding crushing intensity of 8.0° at 400 kPa.

For the PR sand, the dilative intensities were lower than the crushing intensities at 100 kPa, 300 kPa, and 400 kPa. In this case, particle breakage was the control factor contributing to the shear strength, and the sample contraction occurred which was consistent with the testing

results. It was observed that the maximum friction angles (∅) in Table 5.3 were lower than the primary friction angle ($\emptyset_f$). This phenomenon was attributed to the degradation of the particle size distribution due to the particle breakage caused by shear loading, resulting in a decrease of friction angle. On the other hand, in the present study, the maximum friction angle was calculated based on the maximum shear strength in a strain limit of 20%, rather than the peak shear strength, which required a higher strain limit. Therefore, the maximum friction angle obtained in this case was not the peak friction angle, which led to a lower value than the primary friction angle.

For the LP sand, the dilative intensity was higher than the crushing intensity at 100 kPa; therefore, the sample dilation had a more considerable influence on the shear strength. At 300 kPa, the dilative intensity approximately equaled to zero, which indicated a decline of dilatancy. As the confining stress increased, the dilative intensity decreased, and the sample contraction occurred which was consistent with the testing results. Therefore, the effect of particle breakage turned out to be significant at 400 kPa.

Summary

In this chapter, three testing methods with various loading stresses were performed on PR sand and LP sand: 1) One dimensional (1-D) consolidation tests on dry sands, triaxial consolidated drained (CD) tests on dry sands, and TruePath CD tests on saturated sands. Different particle crushing contents of PR sand and LP sand were obtained from the three testing methods. Additionally, the effects of the loading mechanism and the presence of water on particle breakage were discussed. All the tests were performed on medium-dense specimens (D_r = 50%), and Hardin's method was utilized to determine the relative particle breakage. At the end

of this chapter, the modified Rowe's model was introduced to investigate the correlation between dilatancy and particle breakage based on the results from the TruePath tests.

According to the results, higher loading stress caused more particle breakage on calcareous sands, and the initial particle size distributions of the calcareous sands determined their crushing potential. At the same stress level, PR sand with coarser grains had more crushing content than the fine-grained LP sand. Also, shear loading generated more crushing content than the compression loading, and lower stress was required for shearing than that of compression to achieve the same amount of crushing. For PR sand, the majority of crushed contents caused by compression loading were in the fine particle fraction, and the crushed contents caused by shear loading were in both middle and fine fraction. For LP sand, the crushed particles caused by compression loading distributed in two narrow size ranges. In contrast, the shear loading crushed the particles distributing in one continued and broader size range. Therefore, shear loading had a more active effect than the compression loading on particle breakage.

A modified Rowe's model was introduced to illustrate the correlation between dilatancy and particle breakage based on the results from the TruePath CD tests performed on the saturated calcareous sands. The calculated maximum friction angle included the components of dilation and particle breakage. Modified Rowe's model took account of the particle breakage for crushable soils. Therefore, the maximum friction angle was divided into three components: the primary friction angle, the angle of crushing, and the angle of dilation. The angles of crushing and dilation indicated the crushing and dilation intensities during the tests.

Both dilative and crushing intensities were influenced by confining pressure. As the confining pressure increased, the dilative intensity decreased, while the crushing intensity increased. The particle breakage was the control factor contributing to the shear strength for PR

sand due to its high crushability; however, the dilation exhibited a significant influence on the shear strength at a low-stress level for LP sand with low crushability. Then, the effect of particle breakage turned out to be more significant than that of dilation as the loading stress increased.

CHAPTER 6. EFFECT ON STATIC BEHAVIOR WITH INCREASING PARTICLE BREAKAGE CONTENT

Three methods were used for crushing the PR sand and LP sand in Chapter 5. Since the crushing contents obtained from the triaxial CD tests on saturated sands were similar to those of the TruePath CD tests, the results from the triaxial CD tests with dry sand and the 1-D consolidation tests were selected for further study in this chapter. Different crushing contents, created by the two methods of the triaxial CD tests with dry sands and the 1-D consolidation tests, are put together for each type of the calcareous sand to investigate the effect of increasing particle breakage content on the static behavior. A series of reconstituted specimens were prepared based on the crushed particle size distributions obtained in Chapter 5. Triaxial consolidated undrained (CU) tests were carried out on the reconstituted samples with 400 kPa confining pressure. The correlation of loading response, stiffness degradation, and dilative behavior with increasing particle breakage are discussed in this chapter.

Monotonic Behavior of Crushed Puerto Rico Sand

Reconstituted PR sand samples with relative particle breakage contents of 0.36, 0.43, 0.46, 0.52, and 0.55 were prepared for triaxial CU tests with a relative density of 50% to investigate the static behavior with increasing particle breakage. The dry sand sample was in a dimension of 7.11 cm diameter and 14.22 cm height and flushed with CO_2 gas followed by flushing de-aired water to achieve above 95% of saturation. The sample was consolidated at 200 kPa isotropic pressure for 15 min, and then sheared at a confining pressure of 400 kPa until 15% axial strain. The shearing rate was 1%/hour.

The stress-strain curves for the PR sand with increasing particle breakage were plotted in Figure 6.1. A zero value of relative particle breakage (B_r) represented the uncrushed sample, which obtained the lowest shear strength. The stress-strain curve of $B_r = 0.43$ was quite closed to

but slightly higher than the curve of $B_r = 0.46$ before 4% strain and had an overlapping beyond this strain level. Small amount of shear strength increment was obtained for the particle breakage increasing from 0 to 0.46; whereas, significant improvements on shear strength were observed on sample with $B_r = 0.52$ and 0.55. Especially for the case of $B_r = 0.55$, the peak strength was achieved at approximately 1200 kPa followed by a slight strain softening after peak. For medium dense Puerto Rico sand subjected to a constant confining pressure, the increasing particle breakage led to an increase of shear strength.

On the other hand, samples with low particle breakage tended to show more ductile behavior, where peak strength achieved after large axial strain. In this case, the peak strength of samples with B_r values of less than 0.52 all obtained the maximum shear stress at 15% strain instead. Larger amount of axial strain (up to 25%-30%) is recommended to reach the full peak strength for Puerto Rico sand. In contrast, the peak strength of sample with $B_r = 0.55$ was achieved at the strain between 12% and 13%, which was regarded as evidence of a trend of transformation from ductile behavior to brittle behavior.

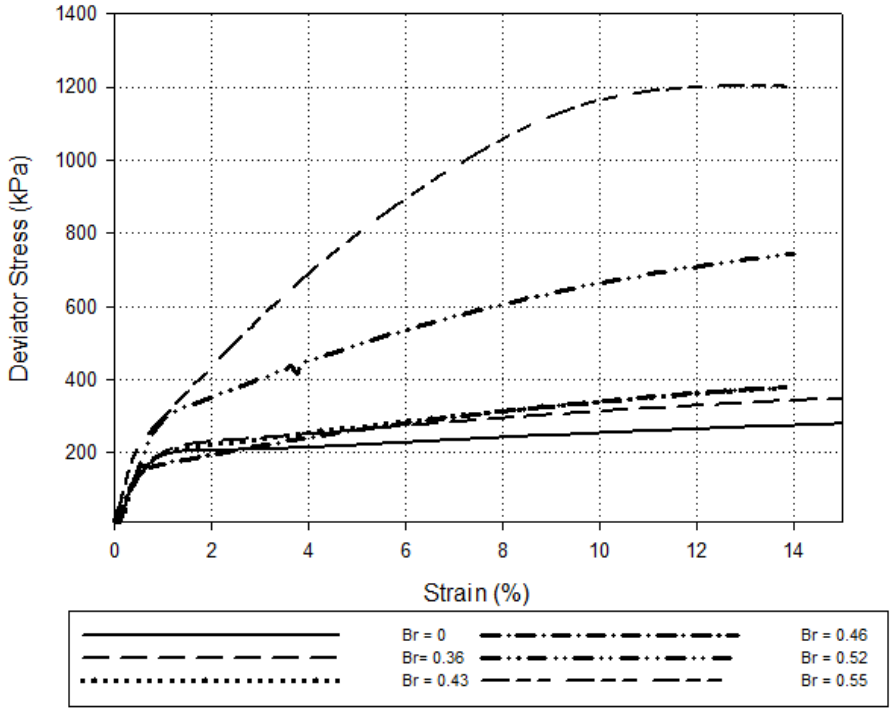

Figure 6.1. Stress-Strain Curves of the PR Sand with Increasing Particle Breakage

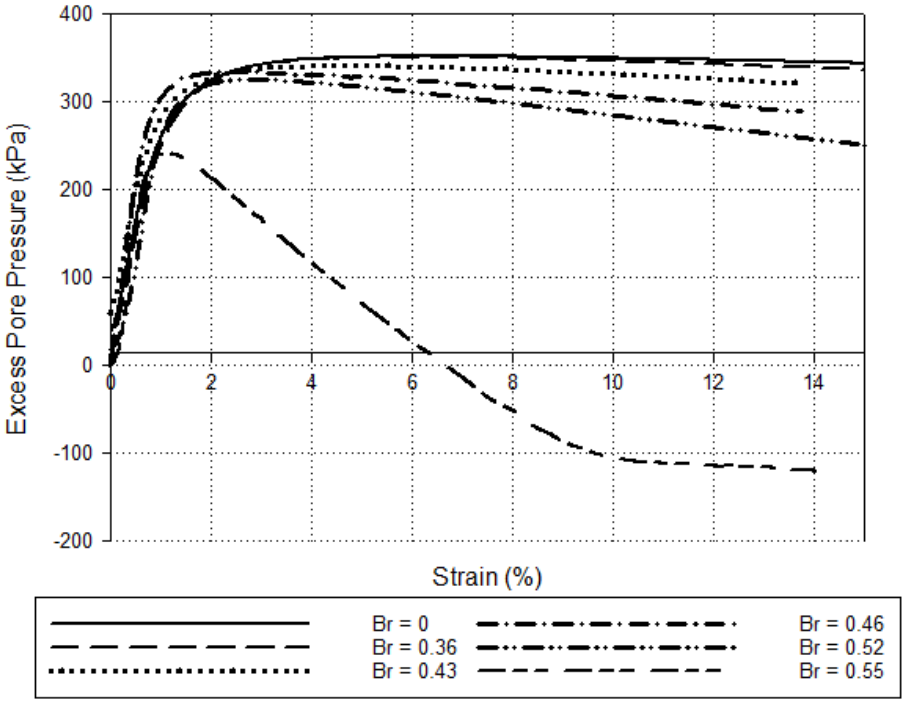

Figure 6.2. Excess Pore Pressure Change on Triaxial CU Tests for the PR Sand with Increasing Particle Breakage

In the case of undrained shear tests, the total volumetric strain is zero; therefore, the change of the pore pressure was utilized to evaluate the dilative and contractive behavior of soil. As demonstrated in Figure 6.2, the sample with $B_r = 0.55$ exhibited a dilative behavior in undrained tests. The pore pressure started to decrease after 1% strain and turned to negative value beyond 6% strain till the end of the test. The uncrushed Puerto Rico sand exhibited a strong contractive behavior, which maintained almost the constant pore pressure after peaking. As the particle breakage increased, the pore pressure curve slanted downward, showing the clear trend of pore pressure decrease and indicating an increasingly dilative tendency. The combined stress paths are presented in Figure 6.3. The contractive and dilative behavior with increasing B_r values are consistent with the pore pressure measurements. Sample with $B_r = 0.05$ changed from contraction to dilation at an early stage during shearing; whereas for samples with particle breakage less than 0.52, the phase transformation occurred at the later stage of shearing. It was also noted that the peak failure envelopes of crushed Puerto Rico sand were not uniform due to the different peak friction angles. High crushability made Puerto Rico sand easy to be crushed and to achieve high particle breakage content. This high breakage content led to grain rearrangement and different gradations, which changed the mobilization of peak friction angle.

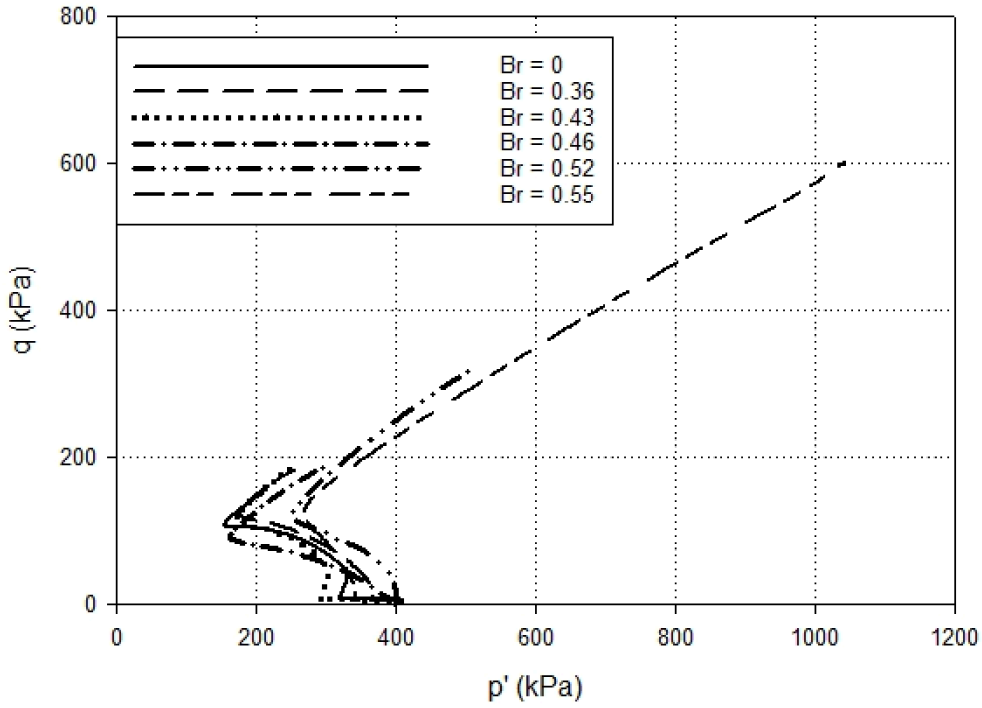

Figure 6.3. Stress Paths of the PR Sand with Increasing Particle Breakage in Undrained Tests

According to the discussion in the last paragraph, the static behavior of Puerto Rico sand was in consistent with the increasing particle breakage. Results from B_r = 0.43 and 0.46 did not follow the same trend as the other tests. The specimens were created using two methods to crush the particles, which resulted in different crushed particle size distributions. The degree of particle breakage was determined based on the crushed particle gradation and initial gradation. However, the crushed particle gradation caused by consolidation differed from the crushed gradation caused by shearing, as discussed in Chapter 5. The static behavior may be more consistent if specimens were created using only one method for crushing; however, in this research, the testing specimens were made from combined crushed particle gradations due to the limited available sand volume. For crushed Puerto Rico sand, the consolidation crushed samples (B_r = 0.36 and 0.43) obtained less middle fraction particles and more fine fraction particles than shearing crushed samples (B_r = 0.46, 0.52, and 0.55), resulting in a higher value of uniformity

coefficient of particle size distribution. The correlation between the uniformity coefficient (C_u) and shear strength is demonstrated in Figure 6.4. It can be inferred that there was an optimum C_u range related to high shear strength for Puerto Rico sand; the sand gradation having the C_u value within this optimum range led to the extremely high shear strength.

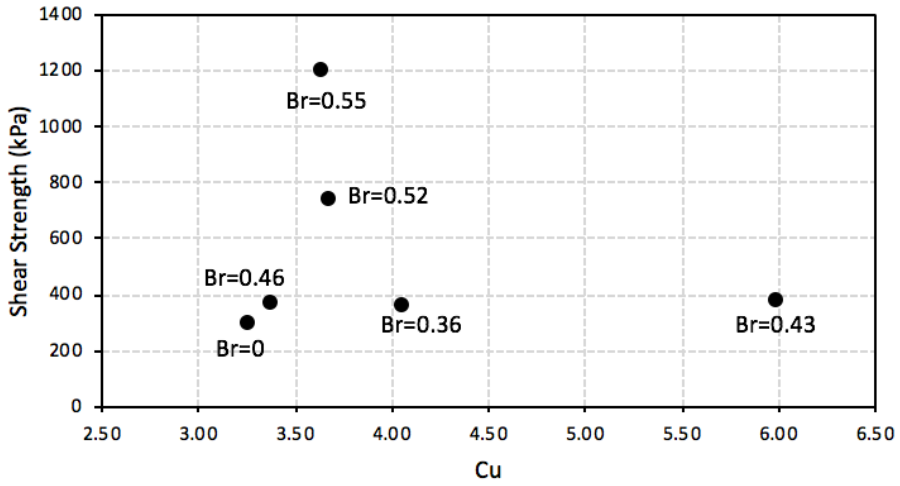

Figure 6.4. Correlation between Uniformity Coefficient (Cu) and Shear Strength for Puerto Rico Sand

Stress-Strain Response of Crushed Ledge Point Sand

A series of the LP sand specimens were prepared with increasing particle breakage contents obtained in Chapter 5 (i.e. B_r = 0.02, 0.05, 0.07, 0.08, and 0.14). The initial particle size distribution of the LP sand limited its crushability leading to less particle breakage content subjected to the same loading stress as compared to the PR sand. To investigate the monotonic stress-strain response of crushed LP sand, triaxial consolidated undrained (CU) tests were performed on the reconstituted specimens with increasing crushing contents. Sample preparation and testing procedures were the same as the steps done for the PR sand. Terminal axial strain level of 15% and strain rate of 1%/hour were used as well. Stress-strain response, pore pressure change, and stress paths were plotted in Figure 6.5, Figure 6.6, and Figure 6.7.

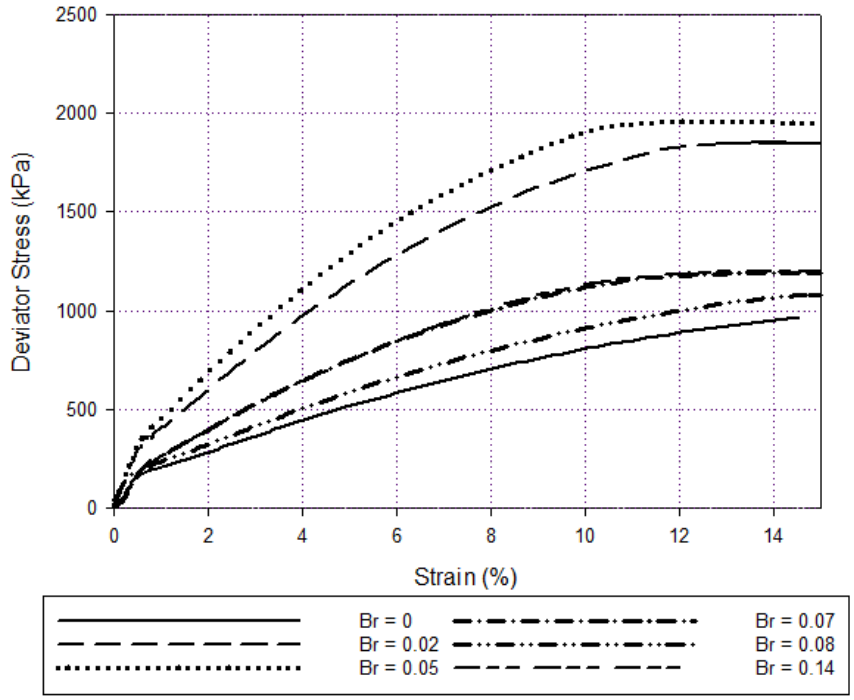

Figure 6.5. Stress-Strain Response of the LP Sand with Increasing Particle Breakage

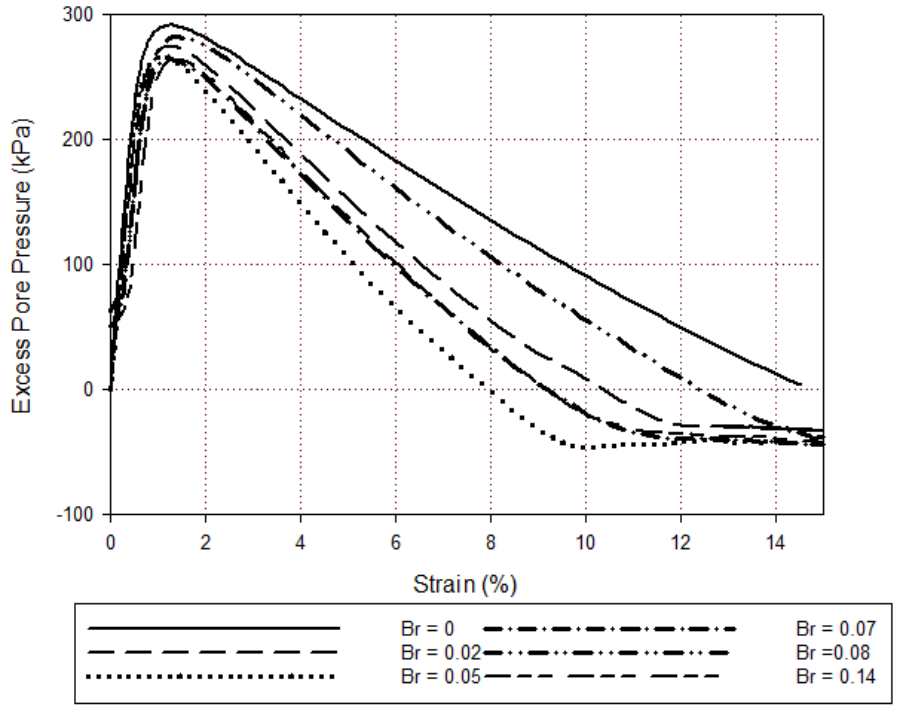

Figure 6.6. Excess Pore Pressure of the LP Sand with Increasing Particle Breakage

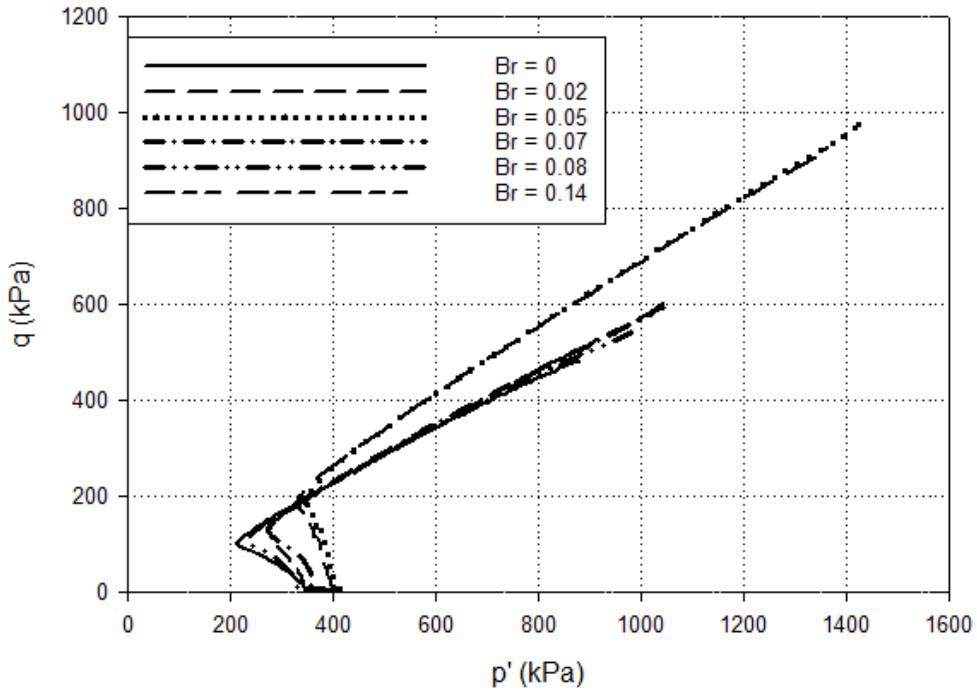

Figure 6.7. Stress Paths of the LP Sand with Increasing Particle Breakage

The uncrushed ($B_r = 0$) LP sand obtained the lowest shear strength within 15% axial strain. There was a significant shear strength increment when particle breakage content increased from 0 to 0.02. Shear strength then increased a small amount when B_r increased to 0.05. The stress-strain curves of $B_r = 0.07$ and 0.14 overlapped together, obtaining the same shear strength; the strength of $B_r = 0.08$ was lower than the strength of $B_r = 0.07$ and 0.14. Since the strength difference between $B_r = 0.08$ and $B_r = 0.07$ was small compared to the entire strength scale; therefore, the result from $B_r = 0.08$ could be regarded as the same strength range with the breakage content of 0.07 and 0.14. Except for the samples of $B_r = 0$ and 0.08, other samples exhibited more brittle behavior by achieving the maximum strength at 11% to 14% strain, followed by the slightly strain softening after the maximum strength.

As shown in Figure 6.7, the uncrushed and crushed LP sand exhibited dilative behavior after 1% axial strain. As discussed in Chapter 4, the uncrushed LP sand with fine-grade particles

provided less freedom for particles to move when subjected to shearing; therefore, the particles contracted only at the early stage and turned to a dilative behavior due to particle interlocking. The increasing particle breakage contents led to more fine particles in the sample matrix; as a result, the crushed sands contracted less and exhibited a stronger dilative behavior during shearing. The sample with particle breakage of 0.02 and 0.05 had the similar stress path overlapping together as shown in Figure 6.7 and showed the similar stress-strain response; likewise, the rest series with B_r values of 0, 0.07, 0.08 and 0.14 obtained the similar stress paths.

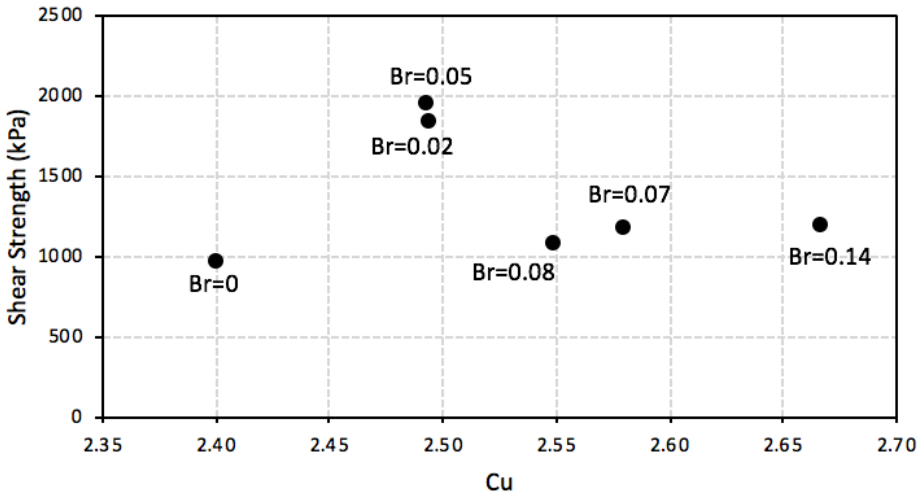

Figure 6.8. Correlation between Uniformity Coefficient (Cu) and Shear Strength for Ledge Point Sand

In the case of the LP sand, the shear strength had a huge jump when particle breakage increased, while the strength dropped down to a lower range as the crushing content increased, which was still higher than the strength of uncrushed sand. It could be assumed that this inconsistent correlation was due to the particle gradation of crushed LP sand. Figure 6.8 shows plots of the uniformity coefficient (C_u) for each crushed sand with its corresponding peak strength. Samples achieved the highest strength (B_r = 0.02 and 0.05) obtained the similar C_u value around 2.49; however, other samples below and beyond than this C_u value were all gained

a relative low strength. Therefore, the same conclusion can be made here: there is an optimum C_u range for crushed LP sand to achieve the extremely high strength; thus, particle size distribution of crushed calcareous sand should be considered as a co-factor when analyzing the effect on shear strength with increasing particle breakage.

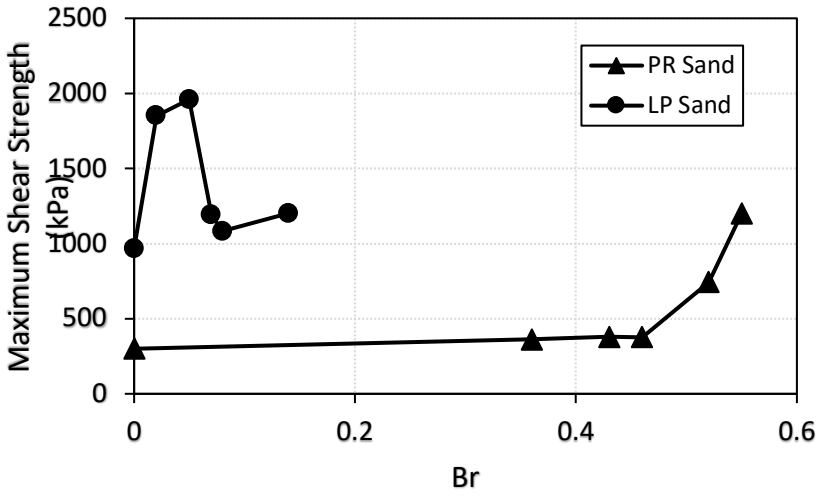

Figure 6.9. Shear Strength with Increasing Br Values for PR Sand and LP Sand

The results of the strength change based on the increasing particle breakage for both PR and LP sand were plotted in Figure 6.9. As the particle breakage increased, the undrained shear strength of the PR sand increased as well. Although the shear strength of the LP sand increased and then decreased as the crushing content increased, the overall trend still indicated that the increasing particle breakage improved the undrained shear strength. According to the results, the strength increase was due to the particle gradation in which the uniformity coefficient (C_u) fell in the optimum range for each type of calcareous sand.

Stiffness and Particle Breakage

Particle breakage affected the particle gradation and the stress-strain response for the PR sand and LP sand. The initial Young's modulus (E) and the initial stiffness for each crushed calcareous sample were determined in terms of Equation 4.1 and Equation 4.4 mentioned in

Chapter 4. The corresponding secant stiffness (G_{sec}) was calculated based on the secant Young's modulus from the stress-strain curve. Figure 6.10 and Figure 6.11 show plots of the initial Young's moduli and initial stiffness with increasing particle breakage for PR sand and LP sand, respectively. The strength change along with the particle breakage was also plotted in the same graph as a reference.

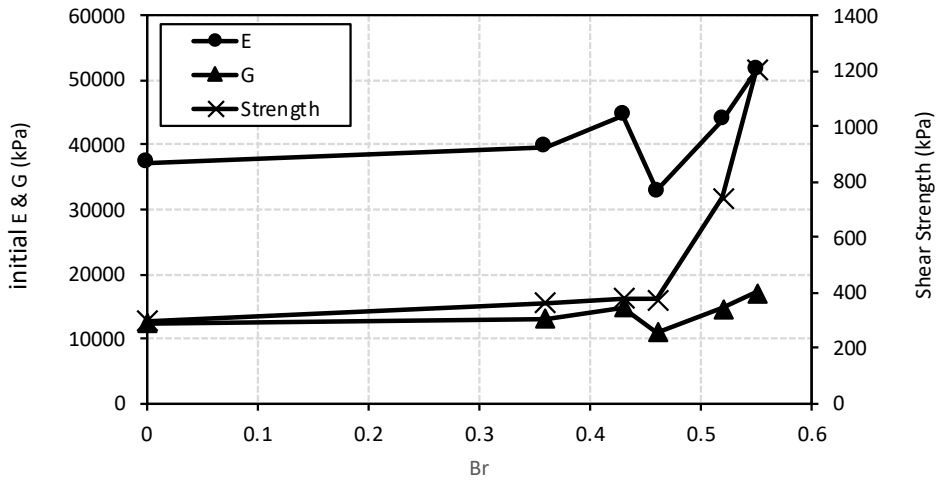

Figure 6.10. Initial Young's Moduli and Stiffness with Increasing Br for PR Sand

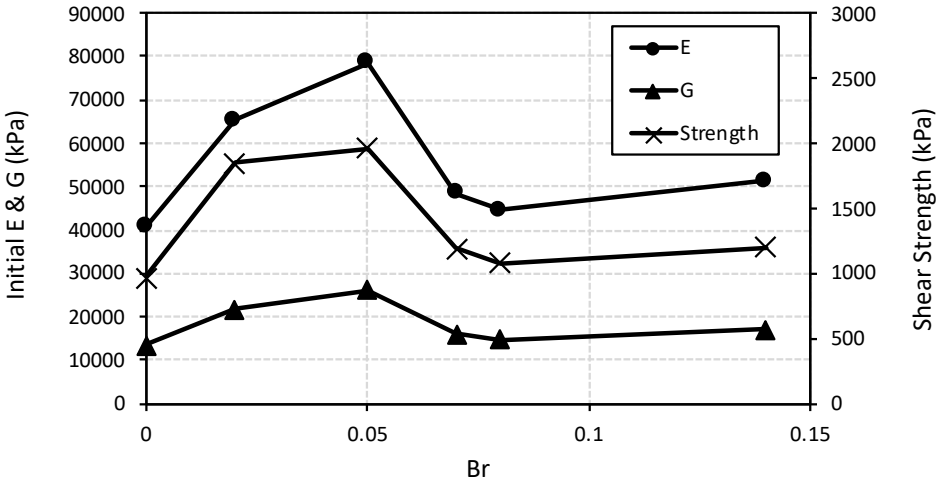

Figure 6.11. Initial Young's Moduli and Stiffness with Increasing Br for LP Sand

As shown in Figure 6.10 and Figure 6.11, initial Young's modulus, initial stiffness, and shear strength were affected by particle breakage. To show the correlation for these four factors, double vertical arises were used. The left vertical axis presents the magnitude scale of initial Young's modulus and stiffness; the right vertical axis presents the shear strength scale.

Although there was a decrease at $B_r = 0.46$ for the PR sand, the overall trends for initial Young's modulus and stiffness increased as the increasing of crushing content and was consistent with the trend of the shear strength. For the LP sand, the change of initial Young's modulus and stiffness, along with the increasing particle breakage, was more consistent with the trend of the shear strength. The particle breakage resulted in the increase of two initial parameters compared to the uncrushed sand.

Young's modulus is not a constant parameter for a given soil; thus, the stiffness, a function of Young's modulus, is also changed along with the axial strain. In Chapter 4, the stiffness was shown to degrade as the axial strain increased. To investigate the influence on the stiffness degradation by increasing crushing content for both calcareous sands, the changing ratio of secant stiffness to initial stiffness (G_{sec}/G_i) with various crushing contents for each sand were plotted in one graph (Figure 6.12 and Figure 6.13). The ratio of G_{sec}/G_i was utilized to compare the curves within a narrow range

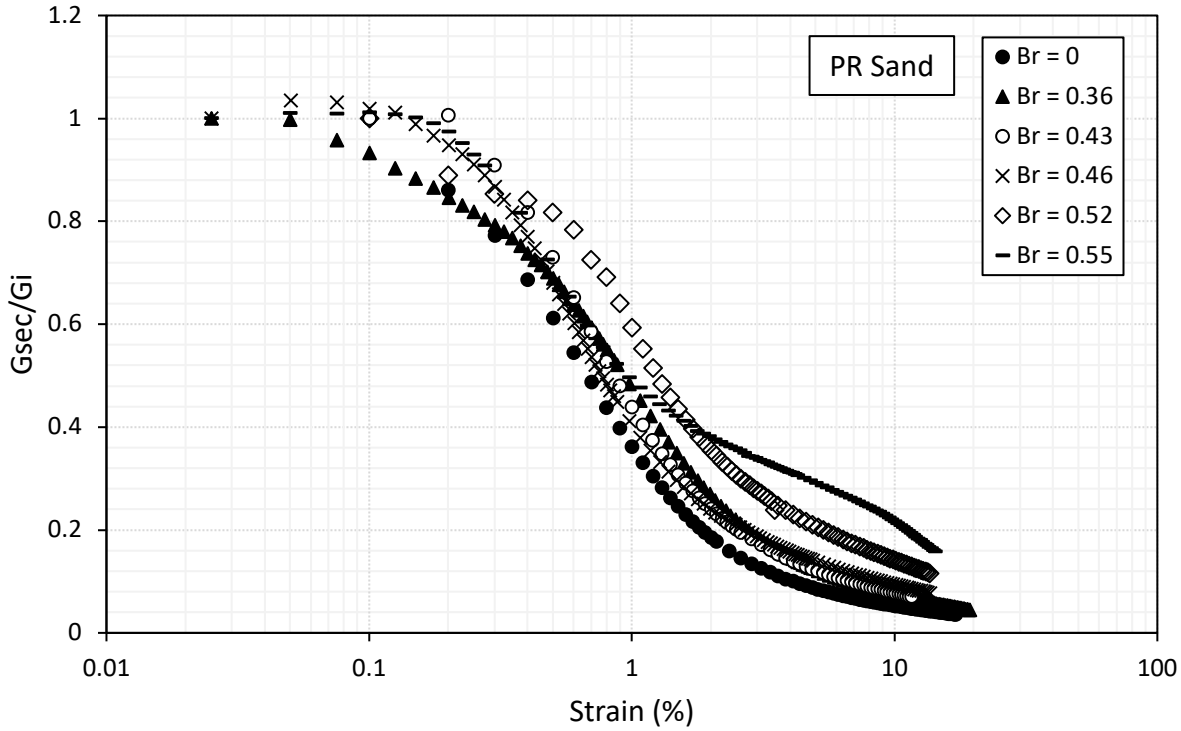

Figure 6.12 Stiffness Degradation for the PR Sand with Increasing Particle Breakage.

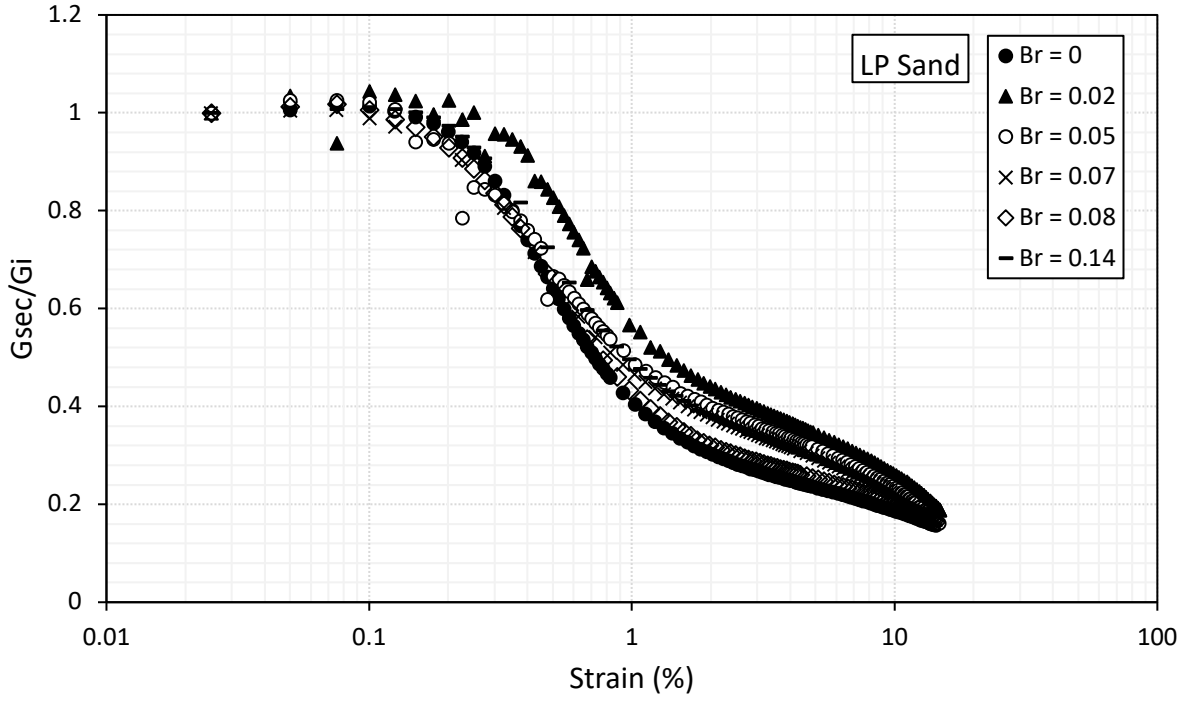

Figure 6.13 Stiffness Degradation for the LP Sand with Increasing Particle Breakage.

For the PR sand, the stiffness degradation curves decreased as particle breakage increased, indicating a degradation effect on the stiffness. There did not appear to be a "threshold" strain for uncrushed Puerto Rico sand; as the crushing content increased, the "threshold" shear was identified at the early stage of axial strain. Additionally, the PR sand with $B_r = 0.55$ had the highest shear strength which resulted in the lowest stiffness degradation. Compared to the PR sand, the stiffness degradation curves of LP sand occupied a narrower range, and the lowest stiffness degradation was observed from the crushed LP sand with $B_r = 0.02$. Therefore, the degree of stiffness degradation for the PR sand and LP sand was actually consistent with shear strength rather than increasing crushing content. Overall, particle breakage has the positive influence on calcareous sands which decreased the degree of stiffness degradation on crushed samples.

Contractive and Dilative Behavior with Increasing Particle Breakage

The modified Rowe's model (Ueng and Chen, 2000) discussed in previous chapters demonstrated the correlation of effective stress ratio, dilatancy, and particle breakage. The modified model is applicable to triaxial drained test due to the known volumetric change obtained during test; however, because the total volumetric change is zero in undrained case, the modified Rowe's model is not available to analyze the undrained data when considering the effect of particle breakage. Dehnavi et al. (2010) suggested a method to quantify the dilative and contractive reactions based on excess pore pressure for the undrained condition.

The response of calcareous sand for undrained shearing test can be measured by the generation of excess pore pressure and increasing of shear strength. The calcareous sands exhibited contractive behavior following an increase of pore pressure during shearing. This contractive behavior continued until the maximum pore pressure was achieved. Then, the sands behaved with a dilative response, while the pore pressure decreased at the phase transformation.

The second stage maintained until the strain corresponding to the maximum effective stress ratio; then the third stage started, and the effective stress ratio decreased.

The intensity of the contractive and dilative behavior was related to the variation of the pore pressure. Two parameters were used to define and quantify these two behaviors. Parameter named R_{uc} was used to indicate the intensity of contractive behavior during monotonic undrained shearing, as in the following equation:

$$R_{uc} = \frac{u_{max}}{\sigma_3} \quad (6.1)$$

in which, u_{max} is the maximum excess pore pressure, and σ_3 is the confining pressure. In this case, confining pressure of 400 kPa was used. The dilative behavior was quantified by the parameter, R_{ud}, expressed as:

$$R_{ud} = \frac{u_{max} - u_{residual}}{\sigma_3} \quad (6.2)$$

where, the $u_{residual}$ corresponded to the pore pressure at 15% strain. Then, the results of R_{uc} and R_{ud} for both calcareous sands with various crushing contents were determined and listed in Table 6.1. The correlation between dilatancy and particle breakage for PR sand and LP sand was shown in Figure 6.14 and Figure 6.15 respectively.

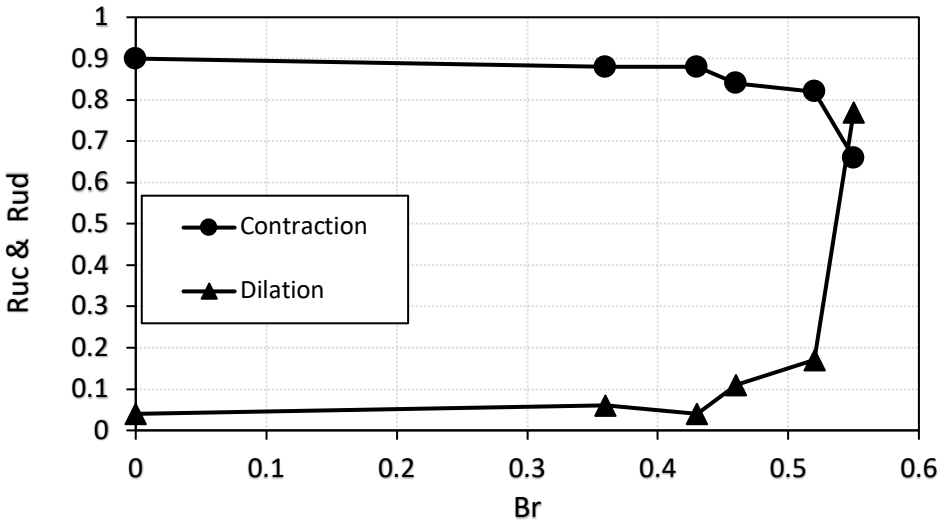

Figure 6.14. Contraction and Dilation of the PR Sand with Increasing Particle Breakage

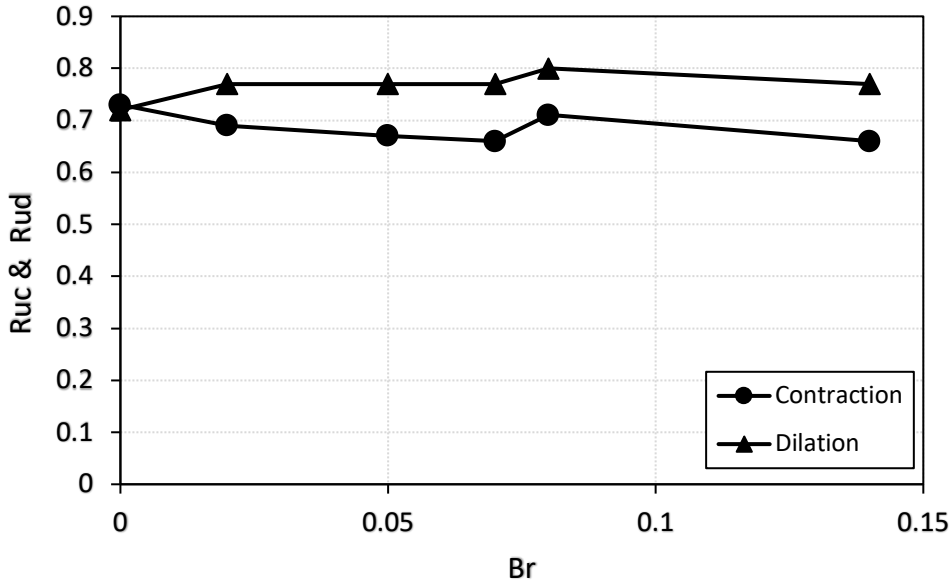

Figure 6.15. Contraction and Dilation of the LP Sand with Increasing Particle Breakage.

Table 6.1 Intensity of Contractive and Dilative Behavior for Puerto Rico Sand and Ledge Point Sand.

	Puerto Rico Sand					
B_r	0	0.36	0.43	0.46	0.52	0.55
R_{uc}	0.90	0.88	0.88	0.84	0.82	0.66
R_{ud}	0.04	0.06	0.04	0.11	0.17	0.77
	Ledge Point Sand					
B_r	0	0.02	0.05	0.07	0.08	0.14
R_{uc}	0.73	0.69	0.67	0.66	0.71	0.66
R_{ud}	0.72	0.77	0.77	0.77	0.80	0.77

The uncrushed PR sand exhibited contractive behavior during the undrained shear test with a high contraction intensity of 0.9 and a low dilative intensity of 0.04. With the increasing particle breakage, the contractive intensity reduced from 0.9 to 0.66. The decrease trendline is non-linear. A reduction in contractive intensity was observed at $B_r = 0.46$; after this, the contractive intensity decreased more as particle breakage increased. In contrast, the dilative behavior of Puerto Rico sand was increasing from 0.04 to 0.77 as the particle breakage increased. The dilative behavior was also observed for $B_r = 0.46$, followed by an increase from the dilative intensity of 0.17 to 0.77 corresponding to $B_r = 0.52$ and $B_r = 0.55$. It can be observed that the more particle breakage, the stronger influence on the behavior of contraction and dilation. Increasing particle breakage decreased the contractive behavior; on the contrary, the dilative behavior was increased with increasing particle breakage for the PR sand.

The contractive and dilative intensities of the LP sand were nearly the same. As the particle breakage increased, the dilative intensities increased and remained around the value of

0.77, and the contractive intensity decreased and remained around the value of 0.66. For the LP sand, particle breakage increased the sample dilation but did not have a strong influence on the contractive and dilative reactions as the crushing content increased. The possible reason could be that the crushing content of LP sand was not high enough since the highest crushing content obtained for LP sand was only 0.14. Likewise, the dilative and contractive intensities were almost the same for the PR sand with the B_r value lower than 0.52; however, a big change of the dilative and contractive intensities was observed for the PR sample with B_r value of 0.55. Therefore, the particle breakage has less influence on the dilative and contractive reactions unless the crushing content is high enough (i.e. $B_r > 0.5$). On the other hand, the coarse grained PR samples and the fine grained LP samples with similar dilative and contractive intensities had different shear strength; therefore, the particle gradation and the particle arrangement should be considered as the potential factors affecting the shear strength.

Summary

Reconstituted calcareous PR and LP sand samples were made following the crushed particle size distributions obtained from Chapter 5. Triaxial CU tests were performed on these reconstituted samples with a confining pressure of 400 kPa to investigate the static loading behavior with the increasing particle breakage.

The stress-strain response was consistent with the increased crushing content for the PR sand; however, the higher shear strength of the LP sand was obtained by the sample with B_r = 0.02, rather than the sample with the highest crushing content. Therefore, the crushing content of calcareous sands is not the primary factor which influencing the shear strength, and the effects of particle gradation and particle arrangement should be taken into account. For the LP sand, it was found that the strength is related to the uniformity coefficient (C_u), and an optimum range of uniformity coefficient value (around C_u = 2.5) contributed to the highest shear strength. This also

held true for the PR sand. Although the highest strength was achieved by the highest crushing content of the PR sand, the corresponding C_u value fell in its optimum range. The optimum range of the PR sand differed from that of the LP sand; thus, the optimum range of C_u was varied from sand to sand.

On the other hand, particle breakage was observed having a slight slow-down effect on stiffness degradation but did not show a sufficient influence on it. Stiffness is a function of the deviator stress increment along with the axial strain; thus, the degree of stiffness degradation was more consistent with the stress-strain response.

Since the total volumetric change is zero for the undrained shear test, an alternate method was introduced in this chapter to quantify the dilative and contractive reactions based on the excess pore pressure. The results indicated that the increasing crushing content decreased the contractive intensity and increased the dilative intensity for both PR sand and LP sand; however, the influence on the dilative and contractive intensities was not evident, unless a large crushing content was achieved, such as the B_r value higher up to 0.55 in the case of the PR sand. On the other hand, the dilative intensity was approximately kept constant for samples with low crushing contents, but the corresponding shear strength was different. Thus, the effect of particle gradation and particle arrangement should be taken into account.

CHAPTER 7. CONCLUSION

Calcareous sands are prevalent in many coastal regions of the world in low latitudes, and they trigger challenges on offshore constructions, such as oil and gas projects. This research has mainly focused on the stress-strain response of uncemented calcareous sands, from Puerto Rico and Australia under increasing severities of particle damage. It has been reported that the measured capacities in calcareous sand were approximately 20% lower than the predicted values. Therefore, it is important to know how the particle crushing content influences its loading response after the construction. The calcareous sands from Cabo Rojo, Puerto Rico (PR sand) and Ledge Point, Australia (LP sand) were selected as the tested materials for this research, and a series of experimental programs have been summarized in the following paragraphs.

A detailed literature review was presented in Chapter 2, including an overview of the concept of calcareous sand and the geological background knowledge of Puerto Rico and Western Australia. In addition, the basic engineering properties, compression behavior, monotonic shearing behavior, and the effective parameters related to particle crushing are summarized.

It is necessary to obtain the physical and chemical properties of the tested materials; therefore, a series of tests were performed to determine the particle size distributions, specific gravities, the maximum and minimum void ratios, and the carbon contents. The testing results and the testing methods were summarized in Chapter 3. Ottawa sand was selected as a control group to show the difference between the calcareous sand and the silica sand.

Chapter 4 summarized the experimental results of triaxial consolidated undrained (CU) tests on uncemented calcareous sands from Puerto Rico and Australia, which aims to provide knowledge about the loading response of these two calcareous sands, such as the stress-strain

behavior, excess pore water change with increased strain, and stiffness degradation. The CU tests were performed on the two calcareous sands with the confining pressure of 200 kPa and 400 kPa, respectively. Additionally, an additional group of CU tests, conducted on the Ottawa sand with the confining pressure of 400 kPa, was taken as the control group to show how the loading response of calcareous sands differed from the silica sands.

In Chapter 5, the particle breakage of calcareous sands was discussed. Three testing methods were used: 1) One dimensional (1-D) consolidation tests on dry sands, 2) triaxial consolidated drained (CD) tests on dry sands, and 3) TruePath CD tests on saturated sands. For the 1-D consolidation tests, compressive pressures of 2,400 kPa and 4,800 kPa were selected. For the triaxial CD dry sand tests, confining pressures of 100 kPa, 300 kPa, and 400 kPa were used to preform specimens. Hardin's method (1985) was used to quantify the relative particle breakage of the tested calcareous sands. The results were collected to investigate the effect of loading mechanisms and water presence on particle breakage. Based on the crushing results, the crushing contents generated by the triaxial CD dry sand tests and the 1-D consolidation tests were selected as the reference data for the investigation of loading behavior of calcareous sand with increasing particle crushing in Chapter 6. At the end of Chapter 5, the modified Rowe's model based on the results from TruePath CD tests was introduced to illustrate the correlations between the effective stress ratio, the internal friction angle, and the particle breakage.

The static loading behavior of PR sand and LP sand with increasing particle crushing contents was investigated in Chapter 6. There were six crushing contents and the corresponding crushed particle size distributions for each sand which were obtained from the triaxial CD dry sand tests and the 1-D consolidation tests mentioned in Chapter 5. The specimens were prepared based on the crushed particle size distributions, and the triaxial CU tests were carried out on

these specimens at 400 kPa confining pressure, respectively. The correlations of loading response, stiffness degradation, and dilative behavior with increased particle breakage were discussed.

This research provided an insight into the difference between the calcareous sands and silica sands. Due to the high angularity, the high intraparticle porosity, and the high carbon content, calcareous sands obtained a higher specific gravity and maximum and minimum void ratios than silica sands. When subjected to the static load at the same confining pressure, the calcareous sands showed a lower shear strength and a ductile stress-strain response at the low strain level because the grain crushing hindered the development of potential maximum dilation.

Although calcareous sands differed from the silica sands, not all calcareous sands are the same. Both calcareous sands in this research were classified as the SP sand, but the LP sand had a finer particle size distribution, lower specific gravity, and lower maximum and minimum void ratios than the PR sand. The LP sand is the aeolian calcareous sand, and the PR sand consists of the debris of marine organisms; therefore, the PR sand exhibited a lower shear strength due to its high intraparticle structure leading to crushing when subjected to load. This information can be counted as the database for one of the sources of the calcareous sands all over the world and will be helpful for the other researchers and constructions in the future.

There were three methods mentioned in this research which were used to create particle breakage: TruePath CD saturated sand test, triaxial CD dry sand test, and 1-D consolidation dry sand test. Based on the results, shear loading generated more crushing content than compression loading with lower stress, and the shearing tests on dry sand samples crushed more particles than that on saturated sand samples. The crushing potential of calcareous sands depends both on the

initial particle size distribution and the intraparticle structure. The medium-to-coarse PR sand with high intraparticle voids had a higher crushing potential than the LP sand.

Modified Rowe's method indicated the correlation between the effective stress ratio, sample dilatancy, and particle breakage. Confining pressure influenced the intensities of dilation and particle breakage. As the confining pressure increased, the effect of dilation on shear strength decreased, while the particle breakage turned out to exhibit a significant influence on shear strength. For calcareous sand with coarser particles and higher intraparticle porosity, the particle breakage was the control factor of the shear strength when subjected to shear loading. Besides, for calcareous sand with finer and less intraparticle porosity, the effect dilatancy became the control factor at lower stress; as the confining pressure increased, the effect of particle breakage turned out to be significant on shear strength.

The triaxial CU test was found to be a good tool to simulate the scenario of the post-installed pile and reflect the stress-strain response surrounding that pile. Compared with the uncrushed calcareous sand samples, the crushed samples exhibited a higher shear strength. For the PR sand, the shear strength increased as the particle crushing content increased; however, the moderate particle crushing content of the LP sand led to a higher shear strength than that of the high crushing content. It can be concluded that the correlation between calcareous sand particle breakage and its shear strength not only depends on the particle crushing content but also is related to the sand's initial particle size distribution. For the medium to coarse calcareous sands, like PR sand, particle breakage improves the shear strength. Although the crushed samples exhibited a higher shear strength than the uncrushed samples, for fine to medium calcareous sand, there is an optimum particle crushing content resulting in the highest shear strength. It also can be inferred that the optimum particle crushing content of the PR sand will be achieved if

more particle crushing occurred. The optimum particle crushing content is not the same for all calcareous sands; on the contrary, each calcareous sand should have its own optimum crushing content. In addition, particle breakage had a slight slow-down effect on stiffness degradation, but the influence was not consistent as the crushing content increased. The stiffness degradation was mainly controlled by the deviator stress increment along with the axial strain.

Since the total volumetric change is zero for the undrained shear test, an alternate method was introduced in this chapter to quantify the dilative and contractive reactions based on the excess pore pressure. The results indicated that the increasing crushing content decreased the contractive intensity and increased the dilative intensity for both PR sand and LP sand; however, the influence on the dilative and contractive intensities was not evident, unless a large crushing content was achieved, such as the B_r value higher up to 0.55 in the case of the PR sand. On the other hand, the dilative intensity was approximately kept constant for samples with low crushing contents, but the corresponding shear strength was different. Thus, the effect of particle gradation and particle arrangement should be taken into account.

This research provides a basic idea about the static loading behavior of calcareous sands with increasing particle crushing content. However, the results of Puerto Rico sand differed from that of Ledge Point sand. The increasing particle breakage led to higher undrained shear strength for PR sand, while the particle breakage did not show a consistent influence on LP sand. Therefore, the effect of the increasing particle crushing content is different from site to site. The results obtained from this study can serve as a data base for future research and offshore projects, such as gas and oil platforms, offshore renewable industry, and pipeline design.

Recommendations for Future Work

Due to the limitation of the apparatus, research on this study, focusing on the static stress-strain response of calcareous sand with increasing particle crushing contents, was mainly

performed in the low stress and strain range. Higher stress levels and larger axial strain levels are expected to be involved in the future so that a detailed investigation can be performed on the correlation of stress, dilatancy, and particle breakage. Additionally, the modified Rowe's model mentioned in this research is also recommended to involve much higher stress levels and crushing contents in the future, so that there will be a more complete and thorough insight of the correlation between the particle breakage and dilation during shearing.

This research only focused on the static loading response after the construction. For a better understanding of the loading behavior of calcareous sands with increasing crushing contents, the cyclic tests are expected to be designed and performed in the future to simulate long term and more complex conditions, such as storm and earthquake.

REFERENCES

Arango, J. C. (2006). Stress–strain behavior and dynamic properties of Cabo Rojo calcareous sands. MSc thesis, University of Puerto Rico, San Juan, Puerto Rico.

ASTM C136 / C136M-14, Standard Test Method for Sieve Analysis of Fine and Coarse Aggregates, ASTM International, West Conshohocken, PA, 2014, www.astm.org.

ASTM D2488-17e1, (2017). Standard Practice for Description and Identification of Soils (Visual-Manual Procedures), ASTM International, West Conshohocken, PA, www.astm.org.

ASTM D4253-00, Standard Test Methods for Maximum Index Density and Unit Weight of Soils Using a Vibratory Table, ASTM International, West Conshohocken, PA, 2000, www.astm.org.

ASTM D4254-00, Standard Test Methods for Minimum Index Density and Unit Weight of Soils and Calculation of Relative Density, ASTM International, West Conshohocken, PA, 2000, www.astm.org.

ASTM D4767-11, Standard Test Method for Consolidated Undrained Triaxial Compression Test for Cohesive Soils, ASTM International, West Conshohocken, PA, 2011, www.astm.org.

ASTM D7181-11, Method for Consolidated Drained Triaxial Compression Test for Soils, ASTM International, West Conshohocken, PA, 2011, www.astm.org.

ASTM D854-14, Standard Test Methods for Specific Gravity of Soil Solids by Water Pycnometer, ASTM International, West Conshohocken, PA, 2014, www.astm.org.

Atkinson, J.H., 1993. The Introduction to the Mechanics of Soils & Foundations: Through Critical State Soil Mechanics. McGraw Hill.

Baldi, G., Nova, R., 1984. Membrane penetration effects in triaxial testing. Journal of Geotechnical Engineering 110 (3), 403–420.

Baharom, B. & Stallebrass, S. E. (1998). A constitutive model combining the microscopic and macroscopic behaviour of sands in shear and volumetric deformation. Proc. 4th Eur. Conf. on Numerical Methods in Geotech. Engng, Udine, 1998. Springer- Verlag Wien, New York. 1998, 263–273.

Bastidas, A.M., (2016). Ottawa F-65 Sand Characterization. Ph.D Dissertation, University of California, Davis.

Beemer, R., Sadekov, A., Lebrec, U., Shaw, J., Bandini, A., & Cassidy, M. (2019). Impact of biology on particle crushing in offshore calcareous sediments. In C. L. Meehan, S. Kumar, M. A. Pando, & J. T. Coe (Eds.), Geo-Congress 2019: Geotechnical materials, modeling, and testing (pp. 640-650). Virginia: American Society of Civil Engineers.

Beemer, R. D., Bandini-Maeder, A. N., Shaw, J., Lebrec, U., and Cassidy, M. J. (2018). The Granular Structure of two marine carbonate sediments. OMAE2018, ASME, Madrid.

Been K., Jefferies M.G., Hachey J., (1991). The critical state of sands. Géotechnique. 41:365-81.

Bolton M. D., (1986). The strength and dilatancy of sands. Geotechnique. 36(1):65–78.

Gianfranco, G., Matteo, M., Livio, S., and Penerbit, A. B., (2013). CFD Analysis and Risk Management Approach for the Long-Term Prediction of Marble Erosion by Particles Impingement. CFD Letters. 5.

Chandler, H. W. (1985). A plasticity theory without Drucker's postulate, suitable for granular materials. J. Mech. Phys. Solids 33, 215–226.

Clarke, P. U., Dyke, A. S., Shakun, J. D., Carlson, A. E., Clark, J., Wohlfarth, B., Mitrovica, J. X., Hostetler, S. W., McCabe, A. M., (2009). The Last Glacial Maximum. Science Vol 325, pp. 710-714.

Chaney, R.C., Slonim, S.M., and Slonim, S.S. (1982). Determination of Calcium Carbonate Content in Soils. Geotechnical Properties, Behavior and Performance of Calcareous Soils, ASTM Special Technical Publication 777, 3-15.

Coop, M.R., Sorensen, K.K., Bodas Freitas, T., Georgoutsos G (2004) Particle breakage during shearing of a carbonate sand. Géotechnique 54(3):157–16.

Coop, M.R., Airey, D.W. (2003). Carbonate sands. Proceedings of the International Workshop on Characterisation and Engineering Properties of Natural Soils, Tan, T.S., Phoon, K.K., Hight, D.W. & Leroueil, S. (eds), **2**: 1049-1086.

Coop, M.R., Lee, I.K. (1993). The behaviour of granular soils and elevated stresses. Predictive Soil Mechanics, Proceeding of C.P. Wroth Memorial Symposium. Thomas Telford, London: 186-198.

Coop, M. R. (1990). The mechanics of uncemented carbonate sands. Geotechinique, 40(4), pp. 607-626.

Dehnavi, Y., Shahnazari, H., Salehzadeh, H., and Rezvani, R. (2010). Compressibility and undrained behavior of Hormuz calcareous sand. Electronic J. Geotech. Eng., Vol. 15, Bund. O., pp. 1684–1702.

Estrada, B. (2013). Insights into the seismic hazard of Western Australia. Australian Geomechanics Journal, 48(2), 1-13.

Fookes, P.G. (1988). The Response of Calcareous Soil in Static and Cyclic Triaxial Tests. Proceedings of the International Conference on Engineering for Calcareous Sediments, Perth Jewell, R.J. & Andrews, D.C. (eds), Balkema, Rotterdam, 1:61-68.

Fitzsimons, I.C.W., (2003). Proterozoic provinces of Australia, and their correlation with Antarctica. In Yoshida M., Windley B.F. & Dasgupta S. (ed.). Proterozoic East Gondwana: supercontinent assembly and breakup. Geological Society Special Publication. 206. Geological Society. pp. 93–130. ISBN 978-1-86239-125-3.

Frydman, S., Talesnick, M., Nawatha, H., and Schwartz, K. (2007). Stress-dilation of undisturbed sand samples in drained and undrained triaxial shear,"Soils and Foundations, 47(1), 27-32.

Geology of Western Australia. (2017, June 19). Department of Mines, Industry Regulationand Safety. Government of Western Australia. Retrieved March 9, 2020, from https://www.dmp.wa.gov.au/Geological-Survey/Geology-of-Western-Australia-1389.aspx

Gianfranco, G., Matteo, M., Livio, S., and Penerbit, A. B., (2013). CFD Analysis and Risk Management Approach for the Long-Term Prediction of Marble Erosion by Particles Impingement. CFD Letters. 5.

Golightly C.R. and Hyde A.F.L., (1988). Some fundamental properties of carbonate sands. Engineering for Carbonate Sediments, R. J. Jewell, and D. C. Andrews, eds., Balkema, Perth, pp. 69-78.

Gozzard, J. R. (2007). Geology and landforms of the Perth region. East Perth: Geological Survey of Western Australia, Dept. of Industry and Resources.

Hardin, B.O., (1985). Crushing of soil particles. Journal of Geotechnical Engineering. 111 (10), 1177–1192.

Hasanlourad, M., Salehzadeh, H., Shahnazari, H., (2008). Dilation and particle breakage effects on the shear strength of calcareous sands based on energy aspects. Int. J.Civil. Eng 6 (2), 108–119.

Hashimoto, T., Bailey, A. and Chirinos, A. 2018. Onshore Basin Inventory Volume 2: The Canning, Perth and Officer basins. Record 2018/18. Geoscience Australia, Canberra.

Hurlbut, C. S. (1971). Dana's Manual of Mineralogy. 18th Ed. John Wiley & Sons, Inc., New York.

Hyodo, M., Aramaki, N., Nakatay, Y., Inoue, S., Hyde, A.F.L., (1999). Particle Crushing and Undrained Shear Behaviour of Sand: Cupertino, CA, ETATS-UNIS, Int. Soc. Offshore. Polar. Eng.

Hyodo, M., Aramaki, N., Itoh, M. & Hyde, A. F. L. (1996). Cyclic strength and deformation of crushable carbonate sand. Soil Dyn. Earthq. Engng 15, No. 5, 331-336.

James, N. P., Bone, Y., Kyser, T. K., Dix, G. R., and Collins, L. B. (2004). "The importance of changing oceanography in controlling late Quaternary carbonate sedimentation on a high-energy, tropical, oceanic ramp: North-western Australia." Sedimentology, Wiley, 51(6), 1179–1205.

Kaggwa, W.S. (1988). Cyclic behaviour of carbonate sediments. PhD Thesis, University of Sydney, Australia.

Kaye C. A., (1959). Coastal geology of Puerto Rico: (A) Geology of the San Juan Metropolitan Area. US Government Printing Office, Washington, DC, Geological Survey Professional Paper 317.

Kaye, C. A., (1959). Shoreline features and Quaternary shoreline changes, Puerto Rico. Geological Survey Professional Paper, 317-B.

Keller, G. H. (1967). Shear strength and other physical properties of sediments from some ocean basins. Proceedings ASCE Conference on Civil Engineering in the Oceans, San Francisco, Calif., 391-417.

Lade, P. V., Yamamuro, J. A., and Bopp, P. A. (1996). Significance of particle crushing in granular materials. J. Geotech. Engrg., ASCE, 122(4),309-316.

Lade, P. V., (2016). Triaxial testing of soils. Chichester, West Sussex, United Kingdom: Wiley, Blackwell.

Lillie, R.J., (2005). Parks and Plates: the Geology of Our National Parks, Monuments, and Seashores. W.W. Norton.

Mann, P., Calais, E., Ruegg, J.C., DeMets, C., Jansma, P.E., and Mattioli, G.S., (2002). Oblique collision in the northeastern Caribbean from GPS measurements and geological observations. Tectonics, Vol. 21, No.6, p. 1057.

Miura, N. and T. Yamanouchi (1971). Drained shear characterisics of Toyoura sand under high confining stress. Japanese Society of Civil Engineers: 69-79.

Moore, C.H. (1989). Carbonate Diagenesis and Porosity. Elsevier Science Publications.

Morales-Velez, A.C., (2014). Evaluation of Field Based Liquefaction Approaches for Calcareous Sands Using Shear Wave Velocity. Open Access Dissertations. Paper 274. University of Rhode Island.

Morelock, J., and Ramirez, W. (2004). "Marine Sediments". Marine Geology, <http://geology.uprm.edu/Morelock/GEOLOCN_/sedimt.htm> (November 8, 2019).

Morelock J., Taggart B. (1988) USA--Puerto Rico. In: Walker H.J. (eds) Artificial Structures and Shorelines. The GeoJournal Library, vol 10. Springer, Dordrecht.

Morelock, J., (1978). Shoreline of Puerto Rico. Coastal Zone Management Program, San Juan, Department of Natural Resources, Puerto Rico, 45 p.

Morse, J. W., and Mackenzie, F. T. (1990). Geochemistry of Sedimentary Carbonates. Elsevier Science Publishers B. V., Amsterdam.

Pestana, J. M. (1994). A unified constitutive model for clays and sands. ScD thesis, Massachusetts Institute of Technology, USA.

Phan, V.T.A., Hsiao D.H, Nguyen P.T.L., (2016). Critical state line and state parameter of sand-fines mixtures. Procedia Engineering, 2016, 142: 298-305.

Pinkert, S. (2016). Rowe's stress-dilatancy theory for hydrate-bearing sand. International Journal of Geomechanics, 17(1), 06016008.

Raymond, O.L., Liu, S., Gallagher, R., Zhang, W. & Highet, L.M., (2012). Surface Geology of Australia 1:1 million scale dataset 2012 edition. Geoscience Australia, Canberra.

Rowe, P. W. (1962). The stress-dilatancy relation for static equilibrium of an assembly of particles in contact, Paper presented at Proceedings of the royal society of London a: Mathematical, physical and engineering sciences, The Royal Society.

Safinus, S, Hossain MS and Randolph M.F., (2013). Comparison of Stress-Strain Behaviour of Carbonate and Silicate Sediments. Proceedings of the 18th International Conference on Soil Mechanics and Geotechnical Engineering, Paris

Scanlon, K. M., Rodríguez, R. W., Trias, J. L., and Delorey, C. M., (1998). Offshore sediments and sand and gravel resources on the insular shelf of Puerto Rico. U.S. Geological Survey, Open-File Report 98-38, 202-217.

Shahnazari, H. A., Tutunchian, M., Rezvani, R., and Valizadeh, F. (2012). Evolutionary-based approaches for determining the deviatoric stress of calcareous sands. Computers & Geosciences, Vol. 50, pp. 84–94.

Shahnazari H, Rezvani R (2013) Effective parameters for the particle breakage of calcareous sands: an experimental study. Eng Geol 159:98–105

Sharma, S. S. (2004). Characterization of cyclic behavior of calcite cemented calcareous soils. Ph.D. thesis, Univ. Western Australia, Perth, Australia.

Silica, U. (2016). Product data: F-65 whole grain silica plant: Ottawa, Illinois, US Silica, https://www.ussilica.com

Spagnoli, G., & Doherty, P. (2016). Comparison between the mixed-in-place technology and driven piles as offshore foundations. Society of Petroleum Engineers. doi:10.2118/182974-MS.

Terzaghi, K., Peck, R. B., and Mesri, G. (1993). “Soil Mechanics in Engineering Practice”. 3rd Ed. John Wiley & Sons, Inc, New York.

Tugores García, A., 2008. Loading rate effects on Dog's Bay sand. Thesis. Univ Cataania: 71–72.

Ueng, T.S., Chen, T.J., (2000). Energy aspects of particle breakage in drained shear of sands. Geotechnique 50 (1), 65–72.

Wang, X. Z., Jiao, Y. Y., Wang, R., Hu, M. J., Meng, Q. S., and Tan, F. Y. (2011). Engineering characteristics of the calcareous sand in Nansha Islands, South China Sea.”*Eng. Geol.*, Vol. 120, pp. 40–47.

Zhang, J.M., Zhang, L., Jiang, G.S. et al., (2008). Research on Particle Crushing of Calcareous Sands under Triaxial Shear. [J]. Chinese Journal of Rock Mechanics and Engineering, 29(10): 2789-2793.

Zhang, J.M., Jiang, G.S., Wang, R., (2009). Research on Influences of Particle Breakage and Dilatancy on Shear Strength of Calcareous Sands. [J]. Chinese Journal of Rock Mechanics and Engineering, 30(7): 2043-2048.

Zhang, J.M., Wang, R., Shi, X.F., et al., (2005). Compression and crushing behavior of calcareous sand under confined compression [J]. Chinese Journal of Rock Mechanics and Engineering, 24(8): 3 327 - 3 331.